Ion-enhanced growth in planar and structured Mo/Si multilayers

Toine van den Boogaard

Ion-enhanced growth in planar and structured Mo/Si multilayers

Toine van den Boogaard

Ph.D. committee

Chairman:

Prof. dr. G. van der Steenhoven	Univ. Twente, TNW

Secretary:

Prof. dr. G. van der Steenhoven	Univ. Twente, TNW

Promoter:

Prof. dr. F. Bijkerk	Univ. Twente, TNW FOM Rijnhuizen

Members:

Prof. dr. K.J. Boller	Univ. Twente, TNW
Prof. dr. ir. H.J.W. Zandvliet	Univ. Twente, TNW
Dr. P.W.H. Pinkse	Univ. Twente, TNW
Prof. dr. ir. M.C.M. van de Sanden	TU Eindhoven

Cover:

Optical microscopy image of the surface of a multilayer mirror with rectangular micromesh patterned areas. The sample has been fabricated by the method as described in chapter 7.

ISBN: 978-94-6191-120-9

Ion-enhanced growth in planar and structured Mo/Si multilayers

PROEFSCHRIFT

ter verkrijging van de graad van doctor
aan de Universiteit Twente, op gezag van
de rector magnificus, prof. dr. H. Brinksma,
volgens besluit van het College voor Promoties
in het openbaar te verdedigen op
dinsdag 13 december 2011 om 12:45 uur

door

Antonius Johannes Ronald van den Boogaard

geboren op 17 januari 1982

te Zeist

Dit proefschrift is goedgekeurd door de promotor

Prof. dr. F. Bijkerk

This work is part of the FOM Industrial Partnership Programme I10 (‘XMO’) which is carried out under contract with Carl Zeiss SMT AG, Oberkochen and the ‘Stichting voor Fundamenteel Onderzoek der Materie (FOM)’, the latter being financially supported by the ‘Nederlandse Organisatie voor Wetenschappelijk Onderzoek (NWO)’.

Contents

Chapter 1

Introduction

I. Motivation

The human eye is sensitive to a restricted part of the electromagnetic spectrum surrounding us in daily life; this part we know as “visible light”. Besides observing colors, we can distinguish a large range in light intensities and experience geometry through our sense of vision. Yet, a very important feature of light which we cannot directly observe is its wave-nature, while typical phase oscillation frequencies are much too fast to follow. It is this wave-nature that yields fascinating interference phenomena in light when interacting with matter. Such physical interactions of waves with obstacles are generally addressed by the term diffraction.

A fundamental, but somewhat inconvenient property of diffraction is that it limits the ultimate resolution in an imaging system. As is described by the Rayleigh criterion [1], the minimal resolvable spot-size Δf for an ideal imaging system is proportional to the wavelength λ of the electromagnetic radiation:

$$\Delta f \propto \lambda / NA. \qquad (1.1)$$

Here $NA = n\sin(\varphi)$ is defined as the numerical aperture, with φ the acceptance angle of the lens and n the index of refraction of the medium of operation. The use of a high refractive index emersion liquid between lens and sample can thus increase the resolution, but employing visible light (wavelength 390 to 750 nm) conventional optical microscopes cannot standardly resolve details smaller than 200 nm. Recently, the use of special scattering lenses and a manipulated incoming wave front have been demonstrated to yield a minimal focal spot-size just below 100 nm, which is below the diffraction limit at the wavelength used as given by equation (1.1), see reference [2].

A large increase in resolution can in principle be achieved by reducing the wavelength, i.e. to values much smaller than the visible light range.

However, transmission optics (i.e. lenses) are not applicable at wavelengths below approximately 100 nm, since the absorption coefficient of all know materials becomes too high and the refractive indices approach unity; the radiation simply would be fully extinguished by a lens of a thickness as appropriate for focusing. It is for this reason that optical multilayer structures have been under continuous attention since several decades [3-5]. Multilayer optics are operated in reflection, as a mirror, hereby circumventing the unacceptable high absorption that would occur in transmission optics at short wavelengths. The highly periodic nanoscale layered structure serves to exploit diffraction, enabling spectacularly increased reflectance values as compared to single-interface mirrors.

The development of a class of multilayer optics with optimized reflectance and operational lifetime is of vital importance for the semiconductor industry, whereas optical lithography is the governing technique in integrated circuit production. Optical lithography can be regarded to be the reversed equivalent of microscopy; it is not concerned with the imaging of magnified details of a specimen, but with the demagnified projection of small details on a photo-sensitive lacquer (resist). This technique enables the production of individual components on integrated circuits, e.g. for computer chips, and can be explicatory described as “writing with light”. The ongoing endeavor of producing smaller structures and hence more powerful computer chips implies that each newly developed lithography tool, a so-called wafer-stepper, operates at smaller wavelengths and beyond the diffraction limits of its predecessor. Next generation wafer-steppers currently considered run at the extreme ultraviolet (EUV) wavelength of 13.5 nm, enabling printing of details of dimensions down to tens of nanometers [6]. Furthermore, multilayer based optics for wavelengths from a few nanometers up to several tens of nanometers are required in fields of material analysis such as soft x-ray to EUV spectroscopy, space telescope applications, synchrotron and x-ray free electron laser beam lines [7,8].

This work presented in this dissertation is mainly inspired by the study and development of optical molybdenum/silicon (Mo/Si) multilayer structures which are of relevance for EUV optical lithography. The work has been carried out at the nanolayer Surfaces and Interfaces (nSI) department at the FOM Institute for Plasma Physics Rijnhuizen, within an industrial partnership program (IPP) with ASML and Carl Zeiss STM GmbH. The contributions of previous PhD research projects within this partnership program involve improved knowledge on oxidation resistive protective capping layers [9], multilayer thermal stability [10,11] and surface contamination diagnostics and cleaning [12]. This thesis addresses the fundamentals and control of the morphology evolution of Si thin-films and Mo/Si multilayer structures during growth, which is of utmost importance to achieve the best possible optical performance of such mirrors. Chapters 2 to 4 are devoted to ion-enhanced layer growth and smoothening conditions enabling the deposition of the smoothest planar thin-film surfaces and multilayer interfaces. Deposition of layered structures on a flat substrate can be regarded as a special case of three-dimensional (3D) morphology control of layers deposited on a substrate of arbitrary shape. In the above mentioned fields of optical multilayer applications, multilayer-on-grating structures can offer enhanced spectral selectivity. These structures are non-trivial to produce because of stringent demands on substrate quality and multilayer deposition conditions, and specific knowledge on 3D Mo/Si multilayer growth was unavailable. The second half of this thesis (chapters 5 to 7) focuses on spectral filtering applications of multilayer-grating systems, and developing a comprehensive understanding of the morphology of multilayers deposited on structured substrate topographies. This work has led to the deposition of prototypical high-EUV reflective, patterned multilayers of which the diffractive properties have been demonstrated.

II. EUV Multilayer Bragg-reflectors

Consider linear, isotropic, non-dispersive media having field-, direction-, and frequency-independent electric and magnetic properties. For these general media the transmission t and reflection r coefficients at the interface, for electromagnetic waves traveling from material 1 to 2, can be determined from the Maxwell equations. This yields the well know Fresnel equations as given by equation (1.2):

$$r_s = \frac{\cos(\theta_i) - {}^{n_2}\!/_{n_1}\cos(\theta_t)}{\cos(\theta_i) + {}^{n_2}\!/_{n_1}\cos(\theta_t)}\,, \qquad r_p = \frac{{}^{n_1}\!/_{n_2}\cos(\theta_t) - \cos(\theta_i)}{{}^{n_1}\!/_{n_2}\cos(\theta_t) + \cos(\theta_i)} \qquad (1.2\ )$$

$$t_s = \frac{2\cos(\theta_i)}{\cos(\theta_i) + {}^{n_2}\!/_{n_1}\cos(\theta_t)}\,, \qquad t_p = \frac{2\cos(\theta_i)}{{}^{n_2}\!/_{n_1}\cos(\theta_i) + \cos(\theta_t)}$$

The angles of incidence and transmission, as measured from the surface normal, are given by θ_i and θ_t, respectively. The squared values of r^2 and t^2 give the total intensity reflected and transmitted, and the subscripts refer to s- and p-polarized radiation. The transmission and refection depend on the refractive indices denoted by n, which generally consists of a real and a imaginary component representing the phase speed of the propagating wave and the extinction coefficient, respectively. These two terms in the refractive index arise from interactions of photons with material intrinsic electron densities, and can be expressed in terms of scatter factors f_1 and f_2:

$$n = 1 - \delta + i\beta = 1 - \frac{r_0\lambda^2}{2\pi} N_{at}(f_1 - if_2), \text{ with} \qquad (1.3)$$

$$\delta = \frac{r_0\lambda^2}{2\pi} N_{at} f_1, \qquad \beta = \frac{r_0\lambda^2}{2\pi} N_{at} f_2 .$$

Here r_0 is the electron radius, N_{at} the atomic density and λ the wavelength. The photon energy is defined as $E = hc/\lambda$, with h the Planck constant and c the speed of light in vacuum. The value of f_1 relates to the number of electrons per atom involved in the interactions with an incoming photon, and approaches the atomic number at high photon energies i.e. small wavelengths. The real part of the refractive index $1-\delta$ will hence approach unity with reducing wavelength ($\delta \propto \lambda^2$). The absorption coefficient β strongly varies with photon energy, since f_2 shows abrupt jumps near absorption edges. Typically, for the wavelength range from EUV down to hard x-rays, transmission lenses cannot be applied for above reasons.

Given the low optical contrast in δ, reflectance efficiencies at the interface between all thinkable materials are rather low at near normal angles of incidence, and the highest value would be in the order of 1% in the EUV wavelength range. Much higher values can be obtained from a multilayer mirror in which successive interfaces, positioned at appropriate distance, contribute in-phase to the reflectance. When a two-material system of self-repeating bilayers is considered, the additional optical path length for reflection at a deeper interface should give rise to a 2π-phaseshift for constructive interference, as is illustrated in Fig.1.1. From this requirement it can be derived that the desired structure should fulfill the Bragg-condition for constructive interference (equation (1.4)), with d_1 and d_2 the individual layer thicknesses and $j \geq 1$ the Bragg-order in specular reflectance:

$$j\lambda = 2\Lambda_z \cos(\theta_i)\sqrt{1 - \frac{2\bar{\delta}}{\cos^2(\theta_i)}}, \text{ with } \Lambda_z = d_1 + d_2 \text{ and} \qquad (1.4)$$

$$\bar{\delta} = \frac{d_1\delta_1 + \delta_2 d_2}{d_1 + d_2}$$

The bilayer thickness, i.e. Λ_z, is also referred to as d-spacing or period. The selection of multilayer materials is primarily based on the absorption, which should be as low as possible. The reflectance is further constrained by the number of bilayers (absorption limited) and the optical contrast between the materials. Based on this consideration molybdenum and silicon are the preferred choice for EUV multilayers, were Mo is the reflector layer and Si the spacer layer. The scattering factors for both materials are depicted in Fig.1.2. The bilayer thickness and individual layer thicknesses yielding optimized EUV reflectance at a wavelength close to 13.5 nm, can be obtained by iterative application of equation (1.2) while taking the phaseshift into account, resulting in $\Lambda_z = 6.95$ nm, and a Mo to bilayer thickness ratio Γ of 0.4. A Mo/Si multilayer of 50 bilayers with these values for Λ_z and Γ yields a peak reflectance of 74% for an idealized two-layer system (Fig.1.3).

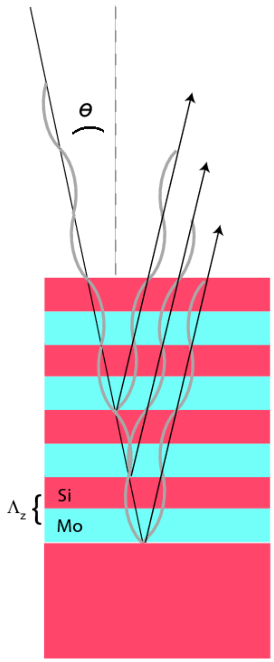

Fig.1.1 Constructive interference in a multilayer structure.

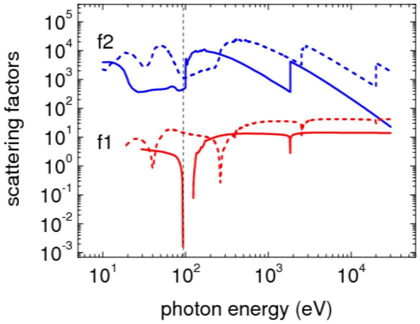

Fig.1.2 Scattering factors f_1 and f_2 plotted as a function of photon energy for Si (solid lines) and Mo (dashed line). A 10^3 offset is applied in f_2 for imaging purposes.

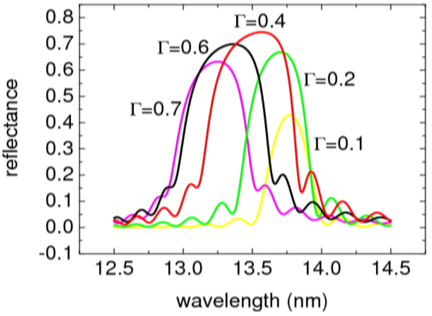

Fig.1.3 Reflectance versus wavelength of 50 bilayer Mo/Si multilayer at $\Lambda_z = 6.95$ nm and various Mo to bilayer thickness ratio Γ.

III. Imperfect interfaces

In the above considerations a perfect bilayer system was assumed, but in practice deviations from this idealized representation will be inevitable. The multilayer interfaces will always have a certain thickness, caused by intermixing and compound formation, and correspondingly the optical constants will change gradually from one layer to the other. The cumulative effect can be described by a Gaussian interface profile, resulting in a multilayer reflectance which is modified according to equation (1.5). The exponent is known as the Debye-Waller factor [3], and σ defines the Gaussian width.

$$R(\sigma) = R_0 e^{-(\frac{2\pi j\sigma}{\Lambda_z})^2} \tag{1.5}$$

The ratio σ / Λ_z indicates absolute reflectance decrements that can be as large as several percent, even at interface widths on the scale of 0.1 nm.

Equation (1.5) is commonly adopted to describe the influence of interface roughness as well, although this approach is only strictly valid in the special case of roughness of typical lateral dimensions smaller than the wavelength. Roughness of larger lateral scale will induce scatter in non-specular directions, causing imaging resolution decrements besides reflectance losses. A Bragg-condition for positive interference of diffraction from in-plane structures rather than from in-depth structures can be formulated, similar to equation (1.4), and is given by:

$$\Lambda_x (\sin(\theta_m) - \sin(\theta_i)) = m\lambda, \tag{1.6}$$

with Λ_x indicating an in-plane distance, and θ_m the (non-specular) normal angle of diffraction of order m. Equation (1.6) is also known as the grating equation since commonly used to obtain the angular positions of the diffraction orders from gratings. The periodic lateral grating structure of length Λ_x is then referred to as the grating pitch. In the case of interface roughness, Λ_x spans a continuous range in length scales and no distinct orders in diffraction arise. Typically the scatter will be diffuse and strongest in first order ($m = 1$). Still, for a multilayer structure with rough interfaces, multiple resonant peaks in the scatter can be distinguished. A method of visualizing the combined implication of the Bragg-conditions equation (1.4) and (1.6) is to express the reflection and scattering processes in terms of the momentum transfer from the multilayer to the incoming photon, which is given by $2\pi j / \Lambda_z$ in $\vec{z}$ (perpendicular to the multilayer) and $2\pi m / \Lambda_x$ in $\vec{x}$ (in the multilayer plane). All reflection and scattering/diffraction events must relate to a position on the Ewald-sphere as illustrated in Fig.1.4, dictated by conservation of momentum. In the case of perfectly smooth multilayer interfaces, momentum transfer is directed solely in $\vec{z}$, and at a given angle of incidence of an incoming photon this yields a single intersection with the Ewald-sphere. In the presence of interface roughness momentum can be transferred into x direction. The continuous range in momentum-space is referred to as Bragg-sheet, and enables intersections with the Ewald-sphere at each discrete amount of momentum transferred in $\vec{z}$. While in applications of optical elements scattering is usually considered as undesirable, x-ray scatter analysis has developed to an important non-destructive technique for characterization of thin film and multilayer interface- and surface roughness [13-15].

IV. Ion modified layer growth

The heterogeneous multilayer structure, chemical reactivity of the layer materials, and the use of non-crystalline fused silica based optical substrates, generally obstruct the possibility of 2D epitaxial multilayer growth. As a result, the leading technique for multilayer fabrication is physical vapor deposition (PVD) at room temperature. Layers are deposited by exposure of a substrate to a particle plume of the desired layer material which condenses to a solid layer. The deposition conditions are usually close to the kinetic limit of layer growth via stochastical addition of atoms with low lateral mass transport. At grazing angles of incidence self-shadowing effect during PVD can result in columnar layer growth [16]. Such layers may have optical or electronic properties governed by the physical layer structure and are referred to as meta-materials [17]. For near normal deposition conditions, as applicable for Mo/Si multilayer, PVD yields amorphous Si or polycrystalline Mo layers with a closed layer structure [18].

The stochastical kinetic limit of layer growth dictates that the layer roughness increases with the square root of the deposited thickness, as will be further addressed in the next paragraph. The morphology of thin layer surfaces can be modified by applying a bombardment with noble gas ions of energy in the order of 100 eV, in order to obtain smooth surfaces. On polycrystalline layers, ion bombardment can have undesired effects such as an increase of surface roughness levels [19]. On amorphous layers however, or layers which quickly become amorphous during ion bombardment (such as crystalline Si [20]), it can lead to enhanced layer quality in terms of density and smoothness. The ion surface interactions will remove surface atoms (sputtering) and induce redistributing processes to occur in a near-surface layer and can be applied either during growth or thereafter. The latter possibility enables dosing the ion flux such that buried interfaces are not affected [21].

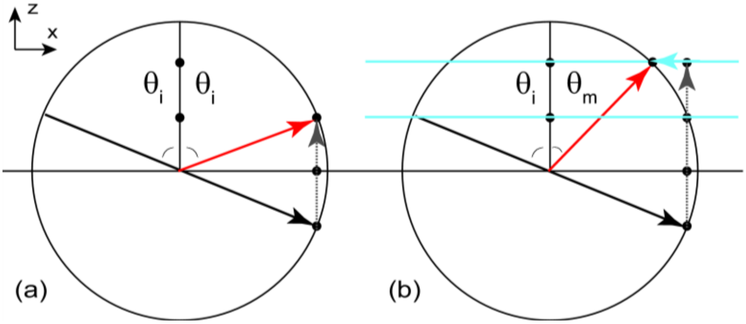

Fig.1.4 Ewald-spheres in momentum space. **(a)** The case of smooth interfaces and specular reflection (red arrow). Discrete momentum transfer in $\vec{z}$ (dashed) is indicated by (multiple) black dots **(b)** The case of rough interfaces; besides into $\vec{z}$ momentum can be transferred within the Bragg-sheet (blue arrow).

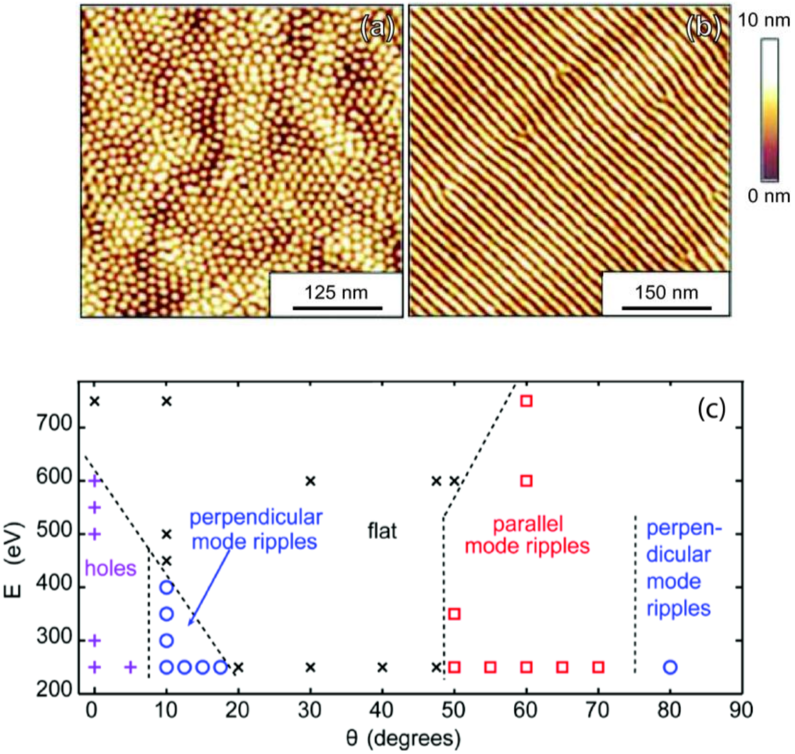

Fig.1.5(a) Surface height profiles determined by atomic force microscopy of ion-induced dot-like structures and **(b)** corrugations at Si, see reference [24]. **(c)** Phase-diagram of ion-induced morphologies on Ar^+-sputtered Si wafers at a typical ion fluence of 10^{18} cm^{-2}, obtained from reference [22]. Ion energy (vertical) versus normal angle of incidence (horizontal).

The ion-induced mass redistribution leads to a rich variety of possible surface morphologies depending on ion beam parameters such as angle of incidence, energy, and ion species (i.e. mass and size of the ions). Ions impinging a surface at near normal incidence can induce hole and dot-like surface structures (Fig.1.5(a)), and at grazing angles of incidence surface corrugations are reported (Fig.1.5(b)) [22-24]. For a range of angles of ion incidence up to approximately 50° from the surface normal, a regime is identified were smooth surfaces are stable under ion sputtering. These observations have been found to be generic for several ion species and energies at amorphous silicon (a-Si), and can be summarized in a phase-diagram [24] (Fig.1.5(c)).

A linear theoretical framework to interpret ion-induced morphologies was first proposed by Bradley and Harper [25], giving the topographical surface-height map $h(x,y)$ to evolve over a layer thickness t according to:

$$\frac{\partial h(x,y,t)}{\partial t} = v_2 \nabla^2 h(x,y,t) - v_4 \nabla^4 h(x,y,t), \qquad (1.7)$$

where v_2 and v_4 are proportionality coefficients. Equation (1.7) was proposed to account for surface roughening as caused by surface curvature depending sputter yield variations and smoothing by surface diffusion (proportional to the second and fourth spatial derivative in h, respectively). By generalizing to isotropic surfaces, with $r^2 = x^2 + y^2$ and $q = 2\pi / r$, and taking the Fourier transform ($F[...]$), equation (1.7) can be simplified to:

$$\frac{dPSD(q,t)}{dt} = -b(q)PSD(q,t) + \Omega, \qquad (1.8(a))$$

with $b(q) = \sum_n v_n q^n$, and (1.8(b))

$$PSD(q,t) \equiv (1/A)\left|F[h(x,y,t]\right|^2. \qquad (1.8(c))$$

The factor $1/A$ provides normalization on the surface area and Ω represents an effective unit volume which is randomly deposited or removed (for layer growth or sputtering, respectively), thereby addressing the stochastical component in the layer roughness evolution. Equation (1.8c) defines the power spectral density (PSD), which represents the roughness spectrum of a surface as a function of spatial frequency f, with $q = 2\pi f = 2\pi / r$ and r the in-plane length scale of a sinusoidal perturbation from equilibrium. In optical scattering the angular distribution is inversely proportional to the spatial frequency, as given by equation (1.6) with $\Lambda_x = 1/f$, and PSDs are indispensible in scatter analysis. Furthermore, from equation (1.8(a-c)) it is apparent that the layer morphology evolution can conveniently be described in terms of PSDs. Integrating the PSD over a spatial frequency domain gives the root mean square (rms) roughness value σ on the corresponding integration interval:

$$\sigma^2 = \int PSD(q)qdq \qquad (1.9)$$

The rms roughness is a commonly used measure of surface roughness and can serve as input for the interface width in equation (1.5), yet lacking spectral information as present in the PSD.

In general terms equation (1.7) and (1.8) predict that the surface roughness will increase monotonically with increasing layer thickness in the absence of redistributing kinetics, relating to $b(q) = 0$. This applies to low energy deposition techniques, e.g. based on evaporation of target material where the energy of the deposited particles (0.1 eV) is low with respect to typical binding energies (>1 eV). In this case the rms roughness scales with the square root of layer thickness: $\sigma(t) \propto \sqrt{t}$. For $b(q) > 0$ the roughness will reach an equilibrium value in the corresponding Fourier component, proportional to the ratio $\Omega / b(q)$. This also applies to initially rough substrates, and consequently substrate roughness can be mitigated if higher than the equilibrium value. The instabilities of the smooth surface under ion sputtering, resulting in distinct patterns in corrugations, correspond to a positive growth rate of (a range of) Fourier components, hence $b(q) < 0$. Transitions between stable and unstable regimes arise due to the dependencies in the magnitude and sign of the proportionality coefficients v_n on ion beam parameters [26].

In the Bradley-Harper model the dispersion relation in ion-induced kinetics (1.8b) thus consists of a second and fourth order term ($n = 2$ and $n = 4$), where the destabilizing term (second order) was initially assumed to be sputter-induced, and the stabilizing term (fourth order) surface-diffusion driven. Since recently however, based on new experimental and theoretical insights [27] both processes are argued to be of minor importance in surface morphology evolution. Ion-induced surface currents (second order, either stabilizing or destabilizing depending on ion beam parameters) [28] and surface confined viscous deformations [29] (fourth order, stabilizing) are considered to dominate. These processes give rise to the same general form of the dispersion relation as proposed by Bradley and Harper, and the conceptual framework of equation (1.8(a-c)) hereby remains unchanged. In the work presented in this thesis (chapters 2 and 3), also a term corresponding to $n = 1$ in equation (1.8b) has been identified, and relates to the in-layer structure and annihilation of free-volume during ion sputtering of Si layers.

V. Towards 3D Bragg-reflector structures

The multilayer and thin layer growth conditions discussed so far all apply to planar layer structures, and can therefore be referred to as 2D. Bragg-reflectors which have, besides the in-depth layered structure, an in-plane periodic grating structure have great potential in many applications in the field of EUV and soft x-ray optics. The grating will diffract incoming radiation into multiple orders m of diffraction, where the specular diffracted order with respect to the average grating plane is defined as $m = 0$. Note that the angular position of the orders is given by equation (1.6) with Λ_x the in-plane grating pitch, and depend on the wavelength for $m \neq 0$. This dispersive nature can be exploited in order to increase the spectral resolving power of an optical element. For near normal angle of incidence and small angles of diffraction the inter-order separation is proportional to λ / Λ_x in close approximation, and to provide increased resolution in the EUV and soft x-ray wavelength ranges a pitch below 1 µm is typically required [30]. At much larger pitches, diffraction in EUV becomes negligible, but radiation of longer wavelengths still can be diffracted out of the optical path of the EUV. Hereby a multilayer-grating system can be employed as a spectral filter, as further discussed in chapters 5 to 7.

Multilayer-grating systems can be obtained pursuing several methods, having specific (dis)advantageous and implications for the device design. A straightforward principle, yet requiring state-of-the-art technology, is the etching of a grating structure in a planar multilayer. The grating profile is transferred into the multilayer starting from a pattern in photo- or electron-resist as a stencil for the grating design. The challenges mainly involve optimization and control of the etching process in order to minimize undesirable effects on the multilayer structure, regarding e.g. contamination, layer intermixing and increased roughness levels, and as such fall outside the scope of the work presented in this thesis, mainly focusing on multilayer deposition parameters. Within this context two classes of general manufacturing principles can be identified, which are discussed in the next sections V.1 and V.2.

V.1. Multilayer deposition on a grating substrate

A grating sample can be employed as a substrate onto which a multilayer is deposited. As is the case for flat substrates, this requires the highest quality in terms of roughness of the individual grating facets, and furthermore the facets should be flat. These requirements rule out the class of commercially available gratings produced by mechanical ruling techniques or holographic gratings with a sinusoidal profile. A particular type of saw tooth grating profile, or blazed grating, where the multilayer is deposited on the long grating facets, is considered a viable possibility (Fig.1.6(a)). Such gratings can be produced by anisotropic etching of crystalline Si, resulting in smooth grating facets along slow etching crystalline lattice plains such as [111]. However, at larges pitch sizes the highest quality requirements on the local flatness of the grating profiles can still not be reached routinely. Apart from this, research was needed on multilayer deposition on this type of facetted substrates, to obtain control of the replication direction and efficiency of a pre-defined grating substrate topography into the multilayer, as is addressed in chapter 6.

V.2. Integrated deposition of multilayer and grating

Since real grating substrates with an appropriate pitch size are yet not available, an alternative to the above described approach has been developed. The method is based on the local deposition of a single- or multilayer add-structure on a planar multilayer by applying a deposition mask, as described in chapter 7 and illustrated in Fig.1.6(b). Hereby rectangular grating structures can be produced. The mask is applied in contact with the planar multilayer to obtain a sharp projection, and can consist of a resist pattern, or a micro-mesh foil. The latter has the advantage that no chemical removal of the resist which can contaminate or damage the multilayer is required. Making use of resist however, will allow for smaller pitches and easy up scaling to large optical areas.

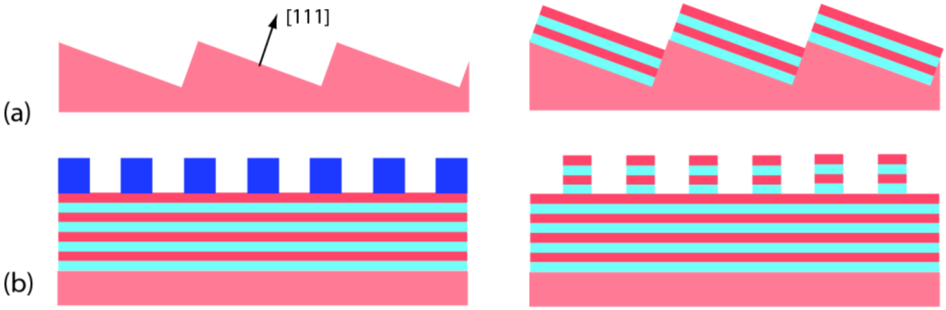

Fig.1.6 Schematic procedures of multilayer-grating manufacturing. The left column depicts the system before the critical processing step, and the right column the resulting structure. **(a)** (left) Blazed grating in crystalline Si, lattice planes coincide with the grating facets, (right) structure after multilayer deposition. **(b)** (left) Planar multilayer with contact mask (dark blue), (right) structure after add-multilayer deposition and mask removal.

VI. Experimental

VI.1. Layer deposition

All thin film and multilayer depositions described throughout this thesis have been performed using the physical vapor deposition facility as shown schematically in Fig.1.7. It consists of a vacuum system with a base pressure in the 10^{-9} to 10^{-8} mbar range. The layer deposition is performed from an evaporation plume, produced by an electron beam (e-beam) generated melt of target material in a crucible at the bottom of the vacuum system. According to the Maxwell-Boltzmann distribution for an ideal gas, the average energy of the evaporated particles is in the order of 0.1 eV, depending on melting temperature. The evaporated particles are deposited at the designated substrates, which are mounted at a substrate holder in line-of-sight of the target material melt at a distance of typically one meter. This deposition technique is characterized by low energy adatoms, hereby minimizing physical intermixing of the deposited layer with the layers underneath. Other characteristics are a low working pressure in the order of 10^{-7} mbar, resulting in a mean free path much longer than target-substrate distance, and small dimensions of the target melt. This yields a predictable deposited layer profile over large areas and an isotropic deposition flux.

A second available PVD technique is direct-current magnetron sputtering (see Fig.1.7). The sputter-target with a diameter of about 10 cm is kept at a relatively short distance from the substrate. A noble gas is ionized by a magnetron under the disk of target material, and a static magnetic field is used to deflect the obtain plasma towards the target upper surface. Target atoms are sputtered and will condense to a solid layer when reaching the substrate. Since operated in the plasma regime, magnetron depositions require a relatively high partial noble gas pressure of 10^{-5} mbar. Because of the deposition geometry and the mean free path, which is comparable to the target-substrate distance, the deposition profile and flux are less uniform than for e-beam evaporation PVD. Yet, the adatom energy that can be up to several electronvolt, as well as the backscattered sputtering ions and neutral particles reaching the substrate, can result in a stable and smooth growth over layer thicknesses up to micrometers. However, this process is more energetic process than e-beam evaporation, and can result in subsurface damage of the deposited layers and intermixing of buried interfaces.

Ions, used for surface treatment, ranging in energy from 50 to 2000 eV are produced by a Kaufmann source, which is mounted at an angle close to 50° with respect to the plane of the substrate holder. In the case of e-beam PVD of EUV high reflectance multilayers, enhancement of the layer growth characteristics by employing a noble gas ion bombardment is indispensible [31,32]. For the noble gas ion bombardment regime yielding smooth layers (see section 1.4), this treatment is also referred to as ion polishing and is frequently incorporated in the Mo/Si multilayer deposition process. Besides noble gas ion surface treatment a reactive ion bombardment can be applied. As is reported in chapter 3, bombardment of Si layers with H^+-ions have been employed to produce porous H rich a-Si layers.

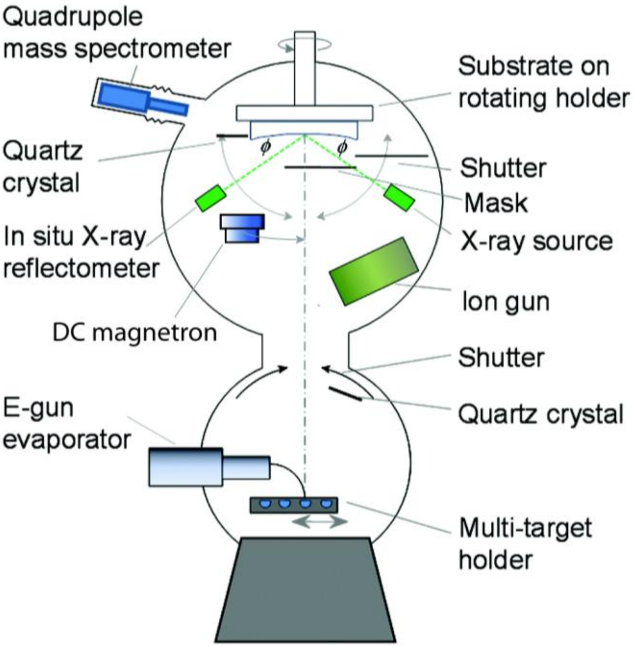

Fig.1.7 Schematic multilayer deposition facility

V1.2. In-situ layer thickness monitoring

The layer thickness is monitored by quartz crystal mass balances, which are mounted at several positions in the vacuum system near the substrate-holder. The quartz crystal resonant oscillation frequency depends on the mass deposited on the surface exposed to the deposition flux. Hereby a accurate relative measure of the deposition rate can be obtained, and given the density of the deposited layer is known, an absolute layer thickness can be derived. These diagnostics provide an indirect measure of the layer thickness on the actual substrates. For the purpose of local and absolute layer thickness control an *in-situ* reflectometer is used to measure the specular reflection of the multilayer during growth, on a monitor sample mounted in the centre of the rotating substrate holder. It operates at the C-K_α soft x-ray emission band at a wavelength of 4.47 nm. For a typical Mo/Si EUV multilayer, the contributions to the reflected signal are absorption limited to the top five bilayers. Hence, the average thickness over five bilayers is controlled and thickness errors in individual layers are compensated for during a later stage of the deposition.

VII. Scope and outline

This thesis is devoted to the study of ion modified layer growth conditions, appropriate for the production of optical Mo/Si multilayers of the highest quality. Main focus is on noble gas ion interactions with thin silicon layers, and the resulting surface and interface morphologies including, but not limited to, the special case of smooth planar layers. The aim was to extend the fundamental knowledge of the processes involved, and to indicate routes to further optimization and new applications.

In a conventional multilayer deposition on the smoothest possible substrates (which often are extremely valuable and difficult to produce), the ion polishing treatment mainly serves to mitigate layer growth intrinsic roughness. In chapter 2 the ion polishing process of relatively thick a-Si layers at much higher ion fluence is examined, in order to suppress substrate roughness prior to the deposition of a multilayer. The substrate roughness level, the sputtered layer thickness and ion energy have been varied. The sputtered layer thickness was found to be the key parameter in optimizing smoothening, giving a significant improvement of the EUV reflectance of subsequently deposited multilayers. Bulk-like viscous deformations are indicated to govern the smoothening process, which relate to the in layer free volume as annihilated during ion polishing.

Based on these results, extended experiments on the influence of the buried layer structure on the morphology of ion sputtered Si have been performed as described in chapter 3. Porous hydrogen rich a-Si layers with a significantly lower density than as deposited a-Si layers were prepared. The enhanced smoothening of these porous layers under ion sputtering has been verified and corresponds to the mechanism identified in chapter 2. Hereby ultrasmooth Si layer surfaces were obtained.

In chapter 4 the dependency of the noble gas ion polishing species, in order of increasing mass: neon (Ne), argon (Ar), krypton (Kr), and xenon (Xe), on the interface structure in Mo/Si multilayers has been studied. To probe the (buried) interface structure, scattering experiments with x-ray were performed, showing a preferential role for the more massive species to obtain the smoothest interfaces. Besides interface structure, the influence of noble gas incorporation in the layers on EUV reflectance has been studied.

As described in section 1.5, the increased spectral selectivity of multilayer Bragg-reflector grating systems has promising applications. Multilayer-grating systems can be a rigorous, high EUV throughput solution to reduce parasitic longer wavelength radiation, referred to as out-of-band radiation, present in EUV source emission spectra. This is of utmost importance considering the foreseen plasma based light sources bright enough for high volume manufacturing in EUV lithography. In chapter 5 the possibility to employ a multilayer applied at a blazed grating as an ideal spectral filtering device, which can be operated without sacrificing EUV reflectance, is described. Successful deposition of multilayers on gratings requires extended knowledge of layer growth on arbitrary facetted substrate profiles. A pioneering study to the growth and characterization of multilayers on a non-flat, step-edge substrate topography is presented in chapter 6. The direction of the substrate profile replication into the multilayer structure was found to depend on the local angle of incidence of the deposition flux, while the ion-enhanced growth affects the substrate profile replication efficiency. The results indicate that the multilayer deposition conditions enable high reflectance multilayer deposition on exotic substrate topographies like blazed gratings, given that the substrate meets the highest demands on roughness and profile quality. Unfortunately these demands are found to be beyond the current state-of-the-art in grating manufacturing. As is presented in chapter 7, an unconventional multilayer deposition scheme has been developed to produce rectangular multilayer-grating systems (briefly addressed in section 1.5.3), which show record EUV reflectance values while the reflection of longer wavelength radiation is strongly suppressed.

VIII. References

[1] D. Attwood, Soft X-rays and Extreme Ultraviolet Radiation – Principles and Aplications, Cambridge University Press, Cambridge, (1999).

[2] E.G. van Putten, D. Akbulut, J. Bertolotti, W.L. Vos, A. Lagendijk, and A.P. Mosk, Phys. Rev. Lett. **106**, (2011).

[3] E. Spiller, Soft X-Ray Optics, SPIE Optical Engineering Press, Bellingham (1994), and references therein.

[4] J.H. Underwood and T.W. Barbee, Nature **294**, (1981).

[5] R.P. Haelbich and C. Kunz, Opt. Commun. **17**, (1976).

[6] J. Benschop, V. Banine, S. Lok, and E. Loopstra, J. Vac. Sci. Technol. B **26**, (2008).

[7] D. L. Voronov, R. Cambie, R. M. Feshchenko, E. Gullikson,H. A. Padmore, A. V. Vinogradov, and V. V. Yashchuk, Proc. SPIE **6705**, (2007).

[8] A.B.C. Walker, T.W. Barbee, R.B. Hoover, and J.F. Lindblom, Science **241**, (1988).

[9] T. Tsarfati, Thesis (PhD), Surface and Interface Dynamics in Multilayered Structures, University of Twente, (2009).

[10] I. Nedelcu, Thesis (PhD), Interface Structure and Interdiffusion in Mo/Si multilayers, University of Twente, (2007).

[11] S. Bruijn, Thesis (PhD), Diffusion Phenonena in Chemically Stabilized Multilayer Structures, University of Twente, (2011).

[12] J. Chen, Thesis (PhD), Characterization of EUV induced Contamination on Multilayer Optics, University of Twente, (2011).

[13] J. Bennett and L. Mattsson, Introduction to Surface Roughness and Scattering, Optical Society of America, Washington, D.C. (1999).

[14] P. Siffalovic, et al., GISAXS - Probe of Buried Interfaces in Multilayered Thin Films chapter in the book X-Ray Scattering, ed. Christopher M. Bauwens, NOVA Publishers, 2011, New York, ISBN: 978-1-61324-326-8.

[15] L. Peverini, I. Kozhevnikov, and E. Ziegler, Phys. Stat. Sol.(a) **204**, (2007).

[16] M.M. Hawkey and M.J. Brett, J. Vac. Sci. Technol. A **25**, (2007).

[17] V.M. Shalaev, nature photonics **1,** (2007).

[18] R.W.E. van der Kruijs, E. Zoethout, A.E. Yakshin, I. Nedelcu, E. Louis, H. Enkisch, G. Sipos, S. Müllender, and F. Bijkerk, Thin Solid Films **515**, (2006).

[19] R. Schlatmann, C. Lu, J. Verhoeven, E.J. Puik, and M.J. van der Wiel, Appl. Surf. Sci. **78,** (1994).

[20] C. S. Madi, B. Davidovitch, H. B. George, S. A. Norris, M. P. Brenner, and M. J. Aziz, Phys Rev. Lett. **101**, (2008).

[21] A.E. Yakshin, E. Louis, P.C. Görts, E.L.G. Maas, F. Bijkerk Physica B **283,** (2000).

[22] F. Frost, B. Ziberi, A. Schindler, and B. Rauschenbach, Appl. Phys. A **91**, (2008).

[23] C. S. Madi, B. Davidovitch, H. B. George, S. A. Norris, M. P. Brenner, and M. J. Aziz, Phys Rev. Lett. **101**, 246102 (2008).

[24] C.S. Madi, H. Bola Gearge, M.J. Aziz, J.Phys.: Condens. Matter **21**, (2009).

[25] R.M. Bradley and J.M.E. Harper, J. Vac. Sci. Technol. A **6**, (1988).

[26] S. Vauth and S. G. Mayr, Phys. Rev. B **75**, (2007).

[27] C.S. Madi, E. Anzenberg, K.F. Ludwig, Jr., M.J. Aziz, Phys. Rev. Lett. **106**, (2011).

[28] M. Moseler, P. Gumbsch, C. Casiraghi, A.C. Ferrari, and J. Robertson, Science **309**, (2005).

[29] C. C. Umbach, R. L. Headrick, and K. -C. Chang, Phys. Rev. Lett. **87**, (2001).

[30] D.L. Voronov, M. Ahn, E.H. Anderson, R. Cambie, C.-H. Chang,E.M. Gullikson, R.K. Heilmann, F. Salmassi, M.L. Schattenburg, T. Warwick, V.V. Yashchuk, L. Zipp, and H.A. Padmore, Opt. Lett. **35**, 2615 (2010).

[31] H. -J. Voorma, E. Louis, F. Bijkerk, and S. Abdali, J. Appl. Phys. **82**, (1997).

[32] E. Louis, A. Yakshin, T. Tsarfati, and F. Bijkerk, Prog. Surf. Sci, (2011), doi:10.1016/j.progsurf.2011.08.001

Chapter 2

Surface morphology of Kr^+-polished amorphous Si layers

A.J.R. van den Boogaard, E. Louis, E. Zoethout, S. Müllender, and F. Bijkerk

The surface morphology of low energy Kr^+-polished amorphous Si layers is studied by topographical methods as a function of initial substrate roughness. An analysis in terms of power spectral densities (PSDs) reveals that for spatial frequencies 2×10^{-2} - 2×10^{-3} nm^{-1}, the layers that are deposited and subsequently ion polished reduce the initial substrate roughness to a rms value of 0.1 nm at the surface. In this system, the observed dominant term in linear surface relaxation, proportional to the spatial frequency, is likely to be caused by the combined processes of a) ion-induced viscous flow and b) annihilation of (subsurface) free volume during the ion polishing treatment. Correspondingly, a modification of the generally assumed boundary conditions, which imply strict surface confinement of the ion-induced viscous flow mechanism, is proposed. Data on surface morphology is in agreement with the optical response in extreme ultraviolet (EUV) from a full Mo/Si multilayered system deposited onto the modified substrates.

I. Introduction

Many applications of thin-films critically depend on the smoothness of surfaces and interfaces. In this perspective, epitaxial (multi)layers can meet the highest quality demands, but generally require strictly defined deposition conditions. Ultrasmooth amorphous layers of nanometers thickness are more routinely realizable by employing ion-enhanced layer growth conditions. For the angular window 35°-60° from the surface normal, smooth Si surfaces have been shown to be stable under noble gas ion sputtering without strong dependence on ion species or energy [1], and typically have rms roughness values in the order of 0.1 nm. Besides of technological relevance, a further study to the stabilizing kinetics can contribute to a complete description of the surface morphology evolution in terms of ion beam parameters, including sharp transitions between stable and unstable regimes [2]. In this study is focused on a-Si physical vapor deposition (PVD) at room temperature, modified by low energy Kr^+ ions impinging on the surface at an angle of 50° from the surface normal. These conditions enable ion polishing of the Si layers and deposition of Mo/Si extreme ultraviolet (EUV) reflective multilayer systems with smooth interfaces [3-6].

The roughness evolution during the ion polishing process is discussed within the framework of a linear continuum model, as can be applied to amorphous thin-film surface morphology evolution down to the nanometer scale in the absence of large surface profile slopes. The evolution involves a growth-intrinsic and a substrate-replicated component [7,8]. As a function of layer thickness t, the surface morphology on the spatial frequency f domain is given by equation (2.1), in terms of two-dimensional power spectral densities (PSDs), see reference [9]:

$$PSD(q,t) = \frac{4\Omega}{2\pi}\frac{1-e^{-2b(q)t}}{b(q)} + e^{-2b(q)t}PSD(q) \equiv \Gamma_t[PSD(q)] \tag{2.1}$$

with, $$b(q) = \sum_i v_i q^i \,. \tag{2.2}$$

Here $q = 2\pi f$ and Ω is a nucleus volume. The polynomial $b(q)$ gives a measure of the kinetic processes with corresponding proportionality constants v_i, affecting the relaxation of surface roughness. For layer growth in the limit $\overset{\lim}{b \to 0}$, stochastical surface roughness arises due to the Poisson-like distribution of growth nuclei. For PVD deposition conditions, the energy of the evaporant (<1 eV) is low compared to typical binding energies, and stochastical roughening is considered to dominate the surface morphology. The combined effect of layer growth and subsequent ion-induced sputtering and surface relaxation follows from iterative application of equation (2.1), with indices *d* and *p* relating to the deposition ($\overset{\lim}{b \rightarrow 0}$) and ion polishing ($b(q) > 0$), respectively: $PSD(q,t) = \Gamma_t^p \Gamma_t^d [PSD(q)]$. At given spatial frequency q_c the latter expression will approach an asymptotic value of $2\Omega / \pi b(q_c)$ with increasing thickness, independent on the initial value ($t = 0$), of which an example is given in Fig.2.1. For $PSD(q_c, t = 0) = 4\Omega / \pi b(q_c)$, a monotonic decrease towards the asymptote is predicted. The corresponding morphology changes are therefore preferably studied on a model system with slightly elevated initial roughness levels, since expected modifications are unambiguous and more pronounced than on surfaces with initial roughness close to the asymptote (rms roughness ≈ 0.1 nm). In this chapter, a study to the roughness evolution of Kr$^+$-polished a-Si layers on substrate with programmed roughness levels is presented. In the experiments has been aimed for optimized substrate smoothing by upscaling the deposited and sputtered a-Si layer thickness. Analysis of the results is given in terms of PSDs as obtained by atomic force microscopy (AFM) and optical profiler measurements. Furthermore, the EUV reflectance from Mo/Si multilayers deposited on the modified substrate morphologies has been studies.

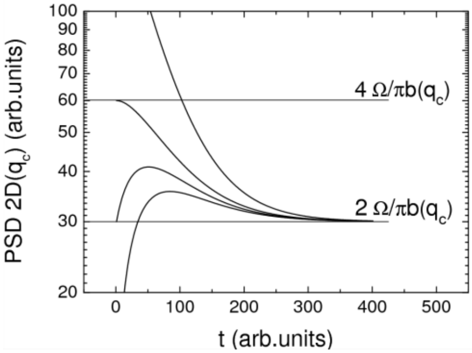

Fig.2.1 Calculated PSDs at given spatial frequency q_c and $\Omega = 0.6$ for different initial values ($PSD(q_c, t = 0) =$ 10, 30, 60, and 200), plotted as a function of deposited ($\overset{\lim}{b(q_c) \rightarrow 0}$) and removed ($b(q_c) = 0.05$) layer thickness t (all arb. units).

II. Experiments

II.1. Substrates and roughness characterization

Fused silica substrates with a programmed range in roughness levels were used. At three positions on each sample the two-dimensional surface profiles were measured by AFM and optical profiler pre- and post-deposition. The areas probed were 1×1 μm and 10×10 μm for AFM and 245×245 μm for the optical profiler with noise values of 0.03 nm, 0.05 nm, and 0.07 nm in rms roughness, respectively. By AFM, the spatial frequencies 10^{-1} – 3×10^{-4} nm^{-1} were probed while the optical profiler provided information on lower spatial frequencies, namely 3×10^{-4}-10^{-5} nm^{-1}. The substrate rms roughness varied from approximately 0.1 nm (referred to as superpolished) to 0.7 nm, as calculated by integrating over the entire spatial frequency range.

II.2. Deposition procedure

Experiments were performed at room temperature under high vacuum conditions with a base pressure of 10^{-8} mbar [10]. The PVD was performed from an e-beam generated vapor of the target material onto the substrates mounted in the vacuum vessel. Thickness control was provided by *in-situ* quartz-crystal mass balances and soft x-ray reflectometry on a Si monitor wafer mounted in the center of the substrate holder. A Kaufmann source was used to generate the Kr^+ beam. Continuous sample rotation (60 r.p.m.) was applied to enhance layer thickness uniformity and to suppress possible ion-induced ripple formation [11]. The deposition scheme of each experiment incorporated an initial layer of Mo of 2 nm thickness to enable grounding of the nonconductive substrates and inhibit charge building up during ion polishing. Subsequently, a Si layer of approximately 20 nm was deposited and removed afterwards by ion sputtering during the Kr^+ polishing at 50° normal angle of incidence. The Si deposition and polishing cycle were performed repetitively, where during the first cycle a 4-10 nm (depending on ion energy) excess Si layer served as a spacer layer to prevent Kr^+ interaction with the buried Mo/Si interface. The obtained thin-film system is referred to as Si single layer, in contrast to the Mo/Si multilayers optimized for EUV reflection, which were additively deposited on the Si single layers in a later stage.

The Kr^+ polishing was employed at 130 eV and 2 keV. Minimized ion-induced intermixing of subsurface interfaces, e.g. in multilayer systems, can be obtained at the lower energy regime [12], while at 2 keV the ion treatment volume has an in-depth extended range at given fluence due to the higher sputter yield. The Si single layer deposition/polishing cycles were performed 1, 5, and 18 times at 130 eV and 18 and 46 times at 2 keV during individual experiments. The maximum number of cycles at both energies was limited by experimental time. Typical removal rates were $R=10^{-2}$ nm/s and $R=7\times 10^{-2}$ nm/s for 130 eV and 2 keV ion polishing, respectively.

II.3. EUV specular reflectometry

After characterization of the surface morphology of the Si single layers, a 50 bilayer Mo/Si multilayer optimized for EUV reflectance was deposited on the samples. Per bilayer 0.5 nm Si was removed by 130 eV Kr^+ polishing. The effect of the surface morphology modifications have been examined by reflectance characterization. For comparison, Mo/Si multilayers were co-deposited on substrates with varying roughness without application of Si single layers. Near-normal (1.5° angle of incidence) specular EUV reflectance was measured by the Physikalisch-Technische Bundesanstalt at the electron storage ring BESSY II in Berlin [13].

III. Results and Discussion

III.1. PSD analysis

From topographical height profiles obtained by AFM and optical profiler (Fig.2.2), combined PSDs on the spatial frequency range 10^{-1} - 10^{-5} nm^{-1} were extracted. The typical shape of the PSD curves suggests a division in three spatial frequency domains (Fig.2.3(a)). At the very high spatial frequencies, i) 10^{-1} - 2×10^{-2} nm^{-1}, the PSDs pre- and post-deposition show differences in the order of the noise level of the AFM measurements. At spatial frequency domain ii), 2×10^{-2} - 10^{-3} nm^{-1}, the substrate roughness is significantly reduced. This domain tends to expand towards lower spatial frequencies with the number of Si single layer cycles, but the dependency is only moderate. At spatial frequencies iii) 10^{-3} nm^{-1}, no significant differences in PSD pre- and post-deposition are observed and the substrate morphology is fully replicated.

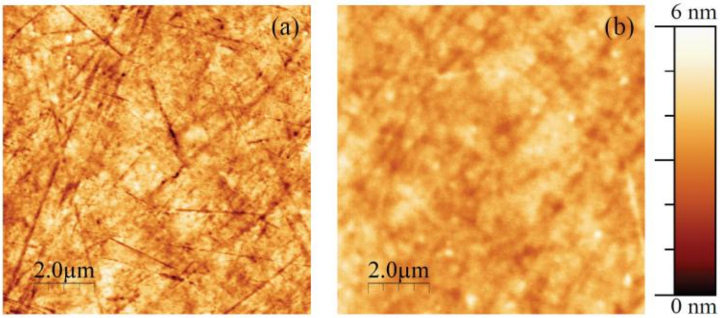

Fig.2.2 Substrate and 18-cycle 130 eV Si single layer AFM topographies, **(a)** pre-deposition, rms = 0.51 nm, **(b)** post-deposition, rms = 0.17 nm.

An overview of the roughness mitigation has been obtained by calculating the rms roughness values for spatial frequencies 2×10^{-2} - 2×10^{-3} nm^{-1} (Fig.2.3(b)). The low correlation in rms roughness pre- and post-deposition indicates a restricted memory of substrate morphology for 18 Si single layer cycles or more, where the rms roughness approaches a lower limit of 0.1 to 0.14 ± 0.02 nm post-deposition, depending on initial substrate roughness. No ion energy dependence is observed, indicating that the layer surface morphology is mainly determined by the number of cycles, hence the total deposited and removed layer thickness.

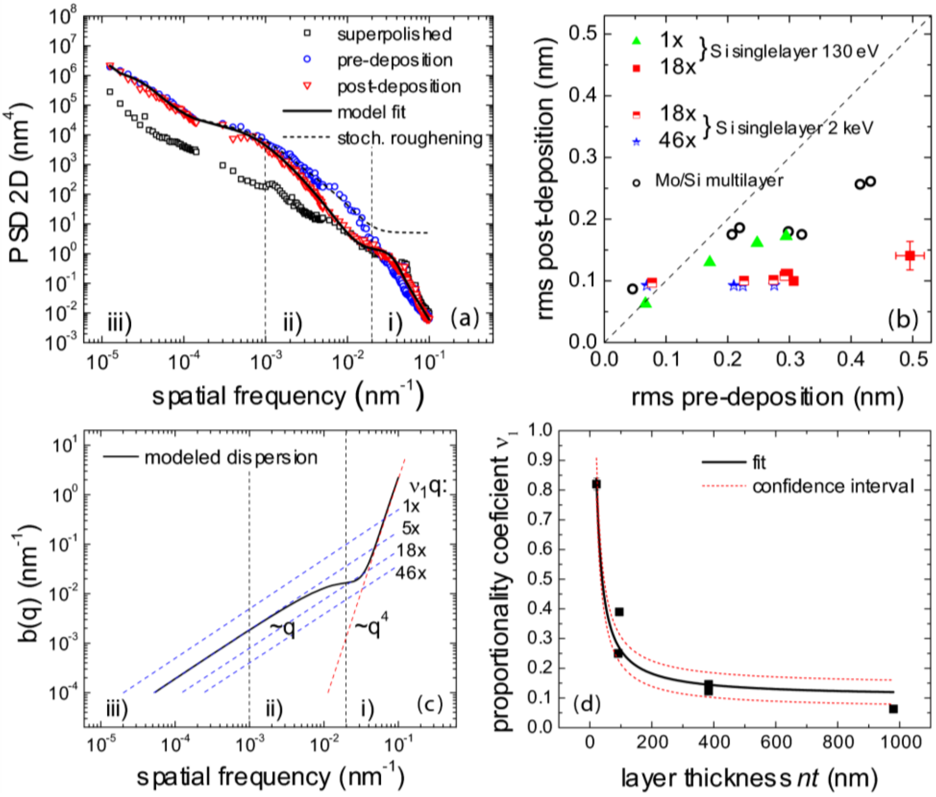

Fig.2.3 **(a)** Example of PSDs of a superpolished fused-silica substrate, and of a substrate of programmed roughness pre- and post-5-cycle 130 eV Si single layer deposition. A model fit to the data is shown, as well as the calculated layer PSD due to stochastical growth and removal only. **(b)** Post-deposition rms surface roughness as a function of initial substrate roughness (pre-deposition). Data averaged over three measuring points per sample, for spatial frequencies 2×10^{-2} - 2×10^{-3} nm^{-1}. **(c)** Typical dispersion relation equation (2.2), as obtained by the model fit to the measured PSDs (Fig.2.3(a)). The corresponding asymptote $\sim q^4$ is depicted, as well as $\sim q$ for the different Si single layers. **(d)** Proportionality coefficient ν_1 as a function of total layer thickness. The solid line represents a fit of equation (2.3) to the data for: Δt = 20 nm, V = 0.1 ± 0.04, V_0 = 0.89 ± 0.07. Confidence interval based on one standard error in V and V_0 is shown.

The framework of the continuum model has been employed for further analysis. Equation (2.1) was iteratively applied to the PSD of the substrate surface up to the total number of cycles n, denoted by the subscript: $PSD(q,t)_n = \Gamma_t^p \Gamma_t^d{}_{(n)} \Gamma_t^p \Gamma_t^d{}_{(n-1)} ... \Gamma_t^p \Gamma_t^d{}_{(1)} [PSD(q)]$. The number of fitting parameters was limited by choosing the unit cell Ω during both deposition and ion polishing equal to the average volume of a Si atom in amorphous Si, yielding 0.02 nm^3 at a density of 2.2 g/cm^3. During deposition, no kinetic processes were considered to be present and the corresponding parameters have been used in the limit $\overset{\lim}{b \rightarrow 0}$, while for ion polishing the proportionality coefficients in equation (2.2) were used as free-fitting parameters. The data for the superpolished substrates was excluded from the fitting due to low roughness values compared to experimental noise.

It is found that the linear model provides an accurate description of the data, of which an example is shown in Fig.2.3(a). As depicted in Fig.2.3(c), the dispersion as given by equation (2.2) is dominated by a term $\propto q$ for spatial frequencies $< 10^{-2}$ nm^{-1} and by a term $\propto q^4$ for spatial frequencies $> 3 \times 10^{-2}$ nm^{-1}. Herein between a negative proportionality in q^2 yields a local minimum, indicating less but still positive smoothing. The long range substrate smoothening at spatial frequency domain ii) thus predominantly relates to the dispersion $\propto q$. Significant smoothing is restricted to domain ii), whereas at the typically low magnitude of the substrate PSD at domain i) the contribution of stochastical roughness is relatively large. At domain iii) stochastical roughening and ion-induced kinetics are negligible.

It is noticed that the fitting parameters ν_i decrease with the number of smoothing layer cycles. This observation is particularly significant for ν_1 (Fig.2.3(d)), being mainly determined by data of high signal-to-noise ratio at spatial frequencies where the higher-order terms in kinetics are negligible (domains ii and iii). As now will be derived, this might indicate ν_1 gives an effective measure of multiple linear stages in kinetics $\propto q$. Since stochastical roughening is small as compared to substrate PSD at domains ii) and iii), the left term on the righthand side of (2.1) can be neglected, explicitly listing the dependence on ν_1: $PSD(q,t,\nu_1)_n = e^{-2\nu_1 nt} PSD(q)$ with nt is the total removed layer thickness. The roughness evolution accordingly becomes a simple exponential function. Consider the kinetics to have an initially elevated value V_0, e.g. during the first cycle, and a value V during all later stages; $\nu_1 \rightarrow V_0$ for $t \leq \Delta t$ and $\nu_1 \rightarrow V$ for $\Delta t < t \leq nt$, yielding the exponent to become $-2(V(nt - \Delta t) + V_0 \Delta t$. When bound to a single model parameter ν_1^*, it will transform under the stated substitution to the weighted mean over the stages in surface-relaxing kinetics, as in this example:

$$\nu_1^*(nt, \Delta t, V_0, V) = \frac{V(nt - \Delta t) + V_0 \Delta t}{nt}. \qquad (2.3)$$

The main trend in the data is explained by equation (2.3). It follows that $V_0 > V$, although the value of V_0 and V cannot be determined uniquely without *apriori* assuming a layer thickness of Δt. In consequence the initially elevated rate in smoothing kinetics cannot further be quantified at this point but its occurrence may be related to a structural or chemical non-equilibrium of the deposited Si single layer prior to completion of the first ion polishing cycle and primary treatment of the subsurface Mo/Si interface region with Kr^+ ions.

III.1.a Free volume annihilation

The dispersion relation $b(q)$ as obtained by the model fitting procedure reveals the fundamentals of the ion-induced surface modification. The proportionality with $-q^2$ is generally interpreted as a fingerprint of roughening due to local surface curvature-dependent sputter yield variations [14], or ion-driven surface currents [15]. The q^4 dependency may either represent surface diffusion [16,17], or surface-layer-confined viscous flow [18]. The latter effect is argued to be dominant for ion-damaged disordered surfaces [19,20], similar to the surfaces under consideration. The constraint of surface-confined viscosity implies the boundary condition of no slip at the viscous liquid-solid interface and relates to the restricted penetration depth of the ions. However, the term $\propto q$ in the dispersion is traditionally explained as caused by bulk viscous flow [16,17], having an in-depth extension into the system $> 1/q$ nm [18]. Although occurrence of this process is physically inexplicable for the system under consideration due to the superficial character of the ion polishing treatment, the observed dispersion gives a robust indication of surface relaxation caused by mass transport extending the strict surface confinement of the ion-induced viscous layer. A revision of the mentioned model boundary condition is proposed to resolve this discrepancy.

Analysis of the critical angle in hard x-ray reflectance shows an increased density of e-beam PVD Si layers grown during simultaneous 130 eV Kr^+-assistance as compared to as-deposited layers (Fig.2.4). This effect is partly due to the incorporation of typically 1 at.% Kr into the a-Si, but based on each Kr atom replacing a Si atom in the amorphous matrix still 2.5% of the densification can be addressed to a decreased fraction of in-layer free volume. It is expected that the ion polishing treatment as applied to the as-deposited, relatively porous Si layers will give rise to a similar compaction, associated with ion-induced in-depth mass transport over short length scales. The mass transport as facilitated by the gradient in free volume from the dense ion-induced viscous layer to the underlying permeable material is referred to as free volume annihilation (FVA). Although the process of FVA opposes the gradient in free volume, it is maintained during ion polishing due to simultaneous sputtering and continuous renewing of the surface layer.

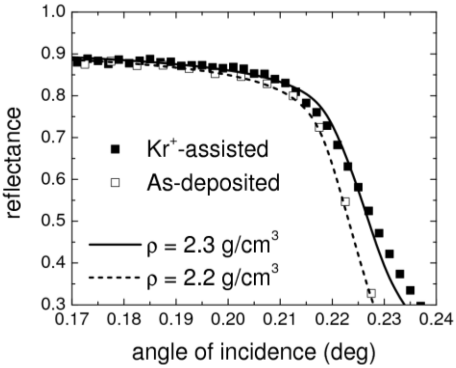

Fig.2.4 Reflectance of 0.154 nm Cu-K$_\alpha$ radiation from Si layers as a function of grazing angle of incidence. Measured data and simulations for two layer densities are shown.

Accounting for FVA requires small adjustments in the boundary conditions of the liquid-on-solid model proposed by Orchard [18], and will be demonstrated to resolve the discrepancy as stated above. The restriction of no slip at the interface between the a-Si and the ion-induced viscous layer (Fig.2.5(a)) is mitigated for in-depth mass transport in $\vec{y}$ (Fig.2.5(b)), with x and y the axes of a Cartesian coordinate system. The velocity at the interface $(x,-h)$ can be written as: $\vec{\upsilon}(x,-h)=(s_x,s_y)(-h)+(\omega_x,\omega_y)(x,-h)$. The constant term is attributed to uniform compacting mechanisms like ion-atom forward scattering events and can be ignored in further analysis. The position dependent term is attributed to stress opposing the free surface perturbations from equilibrium. In the absence of a rigid interface, the latter velocity component is assumed proportional to the viscosity limited velocity in an infinitely thick layer of sinusoidal perturbed fluid: in y direction [17], $\omega_y(x,-h)\propto -iqe^{iqx-qh}(qh+1)=-iqe^{iqx}+O(q^3)$. In close approximation (second order in q), this results in the following boundary conditions on the flow velocity at the $(x,-h)$ plane:

$$\upsilon_x(x,-h)=\omega_x(x,-h)=0 \text{ and,} \tag{2.4}$$

$$\upsilon_y(x,-h)=\omega_y(x,-h)=-i\frac{\gamma a}{2\eta}q\mu e^{iqx}.$$

Here γ is the surface tension, a is the amplitude of a Fourier component, η is the viscosity of the surface layer, and $0\le\mu\le1$ is a material and structural intrinsic proportionality constant representing the effective flow volume as compared to the case of an infinitely thick layer of viscous material ($\mu=1$). From equation (2.4), the rate of leveling of surface roughness can be calculated straightforwardly, in analogy with the method described in reference [18].

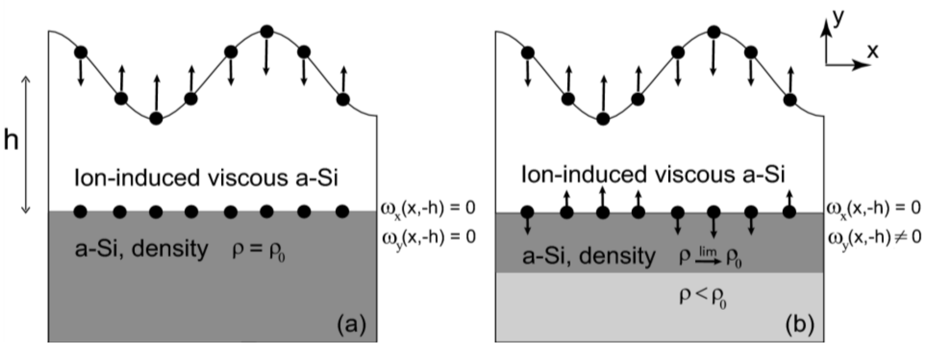

Fig.2.5 Schematic representation of surface confined viscous flow **(a)** for the condition of no slip at the liquid-solid interface at $(x,-h)$, **(b)** allowing for mass transport through the interface.

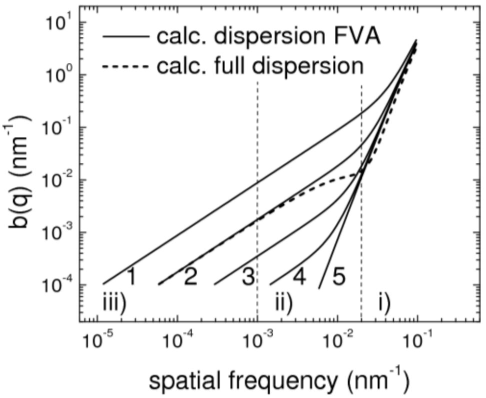

Fig.2.6 Calculated dispersion relation for parameter values in Table 2.I.

Dispersion curve#	$\gamma/(\eta R^*)$	μ
1	1.4×10^2	1.25×10^{-4}
2	1.4×10^2	2.5×10^{-5}
3	1.4×10^2	5×10^{-6}
4	1.4×10^2	1×10^{-6}
5	1.4×10^2	$< 10^{-7}$

*Removal rate (nm/s)

TABLE 2.I Parameter values corresponding to dispersion curves Fig.2.6.

Fig.2.6 shows the calculated dispersion for different values of μ (Table 2.I). The ion-induced viscous surface layer is taken to be 1 nm thick, $h = 1$ nm, in which the majority of the primary ion-atom collision events take place [21]. For the limiting values $\mu = 0$ and $\mu = 1$, the dispersions appears to result from surface-confined viscous flow ($\propto q^4$) and bulk viscous flow ($\propto q$), respectively. For values of μ in between these extreme, a transition from $\propto q$ to $\propto q^4$ for increasing spatial frequency is observed, unifying the two powers of spatial frequency, whereas both arise in the FVA model. When adding the empirically observed (negative) proportionality constant ν_2, full agreement of the modeled dispersion with experiment is obtained. For literature value γ = 0.7 Nm^{-1} [22], the found viscosity is η = 7×10^7 Pa s and η = 5×10^8 Pa s for R = 7×10^{-2} nm/s (2 keV Kr^+) and R = 10^{-2} nm/s (130 eV Kr^+), respectively. Making use of typical sputter yields of Si (0.1 and 1 atom/ion, for 130 eV and 2 keV Kr^+ respectively) [23,24], and the estimated number of ion-induced displacements per atom (dpa) in the ion treaded layer-volume (2.5 and 20 vacancies/ion, for 130 eV and 2 keV Kr^+ respectively) [21], the viscosities can be expressed as η = 1×10^8 Pa dpa, for both ion energies. This value is of the same order as obtained from classical MD simulations on 1 keV self-sputtering of a-Si [20]. The relation between μ and the internal structure of the Si layers is not revealed by the performed experiments but due to lower friction, μ is expected to increase with porosity of the Si layer, resulting in a further enhanced ion-induced modification of the surface morphology in the regime where the dispersion is proportional to $\propto q$. In this light, the enhanced kinetics during the first Si single layer cycle could be due to a lower density of the Si layer near the Mo/Si interface region.

III.3. EUV Reflectance analysis

Interface roughness in EUV-reflecting Mo/Si multilayers, partly replicated from the substrate, will induce diffuse scatter at the expense of specular EUV reflectance for spatial frequencies down to a lower limit f_{scat}, given by the expression [25]: $m\lambda f_{\mathrm{scat}} = \left|\sin(\alpha \pm \Delta\alpha) - \sin\alpha\right|$. Here α is the normal angle of incidence and specular reflection, $\Delta\alpha$ is the angular acceptance of the reflectometer detector from the specular beam, λ is the wavelength of the radiation, and m is the order of diffraction. Substrate morphology can therefore be related to specular EUV reflectance and vice versa. Si single layer modified substrates of varying roughness were applied with a Mo/Si multilayer for reflectance analysis, with f_{scat} = 6.7×10^{-4} nm^{-1} for the used reflectometer [13], neglecting orders in diffraction higher then $m = 1$. Scattered light from lower spatial frequency roughness will contribute to the measured signal.

EUV peak reflectance values are plotted as a function of the rms substrate roughness on the relevant spectral roughness interval (Fig.2.7(a)). To compensate for run- to-run reproducibility errors in multilayer periodicity, reflectance values are normalized to the reflectance of the superpolished *in-situ* monitoring sample having a roughness of approximately 0.1 nm. It is found that the decrease of substrate roughness by applying the Si single layers significantly enhances the EUV reflectance, although losses compared to untreated superpolished fused-silica substrates are still observed. On the substrates with rms roughness between 0.2 nm and 0.4 nm, application of the 46-cycle Si single layer results in a 3% higher peak reflectance (only marginally higher than obtained by application of the 18-cycle Si single layer), while at a roughness of 0.7 nm, up to 8% reflectance is gained by applying the 18-cycle 130 eV Si single layer. The independence of surface morphology modification on ion energy as observed by AFM measurements, is confirmed by the similarity in EUV reflectance at the 18-cycle Si single layer modified substrates. Fig.2.7(b) shows a similar reflectance analysis, but in terms of rms roughness of the surface upon which the multilayer is deposited: the substrate (for the reference samples) or the Si single layer surface. It follows that reflectance of multilayers on the Si single layer modified substrates coincides with the reference data (open circles), despite significant modification of surface morphology and corresponding differences in the shape of the PSD curves, revealing a critical dependence on rms roughness. Due to the similar roughness of the superpolished substrates and the most effectively smoothened substrates of programmed roughness (by application of 18- and 46-cycle Si single layer) at spatial frequency domains i) and ii), the remaining reflectance differences are explained by a still higher roughness at spatial frequencies 2×10^{-3} - 6.7×10^{-4} nm^{-1}. At theses spatial frequencies substrate roughness is efficiently replicated by the Si single layers.

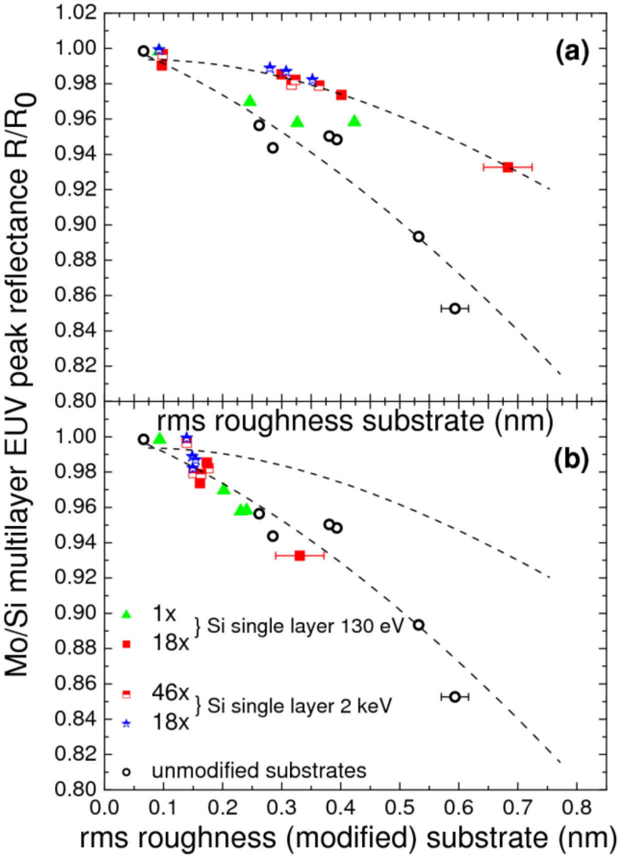

Fig.2.7 Normalized EUV reflectance from Mo/Si multilayers, with and without underlying Si single layer, on substrates with varying roughness at spatial frequencies 6.7×10^{-4} - 10^{-1} nm^{-1}. Fits through (○) and (■) serve to guide the eye. **(a)** Reflectance plotted against initial substrate roughness. **(b)** Reflectance plotted against starting roughness prior to Mo/Si multilayer deposition (substrate- or Si single layer surface roughness).

IV. Conclusions

A surface roughness analysis in terms of PSDs obtained from topographies determined by AFM and optical profiler, has revealed the possibility to apply e-beam PVD of Si and subsequent low energy Kr$^+$ polishing, to produce thin layers with a surface roughness which is significantly reduced as compared to the initial substrate roughness. An increasing number of Si single layer deposition and polish cycles (up to 46) has been applied, at each of which 20 nm of Si was deposited and removed by Kr$^+$ polishing. Integrated over the spatial frequency range 2×10^{-3} - 2×10^{-2} nm^{-1}, substrate roughness values were reduced by a factor three towards a value of 0.1 to 0.14 ± 0.02 nm. The surface morphology modification shows a critical dependence on the number of cycles, hence the total amount of deposited and removed material, rather than on ion energy. The linear model of roughness evolution is found to be in close agreement with the data, and the obtained dispersion in kinetics typically shows linearity in spatial frequency. This relation cannot be explained in terms of known mechanisms, such as surface confined viscous flow, where the viscous relaxation would take place in a strictly confined thin surface layer. The here suggested modification of the corresponding model boundary conditions allows for in-depth mass transport into the ion polished layer and agrees with the dispersion as observed. This mass transport is related to ion-induced annihilation of free volume in the Si layer which has, as-deposited, a relatively low density compared to the bulk material.

Applying these layer growth and ion polishing conditions on rough substrates prior to the deposition of a full Mo/Si multilayer reflective Bragg system enhances the EUV reflectance by up to 8%, which is in qualitative agreement with the observed ion-induced substrate smoothing. In particular the rms roughness at the relevant spatial frequencies is demonstrated to be a good indication of the EUV reflectance of such multilayer systems.

V. Acknowledgements

This work is part of the FOM Industrial Partnership Program I10 (‘XMO’) which is carried out under contract with Carl Zeiss SMT GmbH, Oberkochen, Germany and the ‘Stichting voor Fundamenteel Onderzoek der Materie (FOM)’, the latter being financially supported by the ‘Nederlandse Organisatie voor Wetenschappelijk Onderzoek (NWO)’.

VI. References

[1] F. Frost, B. Ziberi, A. Schindler, and B. Rauschenbach, Appl. Phys. A **91**, 551 (2008).

[2] C. S. Madi, B. Davidovitch, H. B. George, S. A. Norris, M. P. Brenner, and M. J. Aziz, Phys Rev. Lett. **101**, 246102 (2008).

[3] E. J. Puik, M. J. van der Wiel, H. J. Zeijlemaker, and J. Verhoeven, Rev. Sci. Instrum. **63**, 1415 (1992).

[4] E. Louis, H. -J. Voorma, N. B. Koster, L. Shmaenok, F. Bijkerk, R. Schlatmann, J. Verhoeven, Y. Y. Platonov, G. E. van Dorssen, and H.A. Padmore, Microelectron. Eng. **23**, 215 (1994).

[5] I. Nedelcu, R. W. E. van der Kruijs, A. E. Yakshin, F. Tichelaar, E. Zoethout, E. Louis, H. Enkisch, S. Müllender, and F. Bijkerk, Thin Solid Films **515**, 434 (2006).

[6] A. E. Yakshin, E. Louis, P. C. Görts, E. L. G. Maas, and F. Bijkerk, Physica B **283**, 143 (2000).

[7] W. M. Tong and R. S. Williams, Annu. Rev. Phys. Chem. **45**, 401 (1994).

[8] D. G. Stearns, Appl. Phys. Lett. **62**, 1745 (1993).

[9] R. Schlatmann, J. D. Shindler, and J. Verhoeven, Phys. Rev. B **54**, 10880 (1996).

[10] E. Louis, F. Bijkerk, L. Shmaenok, H. -J. Voorma, M. J. van der Wiel, R. Schlatmann, J. Verhoeven, E. W. J. M. van der Drift, J. Romijn, B. A. C. Rousseeuw, F. Voss, R. Dresor, and B. Nikolaus, Microelectron. Eng. **21**, 67 (1993).

[11] R. M. Bradley, Phys. Rev. E **54**, 6149 (1996).

[12] H. -J. Voorma, E. Louis, F. Bijkerk, and S. Abdali, J. Appl. Phys. **82**, 1876 (1997).

[13] C. Laubis, C. Buchholz, A. Fischer, S. Plöger, F. Scholz, H. Wagner, F. Scholze, G. Ulm, H. Enkisch, S. Müllender, M. Wedowski, E. Louis, and E. Zoethout, Proc. of SPIE **6151**, San Jose, (2006).

[14] R. M. Bradley and J. M. E. Harper, J. Vac. Sci. Technol. A **6**, 2390 (1988).

[15] M. Moseler, P. Gumbsch, C. Casiraghi, A.C. Ferrari, and J. Robertson, Science **309** (2005).

[16] C. Herring, J. Appl. Phys **21**, 301 (1950).

[17] W. W. Mullins, J. Appl. Phys **30**, 77 (1959).

[18] S. E. Orchard, Appl. Sci. Res. A **11**, 451 (1962).

[19] C. C. Umbach, R. L. Headrick, and K. -C. Chang, Phys. Rev. Lett. **87**, 246104 (2001).

[20] S. Vauth and S. G. Mayr, Phys. Rev. B **75**, 224107 (2007).

[21] J. F. Ziegler and J. P. Biersack, SRIM 2006.02 computer code, http://www.srim.org.

[22] *CRC Handbook of Chemistry and Physics* (CRC Press, Inc. Boca Raton, 1984).

[23] S. -M. Wu, R. van de Kruijs, E. Zoethout, and F. Bijkerk, J. Appl. Phys. **106**, 054902 (2009).

[24] J. Bohdansky, Nucl. Instrum. Methods Phys. Res. B **2**, 587 (1984).

[25] E. Spiller, *Soft X-ray Optics* (SPIE Optical Engineering Press, Bellingham, 1994).

Chapter 3

Influence of hydrogenic retention in a-Si films on ion-sputtered surface morphology

A.J.R. van den Boogaard, E. Zoethout, E. Louis, F. Bijkerk

Low energy Kr^+ exposure of a-Si:H layers is observed to result in enhanced surface smoothing as compared to intrinsic a-Si, yielding ultrasmooth <0.1 nm surfaces. This effect is demonstrated to be related to the presence of subsurface voids in the a-Si:H layers. An model on ion-induced quasi non-local viscous flow has been developed, showing close agreement with the data. The hereby obtained dispersion in smoothening kinetics correctly addresses the occurrence of bifurcations between stable and unstable surfaces under ion sputtering.

I. Introduction

The fundamentals governing amorphous thin film surface morphology evolution during deposition are under continuous attention. Such evolution is determinative for e.g. the electronic, mechanical, and optical characteristics of the films deposited. Ion bombardment with inert species is generally applied to produce smooth films of increased density for various amorphous layer systems [1-3]. Besides molecular dynamics simulations [4], or phenomenological models on surface growth (for an overview see reference [5]), analytic expressions on the influence of ion-induced redistribution processes such as viscous deformations, surface diffusion and sputtering processes have been derived. The latter advocate a linear evolution for the interesting regime of nanoscale roughness [5-9]. Likewise, the thickness evolution of the isotropic Fourier spectrum of the surface profile h, as a function of spatial frequency $q = 2\pi / r$ with r representing a in-plane length scale, can be given by

$$\partial h(q,t)^2 / \partial t = -b(q) h(q,t)^2 + \Omega , \qquad (3.1)$$

$$\text{with } b(q) = \sum_n v_n q^n . \qquad (3.2)$$

The exponents of q and corresponding proportionality coefficients v_n give the dispersion in layer growth kinetics, and the nucleus volume Ω accounts for stochastical roughening. Furthermore, equation (3.1) shows the power spectral density (PSD) of the surface, defined as $h(q,t)^2$, to approach an asymptotic value $\Omega / b(q)$ for increasing thickness t.

In literature the notion of low energy ion sputtering on amorphous solids causing liquid-like kinetics in a surface confined layer is addressed, and relates to $n = 4$ in above equations [10]. Previously the authors have reported on the observation of both $n = 1$ and $n = 4$ for sequentially physical vapor deposited (PVD) and Kr$^+$-sputtered a-Si surfaces. This indicates an in-layer directed viscous flow component as associated with subsurface free volume annihilation (FVA) [11]. The flow is considered a steady-state process occurring at relatively porous solids and is spatially located to a surface layer near the progressing sputtering front. Unlike the case of strictly surface confined viscosity, FVA flow can have a non-zero velocity over its in-depth range and is therefore referred to as quasi non-local. This study addresses the influence of the subsurface layer structure and most notably the subsurface free volume on the ion-induced surface morphology of a-Si films as measured using atomic force microscopy (AFM). The observation of improved surface smoothing of hydrogen rich a-Si layers under ion sputtering is explained and discussed in terms of a continuum model based on quasi non-local viscous flow.

II. Theoretical considerations

For quantitative analysis a viscous liquid-on-solid continuum model is employed, with an ion-induced viscous layer of thickness d above the interface, viscosity η, surface free energy γ, and sputter rate R, with $B \equiv \gamma / \eta R$, as was first reported in the classical paper of S.E. Orchard [9]. The mechanism of FVA is here postulated to be effectively described by a permeable interface in above model, implying that the condition of no slip at the liquid-solid interface is discarded. A perpendicular, viscosity limited (i.e. bulk) flow velocity component at the interface proportional to the dimensionless coefficient μ is considered to exist due to the permeability of the underlying solid [11]. Solving the two-dimensional Navier-Stokes equations for a sinusoidal disturbed surface from equilibrium and the stated boundary conditions in analogy with the method described in reference [9] yields the following expression:

$$b(q) = - qB \frac{2dq - 2\mu \cosh(dq) - 2dq\mu \sinh(dq) - \sinh(2dq)}{1 + 2d^2 q^2 + \cosh(2dq)} \qquad (3.3)$$

A priory examination of equation (3.3) indicates a dual character; the limiting cases of $\mu = 0$ and $\mu = 1$ relate to surface confined viscous flow and viscosity limited flow, respectively. For $0 < \mu < 1$ and spatial frequency q^*, a transition in the dispersion from $\propto q$ for $q < q^*$ to $\propto q^4$ for $q > q^*$ is predicted. The framework of the linear roughness evolution implies the asymptotic behavior $h(q,t)^2 \sim \Gamma_1 q^{-1}$ and $h(q,t)^2 \sim \Gamma_4 q^{-4}$, respectively, for increasing t and with $\Gamma_n \equiv \Omega / \nu_n$. While the magnitude of the dispersion scales with B, the relative magnitude of Γ_1 and Γ_4 is determined exclusively by the parameters d and μ (Fig.3.1(a-b)).

From the hypothesis that increased subsurface free volume facilitates enhanced quasi non-local flow, hereby improving smoothing kinetics, the comparison of a-Si:H systems with intrinsic a-Si layers under ion bombardment is of great interest. Retention of hydrogen in a-Si layers is known to passivate lattice vacancies in the a-Si matrix, and for H contents of >14 at% to cause voids with a volume up to several cubic nanometers [12]. The hydrogen occupied vacancies and voids are considered to effectively represent free volume due to the relatively shallow binding and trapping potentials.

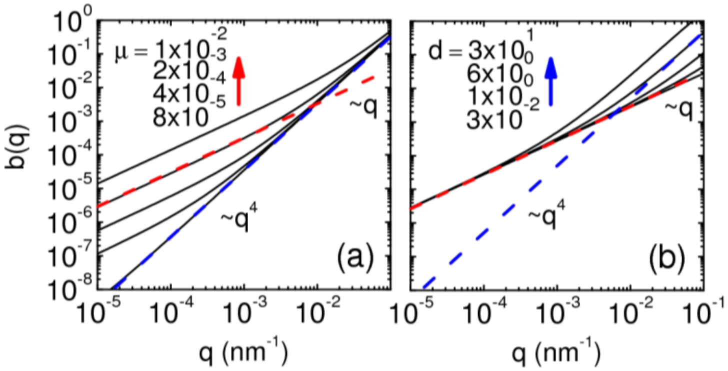

Fig.3.1 Dispersion in ion-induced kinetics. **(a)** Arrow indicates dependence in asymptote $\sim q$ on μ. **(b)** Dependence of $\sim q^4$ on d (nm).

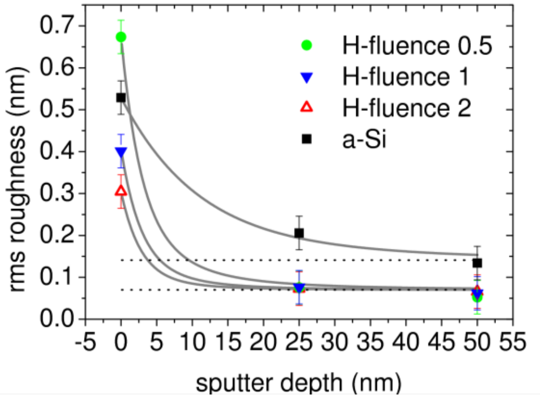

Fig.3.2 Measured evolution in rms roughness and explanatory fits to the data based on $n = 1$. Dashed lines indicate asymptotes in the fits.

H-fluence (arb.units)	0	0.5	1	2
ρ (gcm^{-3})	2.20	2.02	1.99	1.89
H (at.%)	0	27	29	32
$\sigma(25)$ (nm)	0.21	0.08	0.07	0.08
$\sigma(50)$ (nm)	0.13	0.06	0.07	0.05

TABLE 3.I Empirically determined layer parameters.

III. Experimental

a-Si:H Layers were produced by electron beam generated physical vapor deposition of 10 nm a-Si layers on polished Si wafer substrates, and post-deposition 400 eV H^+ exposure at fluences of 0.5, 1 and 2 (arb.units), making use of a Kaufmann ion source. The deposition was performed at high vacuum base pressure conditions (10^{-9} mbar) at room temperature. The penetration depth of the H^+ is in the order of 10 nm as calculated using the SRIM Monte Carlo code [13], ensuring a dilution of the a-Si matrix throughout the layer. To prevent interaction with the substrate, the first H^+ exposure was done after deposition of an additional 20 nm of a-Si. By performing the deposition and H^+ exposure cycle repetitively, layers of 20 nm a-Si+100 nm of a-Si:H were produced. Layers of 120nm deposited a-Si served as reference. The samples were subsequently sputtered with 100 eV Kr^+ at 45 ± 2 degree angle of incidence, by which an approximate layer thickness $t = 25$ nm and $t = 50$ nm was removed. For the applied Kr^+ beam parameters smooth physical vapor deposited a-Si layers are stable under sputtering [11].

In advance to Kr^+ sputtering the layer composition has been characterized by elastic recoil detection (ERD) and layer densities ρ were determined by analysis of the critical angle in hard x-ray Cu-K_α (0.154 nm) reflectance. Pre and post Kr^+ sputtering, the surface morphology was characterized by AFM at scan sizes of 1x1 μm and 10x10 μm.

IV. Results and Discussion

H content up to 32 at.% and a-Si:H layer densities reduced with 19% as compared to bulk Si density ($\rho_0 = 2.33$ gcm^{-3}) are observed (Table 3.I). *In-situ* reflectometry during sequential annealing cycles of 60 seconds and a temperature ramp of 100° C per cycle has revealed a densification of the a-Si:H starting at $T = 400°$ C (from $\rho = 1.89$ to 1.99 gcm^{-3}), whereas at $T = 700°$ C bulk density was obtained. Although not investigated in detail this indicates a trapping potential for a significant part of the hydrogen in the order of electronvolts.

The rms surface roughness σ before Kr^+ sputtering is observed to decreases with H^+ fluence (Fig.3.2). The decrements are considered to relate to interactions with residual amounts of Kr^+ as were present in the gas tubes during the H^+ exposure, which is in agreement with the detection of trace amounts of Kr in the ERD measurements. The varying roughness levels can be straightforwardly adapted as an initial constrained in further analysis. Furthermore $\sigma(t)$, with t the sputtered layer thickness, is found in general agreement with the roughness evolution, as given by equation (3.1) via the relation $\sigma(t) = \int h(q,t)^2 q dq$, for the various initial roughness values. No quantitative measure of the smoothing dispersion can be obtained from $\sigma(t)$ while lacking spectral information; flat PSD spectra were assumed with offset values to come to the different initial roughness levels. However, the data indicates a enhanced roughness relaxation and a reduced asymptotic roughness for all a-Si:H samples as compared to the intrinsic a-Si. To the awareness of the authors the observed ultra low rms surface roughness levels <0.1 nm, at the integrated spatial frequencies range $q/2\pi =$ 0.1-1×10^{-4} nm^{-1}, have not been reported previously for comparable layer systems.

To further quantify the dispersion in ion-induced kinetics the roughness evolution given by the solution of equation (3.1) has been fitted to the PSDs (Fig.3.2(a)), where v_n and Ω served as free fitting parameters and the measured PSD before Kr$^+$ exposure as a initial constrained. For all samples the dispersion is consistently characterized by $n=1$ for $q<q^*$ and $n=4$ for $q>q^*$, with the transition spatial frequency $q^*/2\pi =$ 6×10^{-2} nm^{-1} (a-Si) and 4×10^{-2} nm^{-1} (a-Si:H). The necessity of adopting $n=1$ in order to correctly fit the lower spatial frequencies is emphasized. Within the error bars obtained by simultaneous fitting of the PSDs at $t =$ 25 nm and $t =$ 50 nm (see Fig.3.3(a)) the linearity of the roughness evolution is rendered plausible [14], also considering the given experimental conditions and smooth surfaces. No other polynomial terms have been found to be of significant importance, although it is noted that around the transition frequency the dispersion shows a gradually changing slope corresponding to $1<n<4$. Fig.3.3(b) and Fig.3.3(c) show an example of the best model fit to the PSDs of the a-Si layer and the a-Si:H (H$^+$ fluence 0.5) layer at $t =$ 50 nm, whereas the results are compared by the projected model fit based on the best fitting parameters for the other layer. The enhanced smoothing at the a-Si:H is accompanied by significantly changed asymptotic behavior in the PSD, as indicated by the decrements in the ratio Γ_4/Γ_1 for all the Kr$^+$-sputtered a-Si:H as compared to the a-Si (Fig.3.4).

The differences in asymptotic behavior are explained from equation (3.3) by an increase in the quasi non-local flow fraction μ, but also by a decrease in the viscous layer thickness d. The latter is considered unlikely because of the extended projected Kr$^+$ trajectories into the layer at reduced densities would increase rather than decrease d. An explicit dependence in μ on the subsurface free volume, as derived from the layer density, is substituted in equation (3.3) in order to interpret the analytic predictions in terms of measured layer properties.

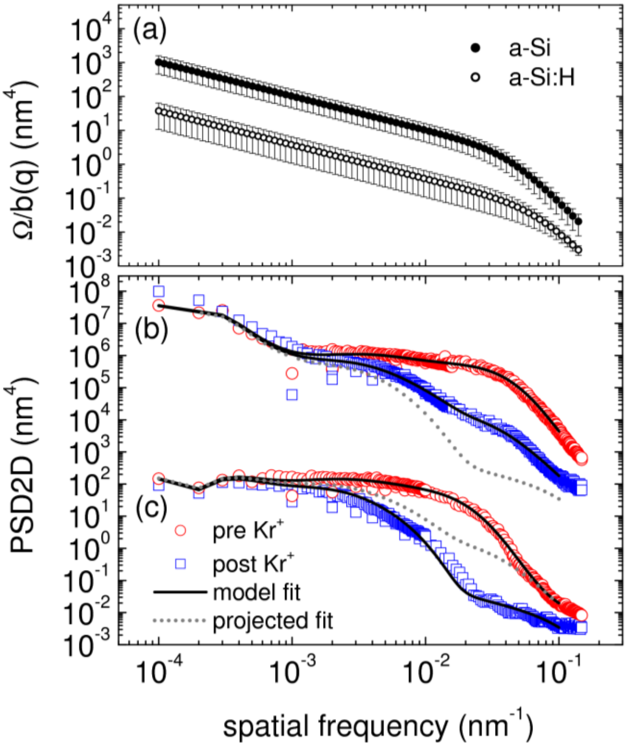

Fig.3.3 (a) Dispersions $\Omega/b(q)$ obtained by simultaneous fitting of the sets of PSDs for the a-Si and a-Si:H layers each. **(b)** PSD pre- and post 50 nm Kr$^+$ sputtering of a-Si (offset applied for imaging), and **(c)** a-Si:H. Solid lines represent best fits, dashed lines represent projected fits based on the best fit parameters of the other system.

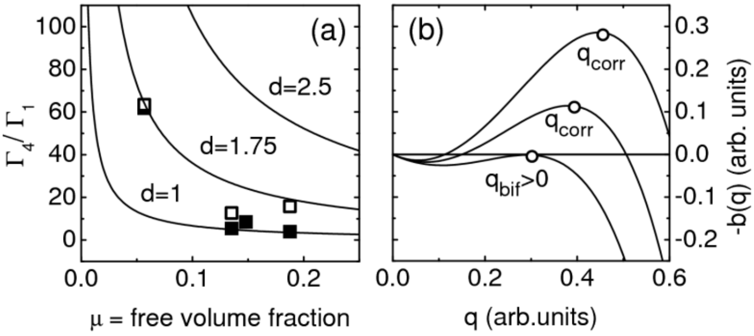

Fig.3.4 (a) Experimental data on Γ_4/Γ_1. 25 nm of Kr$^+$ sputtering (open), 50 nm of Kr$^+$ sputtering (solid). Lines represent analytic calculations. **(b)** Example of FVA model kinetics dispersion at different values of $v_2 < 0$.

In first approximation the upper limiting case of a one-to-one correlation is assumed $\mu(\rho) = \alpha(1 - \rho/\rho_0)$ with $\alpha = 1$. The data on Γ_4/Γ_1 is hereby reproduced for $d =$ 1 nm to 1.75 nm (Fig.3.4(a)). It is noted that a proportionality coefficient $\alpha < 1$ would yield a smaller value for d but a conclusive lower limit cannot be derived. Yet, a viscous layer thickness in the range $0 < d \leq 1.75$ nm is consistent with the depth at which the majority of the primary ion-atom collision events will take place, based on SRIM simulations and experiments on ion-induced intermixing in multilayer systems [15].

For noble ion beam parameters outside the layer smoothening regime, sputter-induced surface corrugations are reported in numerous studies. Corrugations are commonly accounted for by adopting a term $\nu_2 q^2$ with $\nu_2 < 0$ in the kinetics dispersion (equation (3.2)) [14,16]. The presence of a higher order term with a positive proportionality coefficient in the exponent $-b(q)$, which determines the growth-rate of surface Fourier components, results in a local maximum at $q \equiv q_{corr}$ driving spatial frequency selection in corrugation formation. The thus extended FVA model dispersion, characterized by $\propto q$, $\propto -q^2$, and $\propto q^4$, is compatible with the observations on ion-induced corrugations as reported in reference [10] (Fig.3.4(b)). Furthermore, the local maximum in $-b(q)$ is subject to a sign change for finite $q \equiv q_{bif}$ as a function of ν_2, where ν_2 is assumed an effective parameter depending on ion beam energy and angle of incidence [17]. Hereby the FVA model might offer a simple explanation of bifurcations between smooth- and corrugation dominated surfaces at non-diverging spatial frequencies [18,19], which is a still debated phenomenon. Whereas the bifurcations are reported to exist at dense matter surfaces (i.e. sputtered c-Si), this might imply FVA can occur as a sputter-intrinsic process, rather than to occur exclusively at deposited layers of reduced initial density. The authors are not aware of atomic scale experiments supporting this inference, but recognize an evolution in PSDs governed by $n = 1$ for low energy Ar^+-sputtered c-Si samples, as reported in reference [19].

V. Conclusions

It is demonstrated that retention of relatively large quantities of hydrogen into a-Si layers enhances the effect of low energy Kr^+ ion-induced smoothening, resulting in ultrasmooth surfaces (<0.1 nm rms). The special role of the hydrogen retention in a-Si layers is related to the occupied subsurface volume, facilitating enhanced quasi non-localized viscous flow as a steady state process during ion sputtering. The main features of the resulting surface morphology are quantitatively explained in terms of a linear evolution associated with viscous flow and subsurface free volume annihilation. Simulated ion target interactions show nanoscale depth ranges, in general agreement with the model parameters required to describe the data. Beyond the direct observations, bifurcations points between smooth and corrugation dominated surfaces at finite spatial frequencies are predicted, as is in agreement with elsewhere reported empirical data. This supports the notion that the theoretical framework is suited to describe the morphology of ion-sputtered surfaces for a wide range in ion beam parameters.

VI. Acknowledgements

We acknowledge financial support from the AgentschapNL through the EXEPT and ACHieVE programs coordinated by ASML and the Foundation for Fundamental Research on Matter (Stichting voor Fundamenteel Onderzoek der Materie, FOM) and Carl Zeiss SMT GmbH through the Industrial Partnership Program XMO.

VII. References

[1] J.G. Buijnsters, M.Camero, L. Vázquez, Phys. Rev. B **74** (2006) 155417.

[2] G.T. Dalakos, J.L.Plawsky, P.D. Persans, Appl. Phys. Lett. **85** (2004) 3462.

[3] F. Frost, B. Ziberi, A. Schindler, B. Rauschenbach, Appl. Phys. A **91** (2008) 551.

[4] M.S. Valipa, T. Bakos, E.S. Aydil, D. Maroudas, Phys. Rev. Lett. **95** (2005) 216102.

[5] W.M. Tong, R. S. Williams, Annu. Rev. Phys. Chem. **45** (1994) 401.

[6] C. Herring, J. Appl. Phys **21** (1950) 301.

[7] W. W. Mullins, J. Appl. Phys **30** (1959) 77.

[8] D. G. Stearns, Appl. Phys. Lett. **62** (1993) 1745.

[9] S. E. Orchard, Appl. Sci. Res. A **11** (1962) 451.

[10] C. C. Umbach, R. L. Headrick, K. -C. Chang, Phys. Rev. Lett. **87** (2001) 246104.

[11] A.J.R. van den Boogaard, E. Louis, E.Zoethout, S. Müllender, F. Bijkerk, J. Vac. Sci. Technol. A **28** (2010) 552.

[12] A.H.M. Smets, W.M.M. Kessels, M.C.M. van de Sanden, Appl. Phys. Lett. **82** (2003) 1547.

[13] J.F. Ziegler, J. P. Biersack, SRIM 2006.02 computer code, http://www.srim.org.

[14] C.S. Madi, E. Anzenberg, K.F. Ludwig, Jr., M.J. Aziz, Phys. Rev. Lett. **106** (2011) 066101.

[15] A.E. Yakshin, E. Louis, P.C. Görts, E.L.G. Maas, F. Bijkerk Physica B **283** (2000) 143.

[16] R.M. Bradley, J. M. E. Harper, J. Vac. Sci. Technol. A **6** (1988) 2390.

[17] S. Vauth, S. G. Mayr, Phys. Rev. B **75** (2007) 224107.

[18] C.S. Madi, B. Davidovitch, H. Bola George, S.A. Norris, M.P. Brenner, M.J. Aziz, Phys. Rev. Lett. **101** (2008) 246102.

[19] C.S. Madi, H. Bola Gearge, M.J. Aziz, J.Phys.: Condens. Matter **21** (2009) 224010.

Chapter 4

Influence of noble gas ion polishing species on Mo/Si multilayers

A.J.R. van den Boogaard, E. Zoethout, I. Makhotkin, E. Louis, F. Bijkerk

Various noble gases (Ne, Ar, Kr, Xe) have been applied for low energy ion-polishing of interfaces in nanoscale optical Mo/Si multilayers. The interface morphology was studied by grazing incidence small angle x-ray scattering (GISAX), the multilayer composition by x-ray photoelectron spectroscopy (XPS), and the general performance by extreme ultraviolet (EUV) reflectometry. Both the average roughness level and the vertical correlation length of the roughness are reduced significantly with increasing ion mass. Maximal EUV reflectance is observed for Kr^+-polishing, while Xe^+-polishing shows a superior structure. This apparent contradiction is explained by taking into account the absorption from noble gas residuals in the amorphous silicon (a-Si) layers.

I. Introduction

Noble gas ion bombardment of surfaces is one of the most versatile methods of controlling nanoscale surface morphology over large areas. For several amorphous layer systems and noble gas ion species an angular window close to 45 degree incidence of the ion beam enables layer polishing. Such treatment is widely employed to produce ultrasmooth surfaces in (photo)electric and micro-mechanical devices and x-ray optics. The process of layer smoothing is a direct consequence of the collision cascade caused by an ion impact at the target layer material. Local bond breaking allows atomic redistribution driven by e.g. minimization of surface free energy. For lateral roughness scales >10 nm the ultimate layer smoothness is reported to be not critically dependent on the ion energy in several studies [1-4], which is also in agreement with the findings presented in chapter 2. Moreover, in thin film and multilayer applications the ion energy is practically limited by the stopping power to prevent layer intermixing [5]. The absence of an apparent dependence in surface smoothing kinetics on ion energy indicates that the number of atomic displacements in a near surface volume per sputtered atom is not affected strongly, and a surplus of ion energy dissipates into the bulk [3]. Yet, an increase of the number of near surface atomic displacements and, more specifically, the balance between the resulting kinetics and sputter induced stochastical roughening could enhance the ion sputtering surface smoothing process.

Despite utmost efforts to obtain ion-enhanced deposition conditions facilitating growth of the smoothest amorphous layers, a systematic study of the role of the noble gas ion-polishing species is lacking to date. The ion species is considered a parameter of particular interest since the primary ballistics, as determinative for the subsequent collision cascade, will depend on the mass and size of the colliding species with the target layer. This chapter reports on a comparison between the smoothing effects of various noble gas ion species (Ne^+, Ar^+, Kr^+, Xe^+) on the a-Si surface morphology in Mo/Si multilayers for near normal incidence extreme ultraviolet (EUV) reflectance. The interface roughness of the repeating bilayers has been studied by grazing incidence small angle x-ray scattering (GISAXS). It is emphasized that the analysis of multilayers enables probing aspects of the ion-induced roughness evolution which are not accessible by the study of equivalent single-layer systems, e.g. roughness replication between interfaces, and as such the results are of interest beyond the direct application of EUV optics as well. Additionally the multilayers have been analyzed on composition by x-ray photoelectron spectroscopy (XPS), and near-normal EUV specular reflectance.

II. Experiments

II.1. Multilayer deposition

Mo/Si multilayers with 50 bilayers of 6.95 nm thickness and a Mo to (Mo+Si) thickness ratio of 0.4 have been deposited on commercially available polished Si wafers. Physical vapor deposition at room temperature and high vacuum conditions with a base pressure of 10^{-9} mbar was employed. The deposition conditions and multilayer composition result in amorphous Si and nanocrystaline Mo layers [6]. Layer thickness control was obtained by using an *in situ* reflectometer operating at the C K_{α} x-ray band. The experimental setup is thoroughly described in reference [7]. Surface smoothening was obtained by a noble gas ion-polishing treatment after deposition of each Si layer. A Kaufman ion source, mounted under 45° with respect to the substrate holder, was used to generate the ion beam. Different multilayers have been deposited while using the ion-polishing species Ne^+, Ar^+, Kr^+, and Xe^+ at a fixed energy of 130 eV, obtaining species and flux dependent sputter rates in the order of 0.5 nm/min. For consistency, the duration of the ion-polishing treatment was varied in order to obtain a sputtered Si layer thickness of 0.5 nm at each bilayer for all polishing gases. For the described experimental conditions and substrates, the ion-polishing treatment is considered saturated, yielding a steady-state interface roughness near the asymptotic lower limit given by the layer growth and ion-polishing kinetics, and therefore ion-fluence optimization is omitted.

II.2. Analysis

II.2.a GISAXS measurements

Measurements on hard x-ray scattering in the non-coplanar geometry were performed at the various multilayers, at a wavelength of 0.138 nm and a grazing angle of incidence of 0.7 deg. As is further addressed in section 4.III.1, hereby a large portion of the total multilayer stack is probed. Per convention $\vec{z}$ indicates the surface normal of the multilayer plane in (x, y). While reflection at a perfectly smooth surface can only give rise to momentum transfer to the incoming photon in $\vec{z}$, isotropic surface roughness of spatial frequency $f_{||}$ can result in scatter related to lateral momentum transfer $q_{||}{}^2 = q_x{}^2 + q_y{}^2$, with $f_{||} = q_{||} / 2\pi$. The scattered x-rays were recorded by a two-dimensional CCD camera, with the plane of detection aligned with (y, z), while the specular reflected beam was blocked. Note that each transfer in momentum into (q_y, q_z) is accompanied with a (relatively small) momentum transfer in q_x, which can be obtained for the GISAXS geometry as described in more detail in references [8,9].

II.2.b EUV reflectometry and XPS

Specular near-normal incidence reflection measurements in the wavelength range 12.5 nm to 14 nm have been performed at the EUV beam line of the Physikalisch Technische Bundesanstalt (PTB) at the BESSY electron storage ring in Berlin, giving a direct measure of the overall quality of the Mo/Si multilayers. To be able to differentiate between the influence of multilayer interface structure and layer composition as obtained by the various ion-polishing species, the composition of the multilayer was characterized by XPS depth profiling. Depth profiles were obtained by XPS measurements during sputtering of the multilayers with 500 eV Ar^+, with the exception for the Ar^+-polished multilayer were 500 eV Kr^+ was used.

III. Results and Discussion

III.1. GISAXS

CCD camera images of the scattered x-ray intensity are depicted in Fig.4.1 as a function of the momentum transfer in (q_y, q_z). The integrated intensity over the displayed range decreases with ion mass (Table 4.I), indicating enhanced interface smoothness for the polishing treatment with the more massive ion species. The data is modulated as a function of q_z by the periodic multilayer structure in f_z, resulting in so called Bragg-sheets occurring when the Bragg-condition for constructive interference in the outgoing beam is satisfied. In Fig.4.1 cross-sections of the Bragg-sheets are visible as the local maxima along the q_z axis. Further analysis is focused on the second ($p2$) and the third ($p3$) Bragg-sheets, since the first sheet is located too close to the (blocked) specular reflected beam for proper interpretation while higher order sheets lack signal/noise ratio for the smoothest samples. The average momentum transfer is -0.016 nm^{-1} ($p2$) and -0.05 nm^{-1} ($p3$) in q_x, and 1.88 nm^{-1} ($p2$) and 2.8 nm^{-1} ($p3$) in q_z. The full width at half maximum of the Bragg-sheets in q_z (i.e. $FWHMq_z$) has been determined as a function of q_y from Gaussian fits to $p2$ and $p3$. In the obtained curves a clear dependence on both q_y and ion species is observed (Fig.4.2), where at higher ion masses the increments in $FWHMq_z$ as a function of q_y are most prominent.

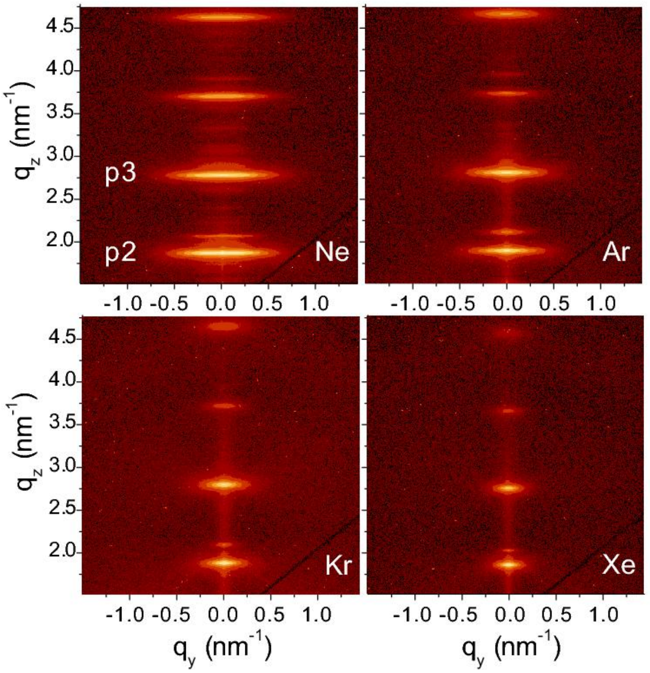

Fig.4.1 CCD images on multilayer x-ray scatter in momentum transfer space, for the several polishing ion species. The intensity scale is logarithmic and the bright regions indicate high intensity.

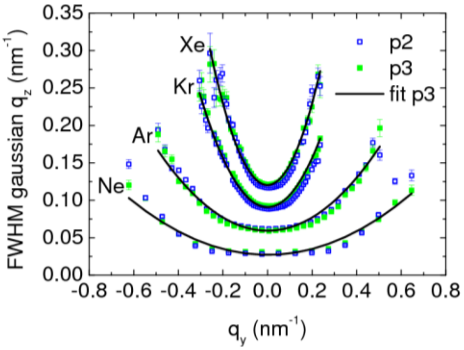

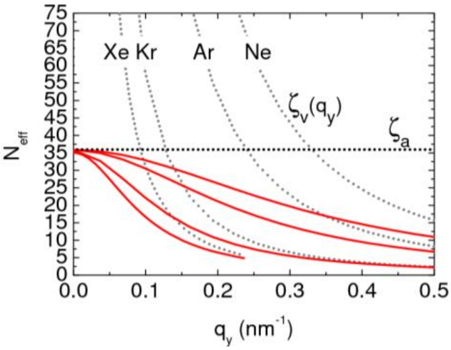

Fig.4.2 Fits and plots of $FWHMq_z$ extracted from the scatter data. A fixed vertical offset between the curves is applied for imaging purposes; the minima at $q_y = 0$ coincide.

Fig.4.3 N_{eff} as obtained from the fitting of $FWHMq_z$ (solid lines). The dashed lines indicate the dependence on the optical penetration depth (ξ_a = 125 nm) and structural relaxation.

The cross-correlation function is defined on the spatial frequency domain as the dot product between two interface profile functions h: $C(\tau) = \langle h_n(f_{\text{II}}) h_m(f_{\text{II}}) \rangle$, with τ the vertical spatial separation between interface n and m. The $FWHMq_z$ is inversely proportional to the effective number of bilayers N_{eff}, with thickness d, which coherently contribute to the scatter. Via the relation $N_{eff} = \xi_v / d$ the vertical correlation length $\tau \equiv \xi_v$ can be obtained over which, per convention, the profile cross-correlation function between the interfaces decays exponentially. Analysis of $FWHMq_z$ allows interpretation of the data in terms of the evolution of roughness throughout the multilayer stack accordingly.

The dependence of $FWHMq_z$ on q_y (Fig.4.2) shows that the multilayer structure is characterized by a vertical correlation length which is a function of the spatial frequency of the interface roughness, i.e. $\xi_v(f_{\text{II}})$. This evidently should be addressed in a model description of the roughness evolution, and discards the simplest models employing a uniform vertical correlation length over the entire spatial frequency spectrum. In the linear model proposed by E. Spiller, D. Stearns, and M. Krumrey, which is considered applicable due to the low roughness levels and amorphous layer structure, the spatial frequency dependence naturally arises from the analysis of the continuum layer growth kinetics [10]. Hereby the cross-correlation function is described to decay exponentially over an effective number of bilayers N_{eff}, as being inversely proportional to the ion-sputtered thickness at each Si layer t_{sput}. The dependency on t_{sput} arises since roughness relaxation, hence decoupling of the interface profiles, is driven by the ion-polishing and scales with the sputtered layer thickness. Multiplication with the bilayer thickness d gives the vertical correlation length:

$$\xi_v(k_{\text{II}}) = d / (t_{sput} \times b(f_{\text{II}})), \tag{4.1}$$

and $$b(k_{\text{II}}) = \sum_i v_i (2\pi f_{\text{II}})^i . \tag{4.2}$$

The orders of the polynomial equation (4.2) correspond to the kinetics involved with proportionality coefficients v_i, which determine the damping rate of surface profile Fourier components. Spiller *et al.* propose a roughness evolution governed by Edwards-Wilkinson relaxation, relating to $i = 2$ [11]. Other processes which might be of relevance are ion-induced viscous deformations and sub-surface free volume annihilation ($i=1$) [4], or strictly surface confined viscous flow ($i=4$) [12]. Equation (4.1) has been fitted to the data using a least-square fitting routine (Fig.4.2), and it is found that no polynomial of order $i \geq 1$ can give a satisfactory description of $FWHMq_z$ for the full range in $f_{||}$ as probed; equation (4.2) inevitably approaches zero in the limit for small $f_{||}$, resulting in $\xi_v(f_{||}) \to \infty$ and $FWHMq_z \downarrow 0$. Physically this relates to the very slow relaxation of low spatial frequency roughness throughout the multilayer stack. At $f_{||}=0$ the interfaces are perfectly planar and unaffected by relaxation, yielding an infinite vertical correlation length. The observation of a finite, non-zero, minima in Fig.4.2 results from the fact that for small $f_{||}$ the vertical correlation length exceeds the exponential decay length of the field intensity in the multilayer, defined as ξ_a measured into $\vec{z}$. The latter measure is determined by the interface transmission coefficients and absorption, and will be referred to as optical penetration depth. Here is proposed to take ξ_a into account by a 0th-order term in equation (4.2), i.e. $i=0$, and $v_0 = d/(2\xi_a \times t_{sput})$. It is found that this approach produces accurate fits to the data at $p2$ and $p3$ for the entire range of lateral momentum transfer, and is therefore preferred above the exclusion of data of small $f_{||}$ from the analysis. Fig.4.3 illustrates how N_{eff} for the several ion species is governed by optical penetration depth and structural evolution at the lower and higher values of momentum transfer, respectively (dashed lines). The fitting parameters are summarized in Table 4.I.

Ion species	Ne^+	Ar^+	Kr^+	Xe^+
Int.scatter (arb.units)	3.23	1.66	1.54	0.89
v_2 [nm]	0.47 ± 0.04	0.98 ± 0.04	3.5 ± 0.08	6.2 ± 0.15
ξ_a [nm]	125 ± 8	115 ± 4	119 ± 3	130 ± 4
Residuals At.%	0.8 ± 0.5	1 ± 0.7	0.6 ± 0.5	0.6 ± 0.5

TABLE 4.I Integrated scatter, fitting parameters (average value of fits to $p2$ and $p3$), and residual noble gas concentrations, for different ion species.

The experimental values $FWHMq_z$ for all noble gases are explained consistently by the optical penetration depth and Edwards-Wilkinson layer growth. It should be taken into account that the spatial frequency range of highest structural sensitivity is limited to $1.5\times10^{-2} > f_{II} > 6\times10^{-2}$ nm^{-1}, and kinetics other than Edwards-Wilkinson growth might be of relevance outside this range. The roughness relaxation coefficient ν_2 is observed to scale with ion mass, which is in agreement with the opposite tendency as observed in the total integrated scatter. The mass dependence in the latter measure is less critical than the trend in ν_2 suggests, which points at higher levels of non-correlated stochastical roughness, i.e. “shot-noise”, for more massive ions. Still the overall enhancement of the layer smoothening kinetics for the more massive polishing ions is unambiguous. In general terms, this can relate to ion/target-atom mass ratio’s M_{ion}/M_{Si}, i.e. 0.72 to 4.67 for Ne^+, Ar^+, Kr^+, and Xe^+, and the size of the ions. The tabulated stopping power in a-Si increases with ion mass [13], and the efficiency of energy transfer decreases for mass ratio deviations from unity. It is considered plausible that hence a higher energy density and more ion-induced displacements per atom in a near surface treatment volume are obtained by employing ions of increased mass for polishing. The hereby decreased viscosity is determinative for the extent to which surface currents reducing layer height perturbations can occur, and which are held responsible for Edwards-Wilkinson layer growth [14]. The fitting parameter ξ_a slightly underestimates the value obtained based on the tabulated optical constants, which is approximately 160 nm. Possibly this is caused by the inherently finite number of bilayers which can contribute to the scatter, i.e. 50 bilayers in presented experiments. This may translate in a value ξ_a which is smaller than the actual optical penetration depth, and which should be considered an effective measure of both field intensity decay and the limited number of bilayers.

III.2. XPS

In-depth composition profiles for the multilayers are obtained from the integrated elemental peaks in the XPS depth profile spectra. The data are normalized on the elemental sensitivity in order to extract in-depth composition profiles. An example of a depth profile for the Xe^+-polished multilayer is shown in Fig.4.4. Besides the layered Mo/Si structure and native Si oxide originating from the ambient exposed multilayer surface, a residual amount of polishing gas is found to be present in the a-Si layers (Table 4.I). Residual concentrations of noble gas in a-Si up to several atomic percent are reported in literature for simultaneous layer growth and low energy ion assistance, whereas burying of the noble gas atoms during the deposition procedure is considered to be one of the dominating mechanisms of incorporation [15,16]. In the presented data relatively low concentrations of residual noble gas are observed (<1 at.%). This is explained by the deposition conditions, where the ion exposure was performed only after the a-Si layer growth. This excludes that gas gets incorporated by trapping of polishing ions below the progressing growth front.

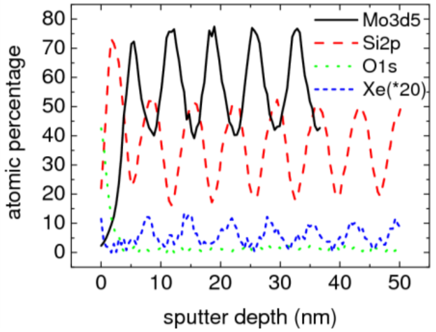

Fig.4.4 XPS depth profile of Xe+-polished Mo/Si multilayer. The Xe concentration profile is multiplied by a factor 20 for clarity.

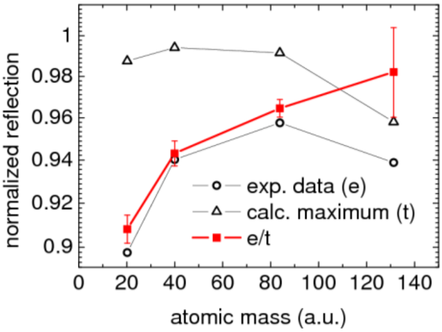

Fig.4.5 Experimental and calculated data on EUV reflectance vs. atomic mass of the polishing ion. Lines serve to guide the eye. The error bars arise from the uncertainties in noble gas residuals.

III.3 EUV reflection

The multilayers were characterized by near-normal incidence specular reflection in the EUV wavelength range from 12.5 to 14 nm. The peak reflectance values at 13.5 nm are plotted in Fig.4.5. The data reveals the preferential use of Kr over Xe as a polishing gas, contradicting the expectations merely based on the multilayer structure as probed by GISAXS. This indicates that the polishing gas residuals affect the optical characteristics of the Si layers. The effective optical constants therefore have been calculated from the atomic scattering factors as obtained from reference [17]. The residual polishing gas atoms were assumed to replace Si atoms in the amorphous matrix. Subsequently, the influence on peak reflectance was examined by employing Fresnel calculations using the IMD computer code [18] and a $Mo/Si_{1-c}X_c$ multilayer model with X_c referring to the residual noble gas species at atomic concentration (c) as given by Table 4.I. The multilayer structures have been taken ideal, i.e. without interface roughness, the bilayers thickness was 6.95 and at each interface 0.8 nm of $MoSi_2$ was assumed as inline with reference [5]. The thickness fraction of the Mo as compared to multilayer period was 0.4. The accordingly modeled peak reflectance shows to be mainly influenced by incorporation of Xe; significant decrements are observed relative to the ideal multilayer containing pure Si (72.9% peak reflectance) on which all data in Fig.4.5 is normalized. When is compensated for this effect by taking the ratio of the experimental reflection data and the calculated maximum values, a monotonically increasing peak reflectance with atomic mass of the ion-polishing species is observed indicating that the ideal multilayer structure (Fig.4.5), reflectance = 1) is closer approached. The remaining losses can be attributed to interface roughness. The trend is in qualitative agreement with the data presented in section 4.III.1 and cross-verifies the notion that the use of more massive polishing ions results in enhanced interface quality.

IV. Conclusions

It has been shown that the interface morphology in Mo/Si multilayers strongly depends on the noble gas ion species (Ne^+, Ar^+, Kr^+, Xe^+) employed for ion-polishing of the a-Si layers, where the smoothening increases with ion mass and is optimal for Xe^+. A model fit was found in excellent agreement with the experimental widths of the Bragg-sheets in hard x-ray scatter measurements, where the only two free parameters are the optical penetration depth and the spatial frequency dependent vertical correlation length. The latter is governed by Edwards-Wilkinson roughness relaxation at the spatial frequency range as probed $1.5\times10^{-2} > f_{\text{II}} > 6\times10^{-2}$ nm^{-1}. The superior relaxation for the more massive polishing ions is considered to relate to a preferential enhancement of the near surface collision cascade. Optimized EUV peak reflectance is observed for Kr^+-polishing, despite Xe^+ is favored from a structural point of view, as is explained by the optical properties of the residuals of noble gas in the a-Si. The data shows that multilayer reflectance values in the EUV wavelength range can be significantly improved with up to several percent (depending on noble polishing gas species) if the residual gas amounts could be removed, or deposition conditions yielding less gas incorporation could be applied. Whether this is possible within the rather small experimental parameter space enabling EUV multilayer deposition is a topic for further study. If minimization of diffuse scatter from multilayers is aimed for rather than optical throughput, Xe^+-enhanced a-Si growth conditions can straightforwardly be applied and are considered very promising.

V. Acknowledgements

We acknowledge financial support from the AgentschapNL through the EXEPT and ACHieVE programs coordinated by ASML and the Foundation for Fundamental Research on Matter (Stichting voor Fundamenteel Onderzoek der Materie, FOM) and Carl Zeiss SMT GmbH through the Industrial Partnership Programme XMO. Furthermore the authors wish to thank P. Siffalovic at the Institute of Physics, Slovak Academy of Sciences, for the GISAXS measurements.

VI. References

[1] J.G. Buijnsters, M.Camero, and L. Vázquez, Phys. Rev. B **74** (2006).

[2] F. Frost, B. Ziberi, A. Schindler, and B. Rauschenbach, Appl. Phys. A **91** (2008).

[3] F. Ericson, N Ghafoor, F. Schäfers, E.M. Gullikson, and J. Birch, Thin Solid Films **500** (2006).

[4] I.Nedelcu, R.W.E. van de Kruijs, A.E. Yakshin, F. Tichelaar, E. Zoethout, E. Louis, H. Enkisch, S. Muellender, and F. Bijkerk, Thin Solid Films **515** (2006).

[5] A.E. Yakshin, E. Louis, P.C. Görts, E.L.G. Maas, and F. Bijkerk, Physica B **283** (2000).

[6] R.W.E. van de Kruijs, E. Zoethout, A.E. Yakshin, I. Nedelcu, E. Louis, H. Enkisch, G. Sipos, S. Müllender, and Fred Bijkerk, Thin Solid Films **515** (2006).

[7] E. Louis, A. Yakshin, T. Tsarfati, and Fr. Bijkerk, Prog. Surf. Sci, (2011), doi:10.1016/j.progsurf.2011.08.001

[8] P. Siffalovic, E. Majkova, L. Chitu, M. Jergel, S. Luby, J. Keckes, G. Maier, A. Timmann, S.V. Roth, T. Tsuru, T. Harada, M. Yamamoto, and U. Heinzmann, Vacuum **84** (2009).

[9] P. Siffalovic, et al., GISAXS - Probe of Buried Interfaces in Multilayered Thin Films chapter in the book X-Ray Scattering, ed. Christopher M. Bauwens, NOVA Publishers, 2011, New York, ISBN: 978-1-61324-326-8

[10] E. Spiller, D. Stearns, and M. Krumrey, J. Appl. Phys. **74** (1993).

[11] S.F. Edwards and D.R. Wilkinson, Proc. R. Soc. London A **381**, 17-31 (1982).

[12] C.C. Umbach, R.L. Headrikc, and K.-C. Chang, Phys. Rev. Lett. **87**, 246104 (2001).

[13] J. F. Ziegler and J. P. Biersack, SRIM 2006.02 computer code, http://www.srim.org.

[14] M. Moseler, P. Gumbsch, C. Casiraghi, A.C. Ferrari, and J. Robertson, Science **309** (2005).

[15] P.F. Barbieri, M.H. de Oliveira Jr., A. Champi, and F.C. Marques, J. Non-Cryst. Solids **352** (2006).

[16] V. Rigato, A. Patelli, G. Maggioni, G. Salmaso, V. Mattarello, M.g. Pelizzo, P. Nicolosi, L. Depero, E. Bontempi, and P. Mazzoldi, Surf. Coat. Tech. **174-175** (2003).

[17] B.L. Henke, E.M. Gullikson, and J.C. Davis, Atomic Data and Nuclear Data Tables **54** (1993).

[18] D.L. Windt, Comput. Phys. **12**, 4 (1998).

Chapter 5

Optical element for full spectral purity from IR-generated EUV light sources

A.J.R. van den Boogaard, E. Louis, F.A. van Goor, F. Bijkerk

Laser produced plasma (LLP) sources are generally considered attractive for high power EUV production in next generation lithography equipment. Such plasmas are most efficiently excited by the relatively long, infrared wavelengths of CO_2-lasers, but a significant part of the CO_2 radiation will be back-scattered by the plasma's critical density surface and consequently will be present as undesired radiation in the spectrum of such sources. Since most optical elements in the EUV collecting and imaging train have a high reflection coefficient for IR radiation, undesirable heating phenomena at the resist level are likely to occur. In this study a new principle is employed to obtain full separation of EUV and IR radiation from the source by a single optical component. While the application of a transmission filter would come at the expense of EUV throughput, this technique potentially enables wavelength separation without loosing reflectance compared to a conventional Mo/Si multilayer coated element. As a result this method provides full spectral purity from the source without losses in EUV throughput. Rigorous calculations on the principal of functioning are presented.

I. Introduction

Extreme ultraviolet Lithography (EUVL) is a main candidate for production of next generation integrated circuits (ICs), and its potential has been further established since the first proof of principle wafer steppers, so called Alpha Demo Tools, successfully demonstrated printing of 32 nm structures [1]. EUVL is aimed to enable high volume IC manufacturing, requiring that the exposure time per treated wafer is minimized. The yield expressed in wafers per hour is generally determined by the EUV intensity offered at the photoresist, and is primarily depending on source intensity and throughput of the optical system. Several source suppliers worldwide are spending great efforts to enhance the efficiency of the EUV sources towards the industrial needs of approximately 200 W of narrow band EUV yield. Laser produced Sn plasma sources in which a droplet of tin is irradiated with a powerful drivelaser to excite an EUV emitting plasma are considered attractive. As a drivelaser, especially 10.6 μm emitting CO_2-lasers may have high yield possibilities. Due to the effective backscattering of the 10.6 μm infrared radiation at the surface of critical density of the Sn plasma however, besides EUV a high load of infrared will be present in the LPP source spectrum.

High throughput of the optical system for EUV is achieved by using Mo/Si based multilayer coated elements, for which near-normal incidence reflectance values just over 70% have been reported [2]. However, EUV optimized multilayer coatings efficiently reflect radiation from vacuum ultraviolet (VUV, $\lambda = 100$-400 nm) to infrared as well (Fig.5.1). As a consequence, the convolution of the source spectrum and response of the optical elements in a EUVL tool will result in a large spectral range of radiation reaching the photoresist, degrading the EUV projected image quality and causing undesired heating. The successful suppression of out-of-band radiation in the VUV range, by application of a spectral purity layer on top of a Mo/Si multilayer stack has been reported [3,4], but for 10.6 μm radiation this is not feasible due to the large wavelength and low absorption relative to EUV, which would lead to unacceptable losses in this wavelengthrange. The application of transmission IR filters has also been suggested, requiring delicate handling due to the extreme fragileness when sufficiently thin to maintain the throughput in EUV.

In this chapter, a hybrid multilayer-grating optical element is proposed as a spectral purity enhancing device. Rigorous calculations are presented, showing that in terms of EUV throughput this approach compares very favorable against transmission spectral filtering. As a further advantage, mechanical robustness and the specifications on heat load resistivity are equivalent to conventional multilayer optics.

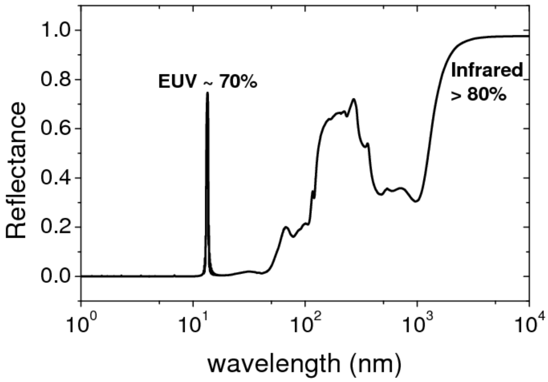

Fig.5.1 Calculated [5] reflectance of a 50 bilayers Mo/Si multilayer coating of 6.9 nm periodicity and a Mo ratio of 0.4.

II. Spectral purity grating design

The use of a blazed reflection grating, to be employed to shift reflected energy out of the mode of specular reflection with respect to the grating plane, is suggested. The angular position of the orders in reflection arising is given by the grating equation, here recalling the definition as provided in chapter 1:

$$\Lambda(\sin(\theta_m)-\sin(\theta_i))=\lambda m, \qquad (5.1)$$

in which Λ is grating pitch, θ_m is the normal angle of diffraction of order m, θ_i is the normal angle of incidence and λ is the wavelength of the radiation. The dependence of θ_m on λ for $m \neq 0$ directly reveals the possibility of spectral separation of different wavelengths over an angular range, at fixed angle of incidence: $\theta_m(\lambda_1)-\theta_m(\lambda_2)$. In order to operate at EUV wavelengths the optical surface of the grating should be equipped with a Mo/Si multilayer. The very large wavelength difference between EUV and IR conveniently allows angular spectral separation by such an optical element, in particular when the grating design is chosen such that the high efficiency orders for the IR radiation are well separated from the optical path followed by the EUV.

Unlike the angular position of the orders in diffraction, which solely dependents on the pitch and the wavelength as is shown by equation (5.1), the efficiency of the orders is a function the grating profile. In order to give optimal EUV throughput, approaching a flat mirror, the multilayer structure should be locally planer. The grating, which functions as a substrate for the Mo/Si multilayer, should thus have flat facets. A blazed grating with a saw-tooth profile is therefore considered a viable candidate (Fig.5.2). In another application the use of Mo/Si multilayers on blazed gratings has been reported with efficiencies up to 63 % of the total diffracted and scattered energy in a single order [6]. The latter would correspond to an absoluter EUV reflectance of about 44%, assuming a multilayer reflectance of 70%.

The novel approach presented here is based on choosing the grating pitch to be comparable to, or larger than, the wavelength of the IR, in combination with a Mo/Si multilayer coating optimized for near-normal reflectance. It has been verified by rigorous calculations performed with the software package PCGrate-SX6.1, that unperturbed flat mirror EUV reflectance can be approached for the proposed multilayer-grating system in the case of large grating facets, provided that multilayer shows no significant structural deformations from when deposited on the blazed grating. The main part of the power in EUV will be reflected under angles close to the blaze angle while the IR is diffracted over sufficiently large angles to enable spatial separation from the optical path of the EUV.

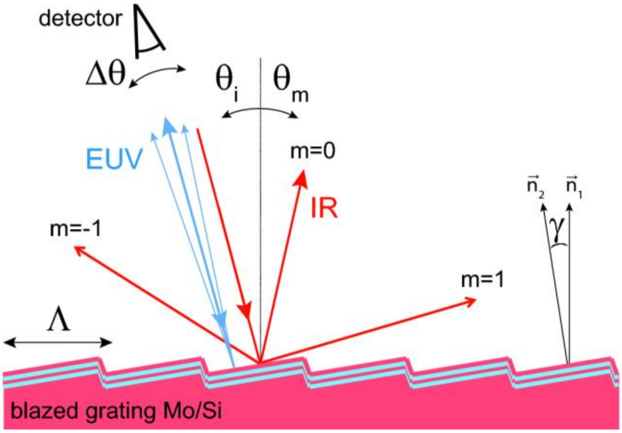

Fig.5.2 Schematic optical response of a Mo/Si multilayer coated blazed grating and the possible geometry for spectral purity enhancement purposes.

In the calculations, the blaze angle is treated as a fixed parameter; in this example γ = 21 deg. On the blazed grating 50 bilayers Mo/Si of 6.9 nm thickness, optimized for reflectance at 13.5 nm and 1.5 deg normal angle of incidence, are applied. It should be noticed that the angle of incidence with respect to the normal of the grating plane ($\vec{n}_1$) is 22.5 deg, while specular reflection of the EUV in the multilayer plane ($\vec{n}_2$) yields an angle of -19.5 deg. When both the incident radiation as the diffracted orders are on the same site of the grating plane normal, this results in a negative sign in the diffraction angle.

The detector aperture defining the angular acceptance for the combined diverging beam, consisting of different orders in diffraction, is chosen to be $\Delta\theta$=3 deg. For various grating pitch dimensions ($\Lambda = 100$ nm, 333 nm, and 1000 nm) the efficiency, the angle of diffraction and the convolution with the detector aperture are calculated as a function of wavelength in the EUV range for several orders. Results are depicted in Fig.5.3.

Fig.5.3(a) reveals that only one order of diffraction ($m = $-5) contributes to the reflected energy within the acceptance angle for Λ= 100 nm. For the larger grating pitches, Λ= 333 nm Fig.5.3(b), and Λ= 1000 nm Fig.5.3(c), besides the four orders taken into account, several more contribute to the reflectance. Since efficiencies are low however, they were left out of analysis. It is observed that for increasing grating pitch, up to Λ = 1000 nm (Fig.5.3(c)), the response of the Mo/Si multilayer coated blazed grating rapidly approaches flat Mo/Si mirror reflectance (as equal to the total reflected energy). Due to limited computer time the rigorous calculation have not been extended to even larger pitches, yet extrapolating the results, it is expected that for grating pitches of 50 to 100 μm the measured reflectance will be practically indistinguishable from the total reflectance. This would result in a Mo/Si multilayer coated blazed grating with a potential reflectance above 70% at 13.5 nm. Furthermore, performance limitations as caused by near step-edge deformations in the multilayer structure, which in practice inevitably will arise in the multilayer deposition process, can be diminished at larger pitches. The upper limitation to the grating pitch is given by the ability to still diffract the undesired radiation over sufficiently larger angles. A grating pitches up to Λ= 1000 nm which are relatively small as compared to the wavelength of the 10.6 μm IR, the only possible order in IR reflection will be $m = 0$ at 21 deg (which can be seen as a case of specular reflection with respect to the grating plane). This obviously yields a full separation of EUV and IR in the order over tens of degrees. Equation (5.1) has been employed to calculate the inter-order separation in IR at elongated pitches up to 100 μm (Fig.5.4). At a pitch of 100 μm the separation between the IR orders of diffraction is larger than 6 deg, giving a ±3 deg angular separation from the optical path followed by the EUV. The authors consider this well within the requirements for a real spectral purity enhancement application.

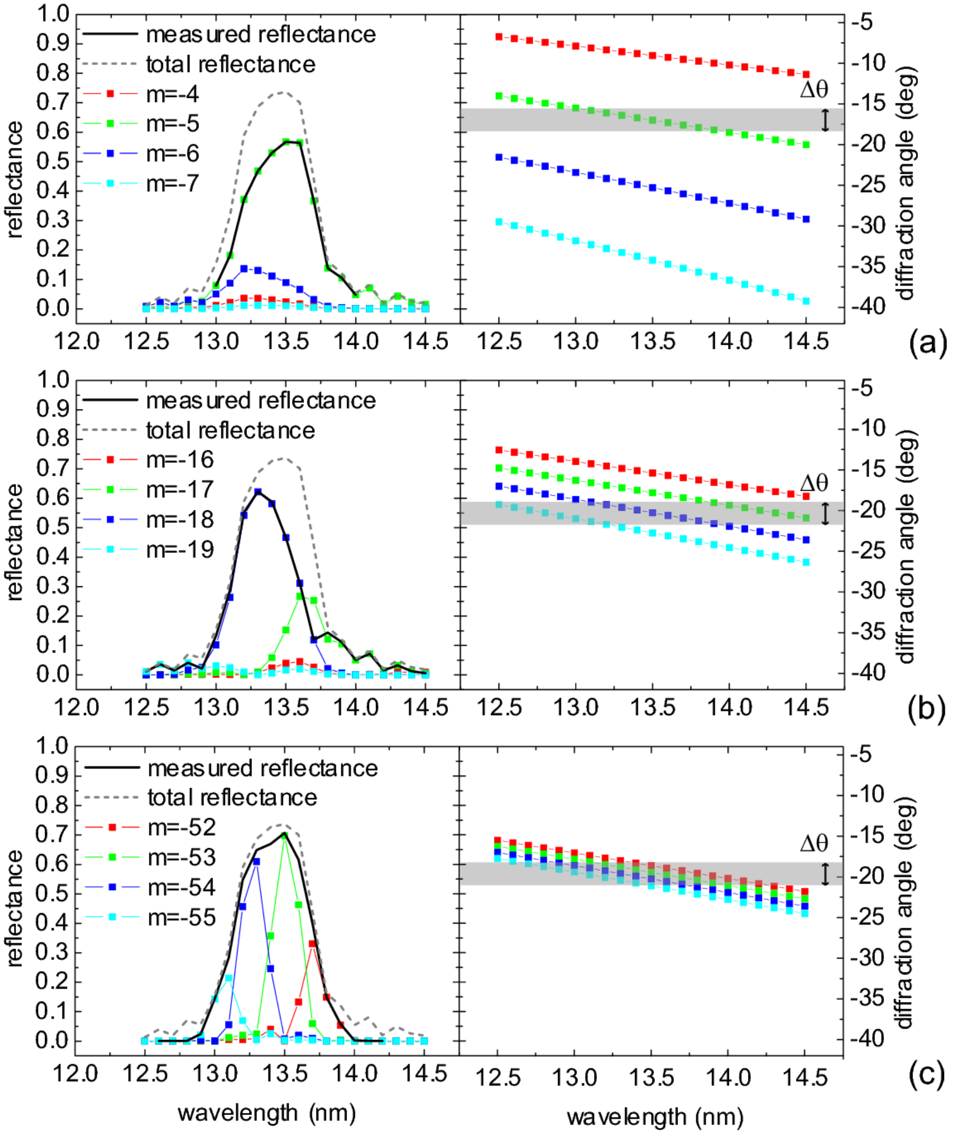

Fig.5.3 The reflectance as a function of wavelength and the diffraction angle for the different orders, plotted for several values of grating pitch. The four orders of highest efficiency at 13.5 nm are considered. The detector aperture $\Delta\theta$ is indicated in grey and centered around the order of highest efficiency. **(a)** $\Lambda = 100$ nm **(b)** $\Lambda = 333$ nm **(c)** $\Lambda = 1000$ nm.

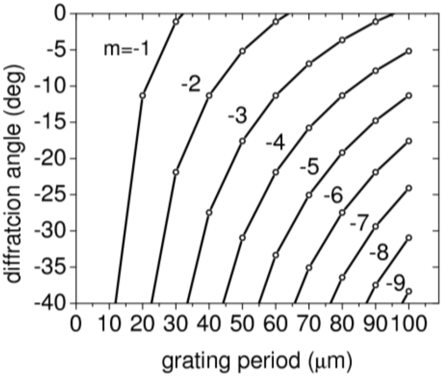

Fig.5.4 Diffraction angle for 10.6 μm IR as a function of grating pitch up to 100 μm.

III. Summary and Outlook

This study shows the potential of achieving full spectral separation of EUV and IR by application of a Mo/Si multilayer coated blazed grating. Based on rigorous calculations it is expected that for multilayer deposition friendly grating pitches (50 μm and upwards) the response of the proposed system equals an unperturbed Mo/Si multilayer EUV reflectance, while the diffracted orders in the IR angularly deviate sufficiently to be spatially fully isolated from the EUV. This enables spectral purity enhancement of especially CO_2 generated Sn LPP sources without losses in throughput of the EUV imaging system. An additional technical advantage over transmission filters is the robustness of the reflective optical component, allowing straightforward integration and cooling. Further study will be mainly devoted to the deposition process of EUV optimized multilayer coatings on blazed gratings, whereas the focus is on replicating the blazed grating structure through the multilayer stack.

IV. Acknowledgements

We acknowledge financial support from SenterNovem through the 'ACHieVE' and EAGLE programs coordinated by ASML.

V. References

[1] Harned N., Goethals M., Groeneveld R., Kuerz P., Lowisch M., Meijer H., Meiling H., Ronse K., Ryan J., Tittnich M., Voorma H-J., Zimmerman J., Mickan U., Lok S., Proc. SPIE **6517**, San Jose (2007).

---

[2] Yakshin A.E., van de Kruijs R.W.E., Nedelcu I., Zoethout E., Louis E., Bijkerk F., Enkisch H., Müllender S., Proc. SPIE **6517**, San Jose (2007).

[3] E. Louis, R.W.E. van de Kruijs, A.E. Yakshin, M.M.J.W. van Herpen, D.J.W. Klunder, S. Alonso van der Westen, H. Enkisch, S. Muellender, L. Bakker, V Banine, M. Richter, and F. Bijkerk, Proc. SPIE **6151**, San Jose (2006).

[4] M. M. J. W. van Herpen, R. W. E. van de Kruijs, D. J. W. Klunder, E. Louis, A. E. Yakshin, S. Alonso van der Westen, F. Bijkerk, and V. Banine, Opt. Lett. Vol. **33**, Issue 6, pp. 560-562.

[5] D.L. Windt, Comput. Phys. **12**, 360 (1998).

[6] J.A. Liddle, F. Salmassi, P.P. Naulleau and E.M. Gullikson, J. Vac. Sci. Technol. B **21** 2980 (2003).

Chapter 6

Characterization of Mo/Si multilayer growth on stepped topographies

A.J.R. van den Boogaard, E. Louis, E. Zoethout, K.A. Goldberg, F. Bijkerk

Mo/Si multilayer mirrors with nanoscale bilayer thicknesses have been deposited on stepped substrate topographies, using various deposition angles. The multilayer morphology at the step-edge region was studied by cross section transmission electron microscopy. A transition from a continuous- to columnar layer morphology is observed near the step-edge, as a function of the local angle of incidence of the deposition flux. Taking into account the corresponding kinetics and anisotropy in layer growth, a continuum model has been developed to give a detailed description of the height profiles of the individual continuous layers. Complementary optical characterization of the multilayer system using a microscope operating in the extreme ultraviolet wavelength range, revealed that the influence of the step-edge on the planar multilayer structure is restricted to a region within 300 nm from the step-edge.

I. Introduction

The optical characteristics of nanoscale thin film multilayer structures deposited on substrates with a strictly controlled surface figure and roughness are subject to numerous studies. For semi-flat superpolished substrates (rms roughness $\leq$ 0.1 nm) the alternating parallel layers may serve as a Bragg-reflector for extreme ultraviolet (EUV) or soft x-ray radiation, yielding high specular reflectance in near-normal conditions. Multilayer structures deposited on 3D patterned substrate topographies have great potential as high efficiency diffractive optics, e.g. applicable as a monochromator [1], or in high resolution spectrometry [2,3], and as reflective phase-mask for EUV lithography [4]. Recent studies mainly focus on fabrication methods of suited substrate topographies such as gratings which meet the Bragg-reflector imposed quality demands on roughness levels [1,2,5]. However, the optical response of mentioned systems depends on the replication efficiency of a pre-defined substrate topography in the deposited multilayer structure. Near key features like step-edges the multilayers will show deformations from the desired, i.e. locally planar, structure. This causes spectral and spatial shifts in the optical response and general reflectance losses, which will be of increasing significance at downscaled pitch dimensions. Detailed knowledge on near step-edge layer growth is therefore required to gain understanding of the performance of diffractive optical multilayer devices, and indicate routes to further optimization. Besides, the findings might be of relevance to other fields of research concerned with the morphology of deposited nanostructures as physically synthesized multilayer nanoparticles [6].

Substrate replication in thin films deposited by physical layer deposition at room temperature show generic dependence on two deposition parameters: geometrical factors and the energy of the adparticles [7,8]. Hereby the substrate replication direction and the substrate profile relaxation are determined, respectively. For the purpose of separately addressing these dependencies, it is desirable to use a well controlled and isotropic deposition flux and a surface relaxation treatment decoupled from the primary layer growth process. In this chapter a study to Mo/Si multilayers deposited under various angles near substrate step-edges, via electron-beam physical vapor deposition (e-beam PVD) and subsequent low energy Kr^+-ion exposure, is presented. The individual bilayer profiles in the step-edge region have been studied by cross section transmission electron microscopy (cs-TEM). To characterize the samples with high sensitivity for the multilayer periodicity, and over a lateral area extending the range of cs-TEM, the Actinic Inspection Tool (AIT) [9] at the Berkeley Centre for X-ray Optics has been used. This state of the art EUV microscope provides a sub-100 nm spatial resolution in the $\lambda = 13.5$ nm wavelength range.

II. Layer growth evolution equations

The data are discussed in terms of a model description of the bilayer profiles throughout the multilayer structure. The continuum formalism as proposed by Stearns *et al*. is used [10]. The layer height profiles are given by $h_N(x)$ at bilayer number N, as measured from the plane of the substrate with surface normal $\vec{z}$, and $\vec{z} \perp \vec{x}$. Only normal incidence deposition is considered in reference [10], with the surface normal of the layer growth front $\vec{n}$ is parallel to $\vec{z}$. The layer profile evolution is given by the recursion relation:

$$h_{N+1}(f) = F[h_N(x) + d + \partial_{nl}(x)]\exp(-t_{sput} \times b(f)), \qquad (6.1)$$

$$h_{N+1}(x) = F^*[h_{N+1}(f)]$$

where $F[...]$ and $F^*[...]$ indicate a Fourier transform and its inverse, respectively, and

$$b(f) = \sum_i v_i (2\pi f)^i . \qquad (6.2)$$

Equation (6.1) gives the combined effect of layer growth by one-to-one replication with offset value d indicating the bilayer thickness i.e. d-spacing, and $\partial_{nl}(x)$ terms in layer growth depending non-linearly on local surface profile derivatives. The exponent can be considered as a damping term on the Fourier components defining the layer profile at the spatial frequency f domain, for proportionality coefficients v_i as associated with ion-enhanced layer growth kinetics during sputtering over a thickness t_{sput}. In order to address the layer growth direction as a variable, the authors here propose the following basic substitution:

$$d + \partial_{nl}(x) \to \vec{z} \cdot (d\vec{n} + \vec{\partial}_{nl}(x)) \text{ and} \qquad (6.3)$$

$$(x)_{N+1} = (x + \vec{x} \cdot (d\vec{n} + \vec{\partial}_{nl}(x)))_N ,$$

with d the multilayer bilayer thickness. An explanatory model of the experimental data is based on the above general equations. The development and further implications imposed by the experimental conditions under consideration are described in section III.C.

III. Experimental

III.1 Multilayer deposition

Commercially available polished crystalline Si (100) wafers were cleaved parallel to a wafer flat, to serve as substrates for high reflective EUV Mo/Si multilayers. The cleaving process produces well defined, rectangular sample edges near which the multilayer morphology is studied. Mo/Si multilayers with 50 bilayers of 6.95 nm thickness and a Mo to (Mo+Si) thickness ration of 0.4 were deposited. PVD at room temperature and high vacuum conditions with a base pressure of 10^{-9} mbar have been employed. Surface smoothening was obtained by a 130 eV Kr^+ ion polishing treatment after deposition of each Si layer, during which an excess layer of 0.5 nm Si was removed by physical sputtering. The Kaufmann ion source was mounted under an angle of 45° with respect to the axis of substrate rotation. The described deposition conditions and multilayer composition yield amorphous Si and nanocrystaline Mo layers [11].

The deposition geometry was controlled by using an electron beam generated spatially confined melt of target material with a typical diameter of 2 cm to produce the evaporation plume, resulting in a deposition rate of $1\text{-}2\times10^{-2}$ nm/s at a working pressure of 10^{-7} mbar. The samples were mounted at a substrate holder rotating at 1 Hz at a distance of 1 meter from, and with the axis of rotation aligned with, the melt of target material. The low working pressure (leading to a 10^3 m mean free path) and deposition geometry gives enhanced control and isotropy of the deposition flux compared to other deposition methods such as magnetron sputtering. The local angle of incidence of the deposition flux was constant during sample rotation and isotropic within 0.5°. Adjustments to the sample position and orientation were made to modify the local angles of incidence of the deposition flux: α_{depo} = -2.65°, 2.65°, and 3.95° (Fig.6.1(a)).

III.2. Characterization

III.2.a Cross section transmission electron microscopy

The cs-TEM specimens were prepared in sandwich shape, containing the sample under study and some supporting Si wafer material, making use of a two component resin. The cross section was taken perpendicular to the cleaving edge. A disk shaped sample was extracted and further processed by the method of dimpling-grinding/polishing, in order to minimize preparation induced artifact near the fragile edge region. For the final thinning of the sample by Ar^+-etching, sequential processing/TEM-inspection cycles were performed to ensure that the edge region and the protecting resin remained intact. Given the phase of the multilayer structure TEM contrast is governed by mass differences. Therefore images were recorded in bright-field conditions as to provide maximum contrast and the best possible visibility of any deviations from the periodicity of the Mo/Si stack. Sample alignment was obtained along the (011) zone axis from the crystalline Si substrate. All measurements have been performed at an acceleration voltage of 300 kV in a Philips CM300ST-FEG TEM, with focus on the step-edge region.

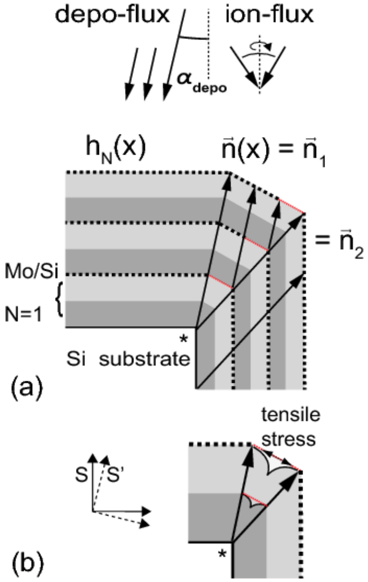

Fig.6.1 Schematic deposition geometry and recursive layer profiles for anisotropic layer growth into $\vec{n}_1$ and $\vec{n}_2$. (*) Indicates step-edge under study. Thin lines (red) represent interpolated data.

III.2.b EUV reflectometry measurements

Reflectance measurements were performed at the Center for X-ray Optics, making use of the Advanced Light Source synchrotron facility. At large distances from the step-edges, the reflectance spectrum around 13.5 nm and at 5° from the local surface normal was measured. Reflectance measurements near the step-edge were performed employing the AIT; for a detailed description of the apparatus is referred to [9]. The step-edge regions of the samples were illuminated uniformly at wavelengths in the range 13-14 nm and 6° from the sample plane normal. A zoneplate with a numerical aperture of 0.075 was used to project the reflected radiation from a diffraction limited spot onto a CCD camera at the back focal plane with a 907x magnification, providing an EUV intensity image of the sample with a spatial resolution better than 100 nm. Per recorded image the measuring geometry was kept mechanically fixed, and the wavelength dependence of the focal length of the zoneplate was used to obtain through-focus image series. By adjusting the sample-zoneplate distance, two through-focus series were obtained with the multilayer surface in focus at different wavelengths. For straightforward comparison and highest spatial resolution, the images with the optical surface in-focus have been processed.

III.3. Continuum model simulations

The recursion relation (equations (6.1) to (6.3)) was numerically evaluated at an array of data points in a Cartesian coordinate system S (xz) on a fixed uniform grid representing $h_0(x)$ as a (close to) 90° step-edge (Fig.6.1). By linear interpolation the data was projected at the initial grid where applicable, after each recursive step. This method allows modeling anisotropic layer growth by introducing spatially dependence in the layer growth front $\vec{n} \rightarrow \vec{n}(x)$ in equation (6.3), while maintaining the uniformity of the grid as required for the fast Fourier transform algorithm used. To obtain ample sampling points at the step-edge side, for enhanced numerical stability of the algorithm, the Fourier transform was applied in a coordinate system S' which is rotated as compared to S. For practical reasons an angle of arctan(0.25) was chosen. It should be noticed that for a non-flat substrate the layer growth model does not prescribe a preferential coordinate system in which the Fourier transform should be evaluated, hence S' can be chosen arbitrary as long as regarded as a model parameter.

For the described multilayer structure and deposition conditions two non-linear contributions to equation (6.3) are considered relevant $\vec{\partial}_{nl}(x) = \vec{\partial}_{comp}(x) + \vec{\partial}_{sput}(x)$ [10], with

$$\vec{\partial}_{comp}(x) = C(1 - 1/(\vec{\xi}(x) \cdot \vec{n}))\vec{n} \text{ and,} \tag{6.4}$$

$$\begin{aligned} &\vec{\partial}_{sput}(x) = \\ &-t_{sput}(\vec{\xi}(x) \cdot \vec{n}_{sput})^{p_1} \exp[-p_2(\vec{\xi}(x) \cdot \vec{n}_{sput})^{p_3} - 1]\vec{n}_{sput} \cdot \end{aligned} \tag{6.5}$$

Equation (6.4) addresses compaction into the local surface normal direction ($\vec{\xi}(x)$), driven by silicide formation of thickness C at the multilayer interfaces [12]. Equation (6.5) describes layer removal by physical sputtering resulting from the noble ion exposure. In its simplest representation the process can be regarded as inverse growth with a layer front $\vec{n}_{sput}$. The above universal analytic expression was used to account for anisotropy in sputter yield as a function of local angle of incidence of the ions at the surface, with coefficients p_1, p_2, p_3. Corresponding to reference [10] the parameters in equation (6.5) were chosen $p_1 = 1.7$, $p_2 = 2.1$, and $p_3 = 2.4$. Moreover, sample rotation ($\omega\vec{z}$) introduced a 2π-periodic modulation in the local surface normal $\vec{\xi}(x) \rightarrow \vec{\xi}(x,\phi)$, with $\omega t \equiv \phi$, relative to the fixed Kr$^+$ ion sputtering geometry. The effective sputter yield therefore was calculated by averaging the scalar part of equation (6.5) over $0 \le \phi \le 2\pi$, yielding $\langle \partial_{sput} \rangle_\phi (x)$. For regions in the shadow of the of the ion flux, $\vec{\xi}(x,\phi)\cdot\vec{n}_{sput} < 0$, the sputter yield was set to zero. The sample rotation results in a symmetric and more uniform effective sputter yield as a function of the surface tangent (Fig.6.2).

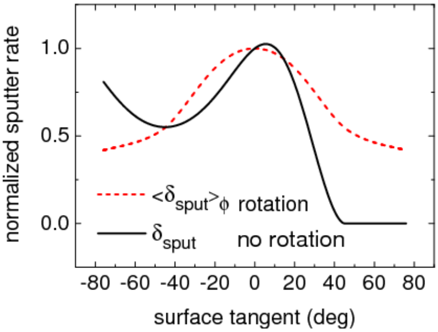

Fig.6.2 Normalized sputter yield (equation (6.3)) for 45° angle of incidence ions relative to the 0° surface tangent, with sample rotation (azimuthally averaged) and without. In the case of no rotation, ions propagate parallel to the surface for +45° surface tangent.

IV. Results and Discussion

IV.1. cs-TEM analysis

Cross section TEM graphs of the multilayers at the step-edge region are shown in Fig.6.3. At the resolution required for proper imaging the bilayer profiles show no indications of any influence of strain, dislocations, and vacancies are observed. In general, the influence of the discontinuous substrate on the multilayer structure predominantly manifests within a lateral distance ± 100 nm ($\vec{x}$) from the step-edge. A three-zone structure diagram is proposed for further discussion of the cs-TEM data.

The step-edge upper terrace expanded into the negative deposition direction defines zone (i). Here a continuous layer structure is observed, with slightly bended layer profiles near the zone boundary. A uniform layer growth front directed towards the deposition flux at the entire step-edge substrate implies lateral confinement of the semi-parallel multilayer to zone (i). The observation of the multilayer extending beyond the zone boundary (i) in positive x-direction, gives a first indication of anisotropic layer growth.

At zone (ii) a transition from the well defined but increasingly bending layers, towards a disordered morphology in which besides the multilayered structure a columnar structure can be recognized, is apparent. Columnar layer growth is typical for the intensively studied regime of layer growth at glancing angle thin film PVD [13]. As is determined empirically from the cs-TEM graphs, the transition occurs at a critical local derivative of the upper layer profile function of approximately $\partial_x h(x) = -\tan(\alpha_{depo} + 42^\circ) \equiv \partial_x h_{col}$. The orientation of the columns indicates a growth front inclined towards the local surface normal with an angle α_{col} measured from $\vec{z}$; α_{col} = 21° for α_{depo} = 2.65° and 3.95°, and α_{col} =11° for α_{depo} = -2.65°. The differences might not be attributed entirely to the deposition conditions, but also to the non-identical step-edge shapes. The observations are in general agreement with the Lichter-Chen model on columnar layer growth [14], which is based on finite mobility of adparticles before condensation and self-shadowing of condensation nuclei.

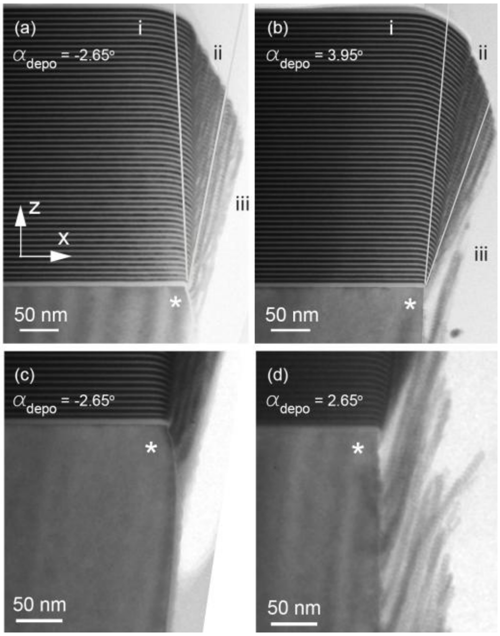

Fig.6.3 Cross section TEM graphs of Mo/Si multilayers on cleaved Si wafers. Boundaries zone (i)-(ii)-(iii) indicated by the lines. **(a)** α_{depo} = -2.65°, **(b)** α_{depo} = 3.95°, **(c)-(d)** details step-edge side unexposed and exposed to deposition flux, respectively.

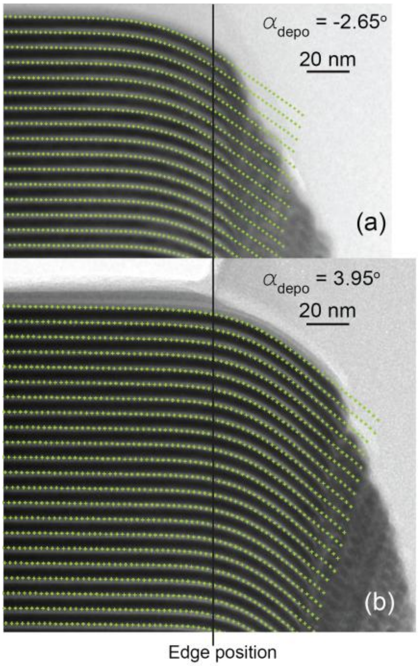

Fig.6.4 Comparison of simulations and data for model parameters in Table 6.I. Cross section TEM data details **(a)** and **(b)** were obtained from the overview graphs in Fig.6.3(a) and Fig.6.3(b), respectively.

The third zone covers the fully columnar layer structure, with corresponding layer growth front, as observed at the step-edge side. A clear view on this region is given by Fig.6.3(c) and Fig.6.3(d). At α_{depo} =-2.65° the side was not exposed to the deposition flux while for α_{depo} =2.65° and 3.95° the columnar structures are unambiguously observed. The columnar bilayers thickness is reduced as compared to the continuous multilayer structure:

$d_{col} < d$. This may be caused by the disordered layer morphology and consequent large interface area, propagating (dense) compound formation.

The observations show strong analogies with reported behavior of other Bragg-reflector multilayer systems on grating topographies, such as La/B_4C and Mo/B_4C [15,16]. This justifies a broader applicability of the three zone structure diagram for a class of nanoscale multilayer systems other then Mo/Si. Suppression of columnar layer growth would be desirable for facilitating straightforward zone (i) substrate replication. An adjusted deposition geometry or substrate design could both be viable methods to achieve this, but the consequences to device design and functionality should be further examined.

IV.2. Simulation results

The model parameters used in the simulations are given in Table 6.I. The anisotropic layer growth directions are addressed, where the columnar layer growth occurs for surface profile derivatives $\leq \partial_x h_{col}$. A quantitative explanation of the columnar layer morphology is beyond the scope of the continuum model. The simulated data are therefore depicted up to the critical surface profile derivative $\partial_x h_{col}$. It is noted that hereby the extent to which the continuous layers overhang the edge is somewhat overestimated; in the experimental data the transition to the columnar layer is observed closer to the projected step-edge position (Fig.6.4). The discrepancy may relate to the *a priory* assumption of continuous layer formation at zone (ii), as implied by the linear interpolation of data points between at the onset of columnar growth. Although not further investigated, continuous layer formation at the transition region is expected to be inhibited by high tensile stresses arising from the anisotropy in layer growth directions (Fig.6.1(b)).

The gradually bending of each individual bilayer in the multilayer structure is accurately described for zone (i) and zone (ii), up to the point the continuity of the layers breaks. Fourier component relaxation in the surface profile functions is governed by viscous flow and free volume annihilation ($\propto 2\pi f$) [17], ion-driven surface currents ($\propto (2\pi f)^2$) [18], and surface confined viscous flow ($\propto (2\pi f)^4$) [19,20]. The non-linear terms given by equation (6.4) and equation (6.5) have a minor influence on the layer profile evolution at realistic parameter values. Fig.6.5 represents the simulated layer profile functions at varying bilayers number. An increase in deposition angle mainly translates into a lateral shift of the layer profiles into the positive x-direction (Fig.6.5(a) and Fig.6.5(b)). An enhanced flatness of the layer profiles at the step-edge region is observed for reduced ion-induced kinetics, of which the ion-sputtered layer thickness provides experimental control under presented deposition conditions (Fig.6.5(c) and Fig.6.5(d)). Restriction of the ion sputtering treatment will simultaneously reduce the mitigation of substrate replicated and layer growth intrinsic interface roughness. Depending on substrate roughness and multilayer composition this might compromise the Bragg-reflector quality.

TABLE 6.I. Continuum model parameters as used in the simulation. Errors relate to uncertainties in experiment and data extraction from the cs-TEM graphs.

Deposition angle (deg): α_{depo}	-2.65 ± 0.5	2.65 ± 0.5	3.95 ± 0.5
Number of bilayers: N	50	50	50
D-spacing (nm): d	7.45 ± 0.05	7.45 ± 0.05	7.45 ± 0.05
Sputtered thickness (nm): t_s	0.5 ± 0.05	0.5 ± 0.05	0.5 ± 0.05
ν_1 (dimensionless)	0.1	0.1	0.1
ν_2 (nm)	2	2	2
ν_4 (nm^3)	20	20	20
Bilayer thickness column (nm): d_{col}	0.9 ± 0.05	0.88 ± 0.05	0.88 ± 0.05
Column tilt (deg): α_{col}	11 ± 1	21 ± 1	21 ± 1
Compaction (nm): C	0.4	0.4	0.4
Critical surface derivative: $\partial_x h_{col}$	-39.35 ± 1.5	-44.26 ± 1.5	-44.95 ± 1.5

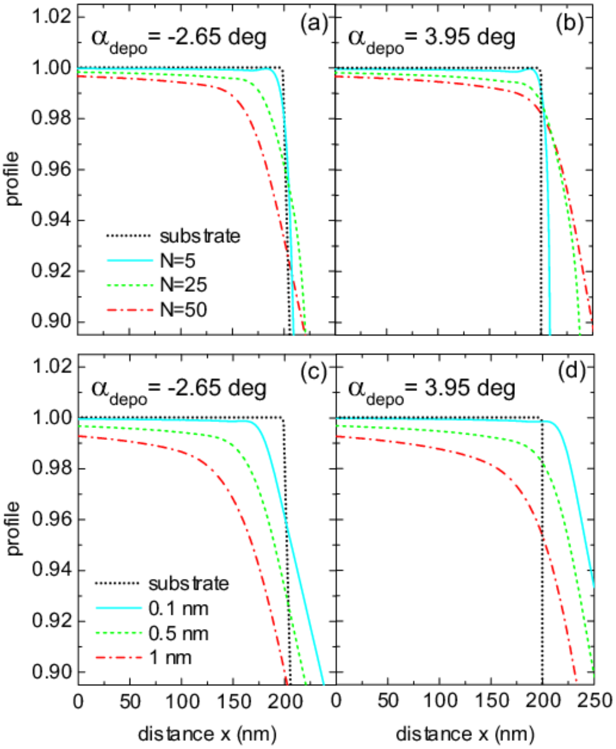

Fig.6.5 Normalized layer profiles based on parameters in Table 6.I. **(a)-(b)** Various bilayer number (N). **(c)-(d)** Various ion-sputtered thickness for N = 50.

IV.3. EUV reflectometry

In the spectral EUV reflectance data obtained far from the step-edges, a maximum is observed at a wavelength of 13.57 nm (Fig.6.6(a)). Correspondingly, the d-spacing is found to be 6.98 nm as derived from Fresnel equation based calculations using the IMD computer code [21], for a four-layer multilayer system with a layer of 0.6 nm and 1 nm of $SiMo_2$ at the Si-on-Mo and Mo-on-Si interface [22], respectively, and 1.7 to 2 nm of native oxide at the Si terminated 50 bilayer stack.

Fig.6.6(b) represents the in-focus AIT reflection profiles obtained near the step-edge, as a function of in-plane distance to the step-edge, for α_{depo} = -2.65° and 2.65°. The data have been normalized on a first-order polynomial fit to the data at the region 0-500 nm, to correct for small misalignment and beam aberrations. The reflection profiles are almost flat up to a point were the signal significantly increases, with a maximum increase of ΔI, followed by a drop-off towards zero reflection. It should be noticed that the wavelength in the AIT experiments is shorter than the wavelength of maximal reflectance at a d-spacing of 6.98 nm. Hence the increased reflected intensity at the sample edge indicates a closer matching of the Bragg-condition for constructive interference caused by a reduced d-spacing at the edge of the samples. IMD calculations show that the observed wavelength dependence in ΔI can be explained by assuming a decrease in d-spacing of Δd = 0.28% and 0.27% for α_{depo}= -2.65 ° and 2.65 °, respectively (Fig.6.7). To match the calculations with the measured data, a small positive offset in the calculated ΔI curves has been applied. Edge-diffraction effects are considered of minor importance; since in-focus images were selected for data analysis a minimized range in interfering phases contributes to the recorded intensity. However, the offset values might be attributed to knife-edge diffraction.

The reflectometry results can be well understood in terms of the continuum model simulations, which show a decrease in d-spacing of 0.3% for an almost unchanged surface normal at 125 nm from the step-edge (Fig.6.5), without strong dependence on α_{depo}. This position is directly related to the maximum reflectance in the AIT data. An even stronger bilayers thickness decrease, as observed in the cs-TEM images near the zone boundary (i)-(ii), implies an oblique surface normal and therefore misalignment in the AIT measurements, yielding a close to zero reflection. Considering the width of the peak in the AIT signal near the step-edge, the region for which the d-spacing is significantly reduced is estimated to be restricted to 300 nm from the wafer edge position.

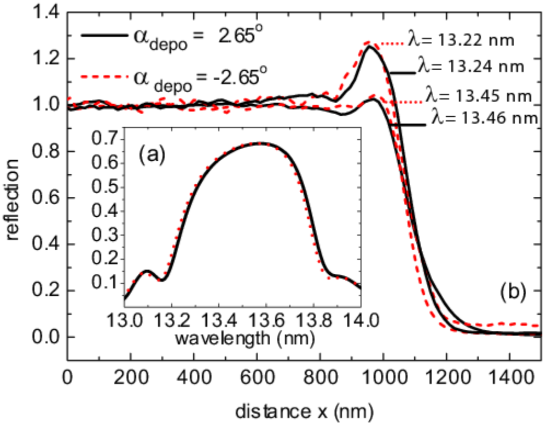

Fig.6.6 Reflectometry data, **(a)** wavelength scans far from the sample edge **(b)** AIT normalized reflection profiles at step-edge region.

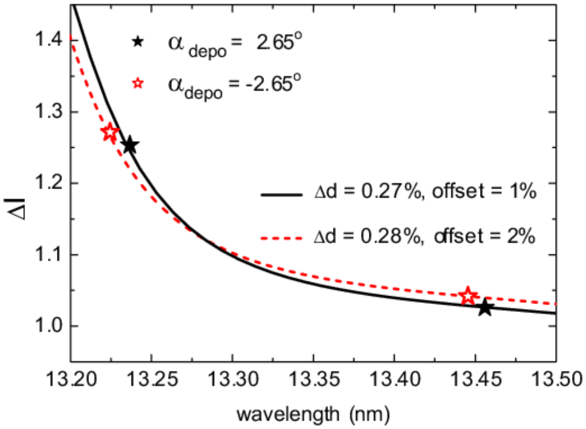

Fig.6.7 Increase in AIT reflection profiles near step-edges plotted against wavelength. IMD calculations (lines) and data shown.

V. Summary and Conclusions

Mo/Si multilayer structures have been deposited on stepped substrate topographies for isotropic deposition fluxes at various, close to normal, angles of incidence. The height profiles of the layers were studied by cs-TEM. The data are indicating continuous layer growth into the deposition direction at the upper step-edge terrace (zone(i)), a transition regime from continuous to columnar layer growth when approaching the step-edge (zone(ii)), and a fully columnar regime at the step-edge side (zone(iii)). The occurrence of the columnar layer growth is explained by the deposition conditions and geometry.

By applying a simple continuum model the layer profiles functions can be quantitatively described for the continuous layer regimes (zone(i) and (ii) up to the transition point). It accounts for the deposition geometry, ion-induced kinetics, compound formation, and most notably the anisotropic layer growth directions as associated with the transition from continuous to columnar layer growth. The observed gradual bending of the layer profiles at zone(i) and zone(ii) strongly depends on the ion-enhanced deposition conditions.

EUV reflection measurements using the Actinic Inspection Tool (AIT) have been used to measure the optical performance of the multilayers close to the step-edge and show a slightly affected reflectance at the step-edge region. This effect is related to a decrease in d-spacing of slightly less than 0.3%. The latter occurs at a distance of 125 nm from the step-edge, whereas the measurable optical perturbation of the planar multilayer is restricted to a region within 300 nm from the step-edge, as is quantitatively derived by comparison of the AIT data with the continuum model simulation.

VI. Acknowledgements

We acknowledge financial support from the AgentschapNL through the EXEPT and ACHieVE programs coordinated by ASML and the Foundation for Fundamental Research on Matter (Stichting voor Fundamenteel Onderzoek der Materie, FOM) and Carl Zeiss SMT GmbH through the Industrial Partnership Program XMO.Furthermore the authors wish to thank E.G. Keim of the MESA+ Institute for Nanotechnology for the TEM analysis, E.M. Gullikson at the Center for X-ray Optics for EUV reflectometry measurements, and B. LaFontaine at Cymer for making experimental time available on the AIT.

VII. References

[1] J.A. Liddle, F. Salmassi, P.P. Naulleau and E.M. Gullikson, J. Vac. Sci. Technol. B **21**, 2980 (2003).

[2] D.L. Voronov, M. Ahn, E.H. Anderson, R. Cambie, C.-H. Chang, E.M. Gullikson, R.K. Heilmann, F. Salmassi, M.L. Schattenburg, T. Warwick, V.V. Yashchuk, L. Zipp, and H.A. Padmore, Opt. Lett. **35**, 15 (2010).

[3] I.V. Kozhevnikov, R. van der Meer, H.M.J. Bastiaens, K,-J. Boller, and F. Bijkerk Opt. Express **18**, 15 (2010).

[4] A.M. Nugrowati, A.S. van de Nes, S.F. Pereira, and J.J.M. Braat, Microelectron. Eng. **83**, (2006).

[5] D.L. Voronov, E.H. Anderson, R. Cambie, S. Dhuey, E.M. Gullikson, F. Salmassi, T. Warwick, V.V. Yashchuk, and H.A. Padmore, Nucl. Instr. and Meth. A (2010) doi:10.1016/j.nima.2010.11.064.

[6] W. Hu, M. Zhang, R.J. Wilson, A. Leen Koh, J.-S. Wi, M. Tang, R. Sinclair, and S.X. Wang, Nanotechnology **22**, 185302 (2011).

[7] E.M. Gullikson and D.G. Stearns, Phys. Rev. B **59**, 20 (1999).

[8] D.G. Stearns, Appl. Phys. Lett. **62**, 1745 (1993).

[9] K. A. Goldberg, I. Mochi, P. Naulleau, T. Liang, P.-Y. Yan, and S. Huh, J. Vac. Sci. Technol. B **27**, 2916 (2009).

[10] D.G. Stearns, P.B. Mirkarimi, and E. Spiller, Thin Solid Films **446**, 37 (2004).

[11] R.W.E. van de Kruijs, E. Zoethout, A.E. Yakshin, I. Nedelcu, E. Louis, H. Enkisch, G. Sipos, S. Müllender, and Fred Bijkerk, Thin Solid Films **515**, 430 (2006).

[12] R.S. Rosen, D.G. Stearns, M.A. Viliardos, M.E. Kassner, S.p. Vernon, and Y. Cheng, Appl. Opt. **32**, 34 (1993).

[13] M.M. Hawkey and M.J. Brett, J. Vac. Sci. Technol. A **25**, 5 (2007).

[14] S. Lichter and J. Chen, Phys. Rev. Lett. **56**, 13 (1986).

[15] D. Häussler, E. Spiecker, S. Yang, W. Jäger, M. Störmer, R. Bormann, G. Zwicker, Status Solidi A **202**, (2005).

[16] D. Häussler, E. Spiecker, W. Jäger, M. Störmer, R. Bormann, C. Michaelsen, J. Wiesmann, G. Zwicker, R. Benbalagh, J.-M. André, P. Jonnard, Microelectron. Eng. **84**, (2007).

[17] A.J.R. van den Boogaard, E. Louis, E. Zoethout, S. Müllender, and F. Bijkerk, J. Vac. Sci. Technol. A **28**, 4 (2010).

[18] M. Moseler, P. Gumbsch, C. Casiraghi, A.C. Ferrari, and J. Robertson, Science **309**, 2 (2005).

[19] S.E Orchard, Appl. Sci. Res. A **11**, 451 (1962).

[20] C.C. Umbach, R.L. Headrick, and K.-C. Chang, Phys. Rev. Lett. **87**, 24 (2001).

[21] D.L. Windt, Comput. Phys. **12**, 4 (1998).

[22] A.E. Yakshin, E. Louis, P.C. Görts, E.L.G. Maas, and F. Bijkerk, Physica B **283**, 143 (2000).

Chapter 7

Wavelength separation from extreme ultraviolet mirrors using phaseshift reflection

A.J.R. van den Boogaard, F.A. van Goor, E. Louis, F. Bijkerk

A generic design and fabrication scheme of Mo/Si multilayer-grating phaseshift reflector systems is reported. Close to optimized extreme ultraviolet (EUV, $\lambda = 13.5$ nm) reflectance values up to 64% are demonstrated, while the diffractive properties can be exploited in spectral filtering applications. The results can contribute to a wavelength-unspecific solution for the suppression of $\lambda > 100$ nm out-of-band radiation in EUV lithography.

I. Introduction

Optical multilayers are used as high reflective elements in extreme ultraviolet (EUV, $\lambda = 13.5$ nm) down to the soft x-ray wavelength range. Typically consisting of alternating layers of a spacer and metal reflector of nanoscale thickness, these structures serve as Bragg-reflecting artificial crystals. For longer wavelengths ($\lambda > 100$ nm) the optical response is similar to efficient single layer mirrors due to the metal fraction in the multilayer. In some applications however, most notably new optical lithography techniques operating at EUV wavelengths [1], optical throughput outside the EUV transmission band is undesirable and the broad band emission properties of the EUV light source indicates the necessity of spectral filtering. The out-of-band wavelength ranges concern vacuum ultraviolet (VUV, 100-400 nm) and infrared (IR, mainly 10.6µm CO_2-laser output), as both present in the spectrum of laser produced Sn-plasma EUV sources [2,3]. The use of foil or grid transmission filters is pursued [3], but this causes undesired EUV throughput losses and energy dissipation may be troublesome during intense illumination.

An increasing amount of attention is attributed to multilayer optics having a more selective spectral response. Multilayers with anti-reflective layers [4-6], as well as multilayer-grating based solutions have been proposed [7,8]. For the latter the filtering principle is based on diffraction caused by the 3D shape of the device, allowing for the use of a Mo/Si multilayer optimized on EUV reflectance, giving a near normal peak reflectance up to 70%. The conventional deposition of multilayers on gratings is successfully used in applications were spectral resolution is critical [9]. However, the yet obtained device quality in terms of roughness, profile of the facets and multilayer deformations near step-edges still compromises ultimate EUV throughput. An alternative design and unconventional deposition scheme of a multilayer-grating system suited for spectral filtering is reported in this chapter, with a process flexibility enabling much tighter specifications on multilayer profile and interface quality and hence EUV performance.

II. Design and functionality

The proposed system consists of a rectangular multilayer add-structure on a planar substrate-multilayer with a pitch Λ and a step height h. Depending on the application a spacing layer of thickness h_s can be used to reach the desired step height (Fig.7.1(a)). The coverage fraction of the substrate-multilayer by the add-multilayer is chosen 0.5. For near-normal plane-wave illumination conditions this gives equal contributions to the reflected wave front from both regions, whereas a phaseshift is caused by the optical path length difference. Rigorous calculations using the PCGrate software package [10] reveal that the thus described phaseshift reflector (PsR) will suppress the $m=0$ order in diffraction for $\lambda=4h$, yielding a π-phaseshift, hereby diffracting the energy into higher orders of which $m=\pm1$ have the highest efficiency (Fig.7.1(b)). In the EUV wavelength range, the 0^{th} order is the most efficient, given that the add-multilayer structure and the substrate-multilayer are in-phase. The near 0^{th} orders will closely approach flat multilayer mirror reflectance efficiency; the cumulative efficiency of orders $m\geq|\pm3|$ is 1-2 percent. Since the angular inter-order separation is proportional to λ/Λ, as is obtained from the grating equation for near normal incidence illumination and $\Lambda>>\lambda$, the described device is suited to spatially separate EUV radiation from longer wavelengths.

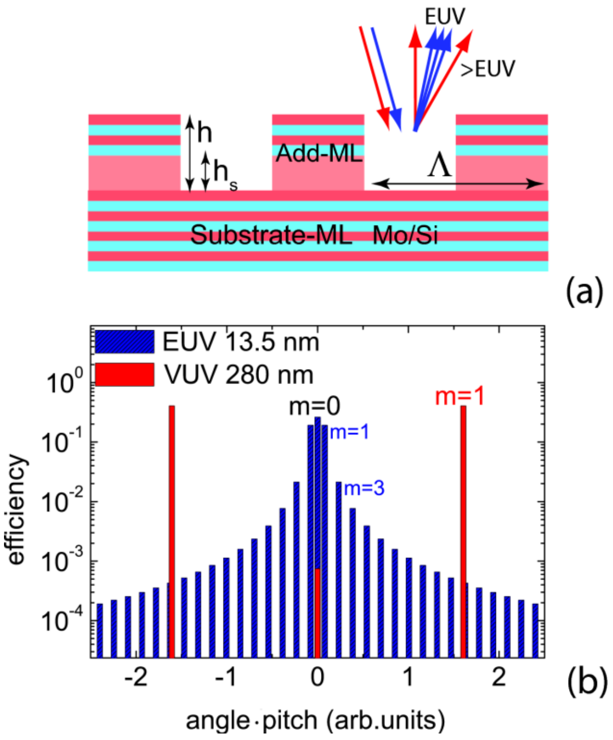

Fig.7.1 **(a)** Schematic phaseshift reflector structure. **(b)** Efficiency orders of diffraction versus angular position for $h=70$ nm and normal incidence illumination.

III. Experimental

Devices suitable for suppression of VUV (PsR-VUV, $\lambda = 280$ nm) and IR (PsR-IR, $\lambda = 10.6$ µm) have been produced. The deposition scheme was based on the application of a removable contact mask during the deposition of the add-multilayer and optional spacer layer. The substrate-multilayer was deposited in advance onto a substrate of choice, and consists of 50 bilayers Mo/Si with a bilayer thickness of 6.95 nm, and a Mo fraction of 0.4. For the PsR-VUV, the add-multilayer consists of 10 bilayers of the same composition as the substrate multilayer resulting in $h = 69.5$ nm, with no spacer layer (h_s =0). Micro-mesh foils which are generally utilized as microscopy calibration grids were selected as contact masks. The foils feature a 2D rectangular mesh pattern with square apertures of 18 µm, a wire size of 7.4 µm ($\Lambda = 25.4$), 50% open area, and a thickness of 2-5 µm. The mask thickness/aperture ratio, here denoted as R_a, is an important parameter in the deposition and for the micro-mesh foils $R_a = 0.1$ to 0.3. This indicates the necessity of a highly isotropic, near-normal deposition flux to obtain sharp replication of the mesh into the deposited structure. Electron beam generated physical vapor deposition (PVD) at high vacuum conditions was employed [11] where the angular spread in incident directions at the sample was in the order of 1° from normal. The demands on deposition angle and isotropy obstruct the use of typically applied off-normal ion-enhanced deposition conditions for smoothest layer growth during the add-multilayer deposition [12]. For the here reported prototypical demonstration, ion assistance was omitted. Furthermore, for the shallow add-multilayer structures agglomeration of roughness is considered to be not critical. The phase requirement of the add-multilayer structure was satisfied by using *in-situ* reflectometry for layer thickness control during deposition. Operating at the C-K_α emission line at 4.47 nm wavelength, the layer thickness control signal was determined by reflections from the layer growth front and several buried interfaces. This enables close matching of the phase of the add-structure with the substrate-multilayer.

For the PsR-IR the add-structure consists of a Si spacer layer $h_s = 2.3$ µm and a 50 bilayer Mo/Si multilayer. The relatively large layer thickness showed to be a complicating factor for two reasons; a thicker foil contact mask had to be applied due to mask deformation and displacements caused by layer stresses, and electron beam PVD without ion assistance could not be used due to accumulating surface roughness. Instead, magnetron sputter deposition was employed, yielding smooth layers growth as caused by the relatively high energy of the adatoms (~1 eV against ~0.1 eV for ebeam PVD) and the additional exposure to back scattered target sputtering ions of 10-100 eV. The deposition geometry gives local angle of incidence variations at the sample up to 10°, were the isotropy may be further influenced by the limited mean free path of $\approx 10^{-1}$ m at a working pressure of $\approx 10^{-5}$ mbar. Line masks with a thickness of 50 µm were required to obtain sharp add-structure projections. The deposition anisotropy and mask thickness imply that this deposition scheme is feasible at low mask thickness/aperture ratios and thus large pitch size only; $\Lambda = 2$ mm was selected giving $R_a = 0.025$. The fact that the substrate multilayer and the add-multilayer are optically separated by the spacer layer dissolves the phase requirement on the add-multilayer. As an alternative approach, a sacrificial photoresist structure can serve as a contact mask which is removed after deposition of the add-structure in a so-called “lift off” procedure. This currently investigated technique might be beneficial for producing smaller pitches. At a resist thickness (i.e. mask thickness) of 2-3 µm, the requirement of $R_a = 0.025$ would allow for downscaling to pitches of 100 µm.

IV. Results and Discussion

The samples (Fig.7.2(a)) were characterized on reflectance at the BESSY electron storage ring EUV beam line, at an angle of incidence of 1.5° from normal and with a detector aperture of ± 0.5°. EUV reflectance up to 64% is observed for the PsR-VUV sample (Fig.7.2(b)), where a reference substrate-multilayer and reference unmasked add-multilayer yield peak reflectance values of 68% and 61%, respectively. The 7% decrease is likely the result of a reduced interface quality in the absence of ion-enhanced growth conditions during the add-multilayer deposition. The wavelength dependency of the PsR-VUV reflectance closely approaches the combined average reflectance of the two reference samples (Fig.7.2(b), solid line), advocating a negligible influence of structural deformations near the edges of the add-multilayer, as is in line with reference [13]. Although the data indicate not yet fully optimized reflectance values for none of the two reference systems, an absolute near 0th order efficiency of 64% in the EUV wavelength range is the highest reported up till now for any type of wavelength separator, to the best knowledge of the authors. For the PsR-IR, an EUV peak reflectance of 63% has been observed as depicted in Fig.7.2(c). This is below the combined average of substrate-multilayer and unmasked add-multilayer (Fig.7.2(c), solid line), having a peak reflectance of 68% and 67%, respectively. The influence of structural imperfections, i.e. non-flat facets, probably is causing the reflectance decrements. These effects are considered to arise from the anisotropy of the deposition flux, leading to half-shadow regions during the deposition of the add-multilayer near the edges of the mask. Yet, the EUV throughput obtained from the PsR-IR so far is demonstrated to be well above the theoretic potential of alternative anti-reflection layers or transmission filtering approaches.

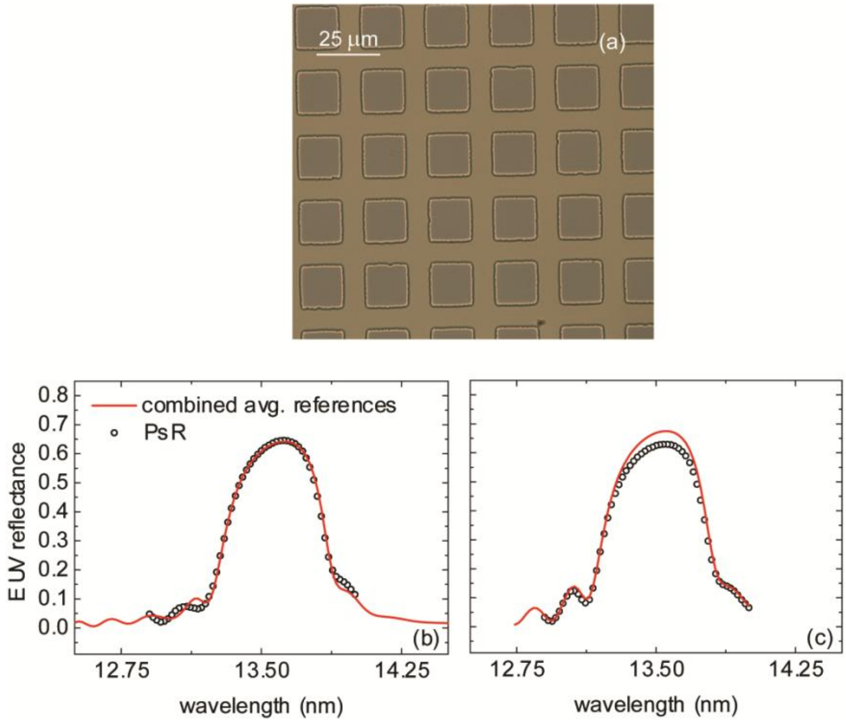

Fig.7.2 (a) Optical microscopic top view of PsR-VUV surface. EUV reflectance measurements for **(b)** PsR-VUV, and **(c)** PsR-IR. In both graphs the solid lines indicate combined average reflectance of substrate-multilayer and unmasked add-multilayer reference samples.

The diffractive response of the VUV phaseshift reflector has been analyzed in the wavelength range of 100-400 nm, at an angle of incidence of 4° from normal, and an angular resolution <0.4°. Suppression of the 0^{th} order with a factor 30 is observed in a broad band around the target wavelength of 280 nm (Fig.7.3(a)). The data is in agreement with rigorous calculations of the 0^{th} order in diffraction, accounting for an uncertainty in the pitch of ± 2.5 µm. The bandwidth of the suppression can be further extended, i.e. including the resonant wavelength at $\lambda = 2h$, by a series of phaseshift reflectors optimized for different wavelengths. For two successive systems, one with $\lambda_1 = 4h_1$ = 280 nm and one with $\lambda_2 = 4h_2 = 0.5\lambda_1$, the simulated VUV throughput shows a maximum ≤ 0.03 for the wavelength range 100-400 nm (Fig.7.3(a) dashed line). Detector scans on the intensity profiles of the diffracted VUV radiation at a fixed 4° normal angle of incidence are depicted in Fig.7.3(b) and Fig.7.3(c). Two-theta defines the angle between the incoming and the diffracted beam. Both the scanning axis and the rectangular PsR-VUV structure were aligned with the incident beam. The 0^{th} order suppression with respect to a reference mirror can be observed in Fig.7.3(b), and at several VUV wavelengths well separated and symmetric orders in diffraction are shown Fig.7.3(c), with an angular separation between the first maxima and the 0th order of 0.6 deg at 280 nm wavelength. It is emphasized that the separation is tunable by adjusting pitch dimensions.

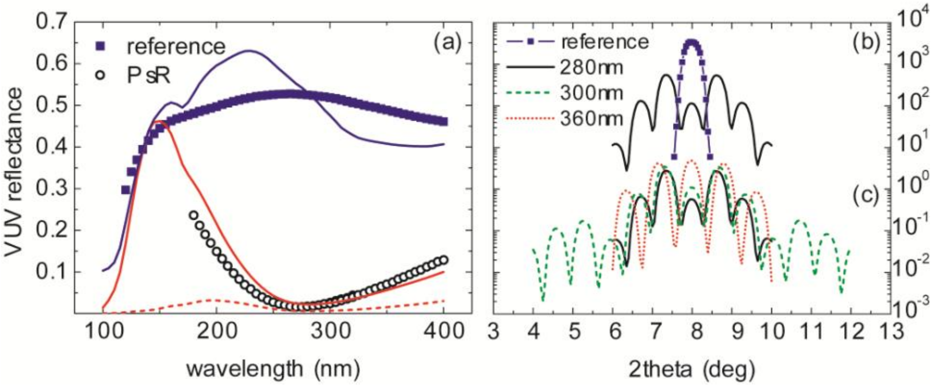

Fig.7.3 (a) VUV reflectance measurements of a phaseshift reflector (circles) and a reference unstructured multilayer mirror (squares), and calculations (solid lines). Also shown is a calculation of a combined PsR system response (dashed line). **(b)** Two-theta detector scans at 280 nm for the PsR and reference mirror, offset applied for visualization. **(c)** Two-theta detector scans PsR at various VUV wavelengths.

V. Conclusions

It is demonstrated that deposited multilayer phaseshift reflector structures can serve as high reflectance optical element in the EUV range (up to 64% reflectance measured) with drastically reduced throughput at out-of-band wavelengths, where a factor 30 reduction has been demonstrated experimentally at 280 nm. As a further advantage, the deposition scheme based on application of a removable contact mask during physical layer deposition, imposes no demands on multilayer composition or substrate material and hence can be considered generically applicable. Sharper mask projections into the deposited add-multilayer structures, and application of ion-enhanced layer deposition, will likely enable further optimization of EUV reflectance values. The parameters of main importance are the geometry of the (ion-enhanced) deposition conditions relative to the mask orientation, and the contact mask dimensions.

VI. Acknowledgements

We acknowledge financial support from the AgentschapNL through the EXEPT and ACHieVE programs coordinated by ASML and the Foundation for Fundamental Research on Matter (Stichting voor Fundamenteel Onderzoek der Materie, FOM) and Carl Zeiss SMT GmbH through the Industrial Partnership Programme XMO.

VII. References

[1]V. Banine and R. Moors, J. Phys. D **37**, 3207 (2004).

[2]I.V. Fomenkov, D.C. Brandt, A.N. Bykanov, A.I. Ershov, W.N. Partlo, D.W. Myers, N.R. Böwering, G.O. Vaschenko, O.V. Khodykin, J.R. Hoffman, E. Vargas, R.D. Simmons, J.A. Chavez, and C.P. Chrobak,. Proc. SPIE **6517**, 65173J (2007).

[3]W.A. Soer, M.J.J. Jak, A.M. Yakunin, M.M.J.W. van Herpen, and V.Y. Banine, Proc. SPIE **7271**, 72712Y (2009).

[4]M.M.J.W. van Herpen, R.W.E. van de Kruijs, D.J.W. Klunder, E. Louis, A.E. Yakshin, S. Alonso van der Westen, F. Bijkerk, and V. Banine , Opt. Lett. **33**, 560 (2008).

[5]W.A. Soer, P. Gawlitza, M.M.J.W. van Herpen, M.J.J. Jak, S. Braun, P. Muys, and V.Y. Banine, Opt. Lett. **34**, 3680 (2009).

[6]V.V. Medvedev, A.E. Yakshin, R.W.E. van de Kruijs, V.M. Krivtsun, A.M. Yakunin, K.N. Koshelev, and F. Bijkerk, Opt. Lett. **36**, 17 (2011).

[7]J.A. Liddle, F. Salmassi, P.P. Naulleau, and E.M. Gullikson, J. Vac. Sci. Technol. B **21**, 2980 (2003).

[8]A.J.R. van den Boogaard, E. Louis, F.A. van Goor, and F. Bijkerk, Proc. SPIE **7271**, 72713B (2009).

[9]D.L. Voronov, M. Ahn, E.H. Anderson, R. Cambie, C.-H. Chang,E.M. Gullikson, R.K. Heilmann, F. Salmassi, M.L. Schattenburg, T. Warwick, V.V. Yashchuk, L. Zipp, and H.A. Padmore, Opt. Lett. **35**, 2615 (2010).

[10]http://www.pcgrate.com/

[11]E. Louis, A. Yakshin, T. Tsarfati, and Fr. Bijkerk, Prog. Surf. Sci, (2011), doi:10.1016/j.progsurf.2011.08.001.

[12]A.J.R. van den Boogaard, E. Louis. E. Zoethout, S. Müllender, and F. Bijkerk, J. Vac. Sci. Technol. A **28**, 552 (2010).

[13]A.J.R. van den Boogaard, E. Louis, E. Zoethout, K.A. Goldberg, and F. Bijkerk J. Vac. Sci. Technol. B **29**, 051803 (2011).

Summary

Nanoscale molybdenum/silicon (Mo/Si) multilayer structures are the systems of choice to serve as reflective coatings on near normal incidence optical elements for wavelengths in the extreme ultraviolet (EUV, λ =13.5 nm) and the soft x-ray regime in general. EUV peak reflectance values above 70% are obtained routinely, which is only 4% below the theoretical maximum. This type of multilayer optics find an important application in the next generation optical lithography (operating at EUV wavelengths), in material analysis techniques, and in space telescopes. The deposition of multilayers requires utmost control of critical layer properties as composition, morphology, and interface thickness. This thesis focuses on physical vapor deposition (PVD) of thin (multi)layers at room temperature and, particularly, on the surface morphology resulting from the smoothening, noble gas ion treatment.

When using appropriate ion-beam parameters, Kr^+ bombardment and consequent sputtering of a-Si layers is known to suppress layer growth intrinsic roughness in Mo/Si multilayers. In chapter 2 the scalability of the smoothing process is investigated, aiming for optimization suppression of substrate roughness. The components of the roughness spectrum corresponding to in-plane length scales up to 500 nm are observed to be significantly suppressed by an extended Kr^+ sputtering treatment, leading to an increased EUV reflectance when applied on smoothening layers prior to the multilayer deposition. The roughness relaxation rate is observed to be proportional to the spatial frequency. This appears to indicate bulk-like viscous deformations and contradicts the locality (i.e. surface confinement) of the ion-treatment. The annihilation of near surface in-layer free volume during ion sputtering is demonstrated to result in a similar dispersion in smoothing kinetics and is shown to resolve the discrepancy.

Chapter 3 reports on modifications of the in-layer structure of a-Si layers by implantation of H^+ ions. As is in agreement with literature, the hydrogen retention in the a-Si layers is found to increase the layer porosity. Atomic concentrations of approximately 30% of H are obtained while reducing layer densities by 10% as compared to typical PVD a-Si. Since free volume annihilation during noble ion sputtering is identified as a layer smoothing process (chapter 2), the additional free volume in the a-Si:H layer was considered to potentially increase ion-induced layer smoothing. Indeed this effect is observed, yielding ultrasmooth Kr^+-sputtered a-Si:H layer surfaces, hereby further establishing the notion of ion-induced free volume annihilation as an important process of layer smoothing.

In chapter 4 the interface roughness in Mo/Si multilayers as a function of the noble gas ion polishing species (in order of increasing mass: Ne, Ar, Kr, and Xe) is investigated by grazing incidence small angle X-ray scattering

(GISAXS). The total scatter arising from interface roughness, as well as the vertical correlation in the roughness is observed to decrease with increasing mass of the noble polishing gas. Optimal interface smoothness is obtained by employing Xe^+ for polishing, however, Kr^+ polishing yields highest EUV reflectance. This result is clarified by the residual amounts of polishing gas in the Si layers, affecting the optical constants for EUV radiation significantly.

Chapter 5 discusses the application of an EUV reflective multilayer on a non-flat, grating substrate, which is appealing as a high EUV throughput optical filtering device for parasitic, so-called out-of-band wavelengths present in the spectrum of most EUV sources. Rigorous calculations on the working principle are presented and reveal full spectral separation of EUV from undesired infrared radiation (10.6 µm) for grating pitches of about 100 µm, with EUV reflectance values remaining close to that of a planar multilayer mirror. The deposition of multilayers onto non-flat substrate topographies as a model system for real gratings, is described in chapter 6. The individual bilayer profiles in multilayer structures deposited near substrate step-edges were studied by cross-section transmission electron microscopy (cs-TEM). An explanatory model of the resulting bilayer profile has been developed. Combining the model calculations with EUV microscopy measurements, it is derived that non-uniform replication of the step-edge substrate topography into the multilayer is predominantly caused by ion-induced profile relaxation. Yet, this effect occurs within a region very close (within 300 nm) to the step-edge only.

With the findings presented in chapter 6 multilayer deposition on a grating is shown feasible. However, the tolerances on grating roughness and flatness of the facets are extremely tight. In chapter 7 a deposition scheme of a class of rectangular grating phaseshift reflectors (PsR) on flat substrates is reported. These structures enable suppression of the 0th order of out-of-band radiation from the VUV (100-400 nm) to the infrared range. Experimentally, but not yet optimized, a 30 times suppression of out-of-band radiation at 280 nm is demonstrated, while preserving a high EUV reflectance of 64%.

Samenvatting

Molybdeen/silicium (Mo/Si) multilaag structuren van nanometer schaal, zijn zeer geschikt als reflectieve optische elementen voor loodrechte lichtinval in het golflengtegebied van het extreem ultraviolet (EUV, $\lambda = 13.5$ nm) en zachte röntgen straling. Hiermee kan een genormeerde EUV piek-reflectie van meer dan 70% worden behaald, wat dicht in de buurt komt van het theoretisch maximum. Dit type multilaag optiek is belangrijk in toepassingen zoals optische lithografie van de volgende generatie (waarin gebruik zal worden gemaakt van EUV), materiaal analyse technieken en ruimte telescopen. De fabricage van deze multilagen vereist controle over kritische laageigenschappen zoals de samenstelling, morfologie en de dikte van grenslagen tussen de materialen. Dit proefschrift beschrijft de depositie van dunne (multi)lagen bij kamertemperatuur door middel van fysisch opdampen. De nadruk ligt vooral op de invloed van een vervlakkende behandeling met edelgas ionen van oppervlakten en grenslagen in zowel vlakke multilagen als in 3D multilaag-tralie structuren.

Ruwheid als gevolg van laagaangroei in Mo/Si multilagen kan worden onderdrukt door middel van een bombardement van de Si lagen met krypton ionen (Kr^+). De schaalbaarheid van dit polijst proces en de mogelijkheid om ruwheid niveaus hoger dan laagaangroei intrinsieke waarden te onderdrukken is onderzocht in hoofdstuk 2. Gebruik makend van een verlengde Kr^+ behandeling konden componenten in het ruwheidspectrum met laterale lengteschalen tot 500 nm sterk worden onderdrukt. Toegepast als een vervlakkende laag onder een multilaag structuur resulteerde dit in een verbeterde EUV reflectie. De relaxatie van de verschillende componenten in het ruwheidspectrum bleek evenredig te zijn met de ruimtelijke frequentie. Dit duidt erop dat de Si lagen vloeistofachtige kenmerken krijgen onder invloed van het ionen bombardement. Volgens de gangbare modellen zou de vervloeiing zich uitstrekken tot diep in de behandelde laag; dit is in tegenspraak met het feit dat de lagen erg dun zijn en bovendien hebben de ionen een zeer beperkte indringdiepte. Berekeningen hebben aangetoond dat het opvullen van lege ruimten onder het oppervlak, tijdens het vervloeien van de laag onder invloed van de behandeling met ionen, een plausibele verklaring van de observaties is.

In hoofdstuk 3 wordt een procedure beschreven waarin H^+ ionen in Si lagen worden geïmplanteerd, om de lagen poreuzer te maken. Volgens de bevindingen gepresenteerd in hoofdstuk 2, kan dit leiden tot een betere vervlakking van de lagen tijdens een Kr^+ ionen bombardement. Atomaire concentraties H in het Si van 30% zijn behaald, wat een 10% gereduceerde dichtheid oplevert. In lijn met de verwachtingen bleek een Kr^+ bombardement te resulteren in een nog betere vervlakking op de Si:H lagen dan op de gewone Si lagen.

In hoofdstuk 4 wordt de invloed beschreven van het soort edelgas ionen, zoals gebruikt voor het ionen bombardement, op de ruwheid van grenslagen in Mo/Si multilagen. De gassen in volgorde van toenemende atomaire massa zijn: neon (Ne), argon (Ar), krypton (Kr) en xenon (Xe). De ruwheden zijn bestudeerd aan de hand van metingen aan de verstrooiing van röntgen stralen. De zwaarste ionen (dus Xe) gaven de beste vervlakking, hoewel een polijst proces met Xe niet optimaal bleek voor de EUV reflectie. Dit wordt verklaard door gemeten kleine hoeveelheden edelgas die in de multilaag achterblijven na het polijst proces, wat in het geval van Xe een nadelige invloed heeft op de reflectie omdat het atoom relatief veel EUV licht absorbeert.

Hoofdstuk 5 beschrijft de toepassing van een EUV reflectieve multilaag op een niet-vlak tralie substraat. Zulke systemen bieden zeer interessante mogelijkheden als optisch filter voor ongewenste golflengte die geproduceerd worden door EUV licht bronnen. Berekeningen naar de werking van dit filter worden gepresenteerd, en laten zien dat ongewenste infrarode straling gescheiden kan worden van het EUV licht. Dit gebeurt zonder verliezen op te leveren in EUV reflectie ten opzichte van een vlakke multilaag spiegel. De depositie van multilagen op een niet-vlakke ondergrond is beschreven in hoofdstuk 6. Het profiel van de individuele lagen in een multilaag is bestudeerd met een transmissie electronen microscoop. Op basis van de metingen is een aangroei model ontwikkeld. Het is gebleken dat wanneer een multilaag gedeponeerd wordt op een niet-vlakke ondergrond, scherpe randen in het profiel deels worden uitvlakt door het ionen bombardement. Uit verdere metingen met een EUV microscoop blijkt dat dit alleen dichtbij een rand plaatsvindt en daarom niet problematisch hoeft te zijn.

De laatste bevindingen onderschrijven dat het mogelijk is een multilaag te deponeren op een tralie-substraat, met behoud van het voorgedefinieerde tralie profiel. Het is van belang dat het tralie-substraat voldoet aan de hoogste kwaliteitseisen wat betreft de vlakheid en de vorm van de tralie facetten, wat in de praktijk niet zomaar mogelijk is. In hoofdstuk 7 tenslotte, wordt een ontwerp en depositie schema beschreven dat het mogelijk maakt een multilaag-tralie structuur te fabriceren, beginnend met een simpel vlak substraat. Door de dimensies aan te passen, kan deze structuur gebruikt worden als optisch filter voor ongewenst licht van elke golflengte, mits langer dan 100 nm, inclusief de golflengte gebieden die problematisch zijn in EUV lithografie: het vacuüm ultraviolet (100-400 nm) en infrarood (10.600 nm). Zowel theoretisch als experimenteel (nog niet geoptimaliseerd) is het werkingsprincipe aangetoond. Een factor 30 onderdrukking van het vacuüm ultraviolet is behaald terwijl de EUV reflectie met 64% zeer hoog blijft.

Acknowledgements/Dankwoord

I would like to thank my promotor Fred Bijkerk, for offering me the opportunity to do my PhD research, and for encouraging me in my work. Also I would like to thank my group leader Eric for facilitating my work by giving me the freedom to pursue unpaved roads, arranging access to the experimental facilities, and for proof-reading of my papers. Erwin usually was the first person I consulted for general discussion or whenever specific problems occurred. Your experimental intelligence and commonsense reasoning have been of great help. Big credits go to the skillful operators Santi, Peter, and Frenk, who did most of the depositions described in this thesis. I would like to thank Fred van Goor (Twente University) for discussions and inspiring my work on multilayer-grating systems. I would like to acknowledge Robert (Twente University) and “my” master student Daniël for exploring new, promising methods of multilayer-grating fabrication, while I was occupied with finalizing this thesis.

I especially enjoyed working with- and the company of- my fellow PhD-students, without exceptions. I would like to thank my friend from university Tim who introduced me to the group, and Igor for performing the GISAX measurements. Saskia: besides your help with CuK_α-analysis, I really liked the exquisite home-baked pies you brought to the coffee breaks! Hirokazu, I am grateful that you became a friend and my paranimf.

Het belangrijkste is dat ik altijd steun en afleiding heb gehad van mijn vrienden, familie, ouders en zussen, en natuurlijk Annemiek.

Dank

Curriculum Vitae

Toine van den Boogaard was born on the 17th of January 1982 in Zeist, the Netherlands. He obtained his VWO diploma at K.S.G. de Breul in 2000, after which we he studied physics at Utrecht University from 2000 to 2007. His bachelors research project was performed in the Soft Condensed Matter group, under the supervision of prof. A. van Blaaderen and A. van der Horst, were he investigated the trapping of micrometer scale particles in colloidal dispersions by optical tweezers. His graduation research was performed in the nanolayer-Surface and Interface Physics department, led by prof. F. Bijkerk, at the Institute for Plasma Physics Rijnhuizen, on the topic of smoothening Si layers for EUV mirror substrates. After his graduation, he accepted a position as PhD-student in the same department, on the topic of ion-enhanced thin-film growth, which has resulted in this thesis.

List of publications

Chapter 2

A.J.R. van den Boogaard, E. Louis, E. Zoethout, S. Müllender, and F. Bijkerk, "Surface morphology of Kr^+-sputtered amorphous Si layers," Journal of Vacuum Science and Technology A **28**, (2010).

Chapter 3

A.J.R. van den Boogaard, E. Zoethout, E.Louis, and F. Bijkerk, "Influence of hydrogenic retention in a-Si on ion-sputtered surface morphology," *submitted*.

Chapter 4

A.J.R. van den Boogaard, E. Zoethout, I. Makhotkin, E. Louis, and F. Bijkerk, "Influence of noble gas ion polishing species on Mo/Si multilayers," *submitted*.

Chapter 5

A.J.R. van den Boogaard, E. Louis, F.A. van Goor, and F. Bijkerk, "Optical element for full spectral purity from IR-generated EUV light sources," proceedings of SPIE **7271-159**, San Jose, (2009).

Chapter 6

A.J.R. van den Boogaard, E. Louis, E. Zoethout, K.A. Goldberg, and F. Bijkerk, "Characterization of Mo/Si multilayer growth on stepped topographies," Journal of Vacuum Science and Technology B **29, (**2011).

Chapter 7

A.J.R. van den Boogaard, F.A. van Goor, E. Louis, and F. Bijkerk, "Wavelength separation from extreme ultraviolet mirrors using phaseshift reflection," Optics Letters, *accepted for publication*.